CVD synthesis and characterization of nitrogen-doped SWNTs

(窒素ドープ単層 CNT の CVD 合成と評価)

ﾄｳﾗｷｯﾄｾｰﾘｰ　ﾃｨｰﾗﾎﾟﾝ

CVD synthesis and characterization of nitrogen-doped SWNTs

(窒素ドープ単層 CNT の CVD 合成と評価)

by Theerapol THURAKITSEREE

A thesis presented in partial fulfillment of
the requirements for the degree of
DOCTOR OF PHILOSOPHY

東京大学大学工学系研究科機械工学専攻

Department of Mechanical Engineering
The University of Tokyo

August 2013

This thesis entitled "CVD synthesis and characterization of nitrogen-doped SWNTs", submitted by Theerapol THURAKITSEREE, is approved by the undersigned members of this committee.

Prof. Shigeo Maruyama, Thesis advisor and Chairman
Department of Mechanical Engineering,
The University of Tokyo

Prof. Yuichi Ikuhara,
Institute of Engineering Innovation
The University of Tokyo

Prof. Tatsuya Okubo,
Department of Chemical System Engineering
The University of Tokyo

Assoc. Prof. Junichiro Shiomi,
Department of Mechanical Engineering
The University of Tokyo

Dr. Shohei Chiashi,
Department of Mechanical Engineering
The University of Tokyo

Declaration

I, hereby, swear on my conscience that I have perused the "Code of Conduct in Scientific Research at the University of Tokyo" and the "Ethics Guidelines for Scientific Research at the Graduate School of Engineering, the University of Tokyo", correctly understood the content, and complied with these and other rules when preparing this dissertation to the University of Tokyo.

Tokyo, August 2013

If the idea of electricity was left in Edison imagination,
we would never had electricity.

If the idea of literature was left on a nib of Shakespeare,
we would never had nice literature to read.

If the idea of liberty stuck on the lip of Gandhi,
the world would never been peace as it is now.

Do not let your idea stop just an idea,
all ideas are possible if you start.

-Unnamed PhD student

Contents

Preface v

1 Introduction 1

1.1 Electronic density of states . . . 1

1.1.1 Particles in different dimensions . . . 2

1.1.1.1 Particles in 1D line . . . 2

1.1.1.2 Particles in a 2D plane . . . 3

1.1.1.3 Particles in a 3D box . . . 4

1.1.2 Single-valley in different dimensions . . . 6

1.1.2.1 Density of states in bulk materials (3D) . . . 6

1.1.2.2 Density of states in 2D and 1D . . . 8

1.1.2.3 Density of states in 0D . . . 10

1.2 Carbon nanotube . . . 10

1.2.1 Archetypes of carbon nanotube . . . 10

1.2.2 Geometry in SWNTs . . . 12

1.2.2.1 Real-space representation . . . 12

1.2.2.2 Reciprocal-space representation . . . 14

1.2.3 Electronic structure of SWNT . . . 15

1.3 Electronic properties and spectroscopy . . . 21

1.3.1 Raman spectroscopy . . . 21

1.3.1.1 Scattering process . . . 21

1.3.1.2 Raman spectroscopy of SWNTs . . . 23

1.3.2 Optical spectroscopy . . . 26

1.3.2.1 Absorption in general . . . 26
1.3.2.2 Optical transition of SWNT . . . 27
1.3.2.3 Photoluminescence Excitation spectroscopy 30
1.3.3 Photoemission spectroscopy . . . 32
1.3.4 Near-edge x-ray absorption spectroscopy . . . 34
1.3.5 Electron microscope . . . 36
1.4 Synthesis and bulk SWNTs . . . 39
1.4.1 Synthesis of SWNTs . . . 39
1.4.2 Alcohol-catalytic CVD . . . 40
1.4.2.1 Catalyst loading . . . 41
1.4.2.2 SWNT dispersion . . . 42

2 Nitrogen-doped SWNTs 45
2.1 Electronic states of N-doping SWNTs . . . 46
2.2 Doping-dependent diameter change . . . 48

3 Synthesis of small-diameter VA-SWNTs 51
3.1 Introduction . . . 51
3.2 Diameter modulation by acetonitrile . . . 52
3.2.1 Synthesis of small-diameter VA-SWNTs . . . 52
3.2.2 Characterization of small-diameter VA-SWNTs . . . 54
3.3 Diameter tailoring . . . 59
3.3.1 Influence on flat substrate . . . 59
3.3.2 Influence on zeolite . . . 64
3.3.3 Evaluation of SWNT mean diameter . . . 68
3.4 Nitrogen-doped SWNTs . . . 71

4 One-Dimensional Nitrogen molecule 75
4.1 Introduction . . . 75
4.2 Encapsulated nitrogen gas . . . 76
4.3 Isotope ^{15}N-labeled encapsulated N_2 . . . 82
4.4 Aligned N_2 molecule inside VA-SWNTs . . . 86

5 Multi-layered growth and growth mechanism **91**
5.1 Introduction 91
5.2 Synthesis of multi-layered SWNT arrays 92
5.3 Catalyst-Independent Diameter Modulation 95
5.4 Diameter reversibility 98
5.5 Interface examination 101
5.6 Role of nitrogen and growth mechanism 106

6 Conclusion and prospect **109**

Appendix **113**

Bibliography **117**

Acknowledgement **137**

Curriculum vitae **141**

List of Figures **145**

List of Publications **149**

Preface

Single-walled carbon nanotube (SWNT) has been recognized as special one-dimensional material fruitful with many promising properties. The experimental and theoritical studies have been revealing its great physical, optical, and electrical properties. By utilizing catalyst support, mass production processes on SWNT synthesis have been commercialized as CoMoCAT [1], HiPco [2], and ACCVD [3] methods, which provide good quality SWNTs for the next step of applications. It seems that carbon nanotube (CNT) research has been diverted after discovery of graphene for the last decade [4, 5]. A solely chirality dependence [6] have still been arousing many researchers to continue studying what nanotube can indeed contribute to the near future applications after a few decades of discovering, even though graphene the new generation two-dimensional carbon material theoritically provides a great mobility and transparency [7, 8].

In 2011, feasible potential applications from tunable nanotube film thicknes and transparency with high mobility and sheet resistance have been reported on multi-walled CNTs and SWNTs [9]. Interesting, their properties seem to have very promising properties without post-treatment as separation process, comparable with the well-know commercial indium tin oxide (ITO) used as flexible electric devices. Additionally, many reports on energy storage and some other application, for instance CNT sponge [10–12], nanotube yarn [13–15], chemical doping on nanotubes [15–18], have been again shown for the use of nanotubes. With these establishments, SWNTs have been brought back to promising research interest.

Electronic, electrical and optical properties of SWNT are essentially dependent of chirality [6]. Performance or efficiency of devices consequently require in principal narrow number of present chirality in the sample. Direct chirality control is, however, considerably delicate in experiment. Although the great number of researches on chirality control has struggled to conquer difficulties to reduce number possible chiralities or modify electronic properties [15–20]. One feasible approach is in general to confine a mean diameter of SWNTs for the direct use. It has been often questioned that *Can we actually control chirality or diameter*? However, different interpretations of research arise from the various approaches. The more diameter we reduce the less chirality we have. Another issue is *can we also modify electronic properties of SWNTs*? since introducing heteroatoms into the carbon lattice or chemical doping have opened up another availability of electrical modification by changing electronic state of nanotubes. In order to complete and overcome this problematical issues, structure control and growth mechanism are necessary for well understanding of how structure and properties can be tuned, especially synthesis on flat substrate.

This PhD thesis *CVD synthesis and characterization of nitrogen-doped single-walled carbon nanotubes* begins with brief introduction to fundamental on electronic density of state in different dimensional materials and single-walled carbon nanotube (SWNT) beginning in Chapter 1. Following this fundamentals, the physical, optical, and electronic properties of SWNTs will be discussed, prior to reviewing a brief history of nanotube synthesis and N-doped carbon nanotubes in Chapter 2. The fundamental introduction on electronic density of state, nanotube properties will be implemented to explain and discuss the results presented later.

In Chapter 3, the results of diameter-controlled CVD synthesis will be discussed, which discusses the synthesis of small-diameter VA-SWNTs from $\sim 2.1\,\mathrm{nm}$ to $\sim 0.8\,\mathrm{nm}$ from changing just carbon precursors. In this section, change in spectroscopic aspects are discussed. Diameter reduction is comprehensively characterized. I also demonstrated a great influence of

nitrogen incorporation during synthesis on the reduction of quantitative SWNT mean diameter. Along with correlation between nitrogen content and nanotube mean diameter, the incorporated nitrogen configurations are also discussed.

An unexpected encapsulated nitrogen molecule (N_2) is investigated and demonstrated in Chapter 4. A viability of N_2 from feedstock is demonstrated using isotope $CH_3{-}C^{15}N$. The characterization of encapsulated N_2 by near-edge x-ray absorption fine structure (NEXAFS), as well as, deflating of N_2 from interior of SWNTs give an insight into a more detail of growth mechanism in nitrogen-doped SWNTs. Availability of N_2 inside such small-diameter SWNT indicates a suitable interior one-dimension container. I also revealed the polarization-dependent of N_2 gas inside confined one-dimensional space, showing co-axially alignment of gas molecules in the interior of the narrow SWNTs (less than 1 nm), presented by degree of alignment along with the combined molecular dynamic simulation.

In Chapter 5, I presented facile modulation of SWNT diameters during CVD synthesis by changing the carbon precursor between pure ethanol and an acetonitrile-ethanol mixture. Using this method I am able to reversibly change the SWNT diameter between 2 nm (for pure ethanol) and ~ 1 nm (for the acetonitrile mixture). This feedstock-dependence indicates the process is independent of catalyst particle size. The majority of discontinuous heterojunctions with some presented continuous interface is demonstrated by either TEM observation, or number of N_2 molecules passing through different diameter SWNTs interface. I also proposed a possible growth mechanism and stress out the role of nitrogen on the reduction of SWNT diameter.

Chapter 1

Introduction

1.1 Electronic density of states

In general, many phenomena, bounding of the balls, interaction force of objects, or acceleration of cars, for example, can be well explained by classical mechanic which allows us to understand physic phenomena in large scale. Considering interaction between atom and electron, one can think of coulomb interaction which can be explained by simple classical mechanic. The more complicated phenomena is, however, taken into account due to atomic scale consideration in which electron can be excited and leave an atom prior to turning back to ground state by decaying energy showing in spectrum. Another example is photon behavior which can be considered as either particle or wave. These kinds of phenomena in nanoscale or atomic scale are invalid, consequently, quantum mechanic would be well expected. Even though quantum mechanic is not touchable nor visible, it can be tested by experiment for instance photoemission and scattering of electrons. It can be furthermore alluded to well describe quantum well, wire, or dot. To valid the energy or wavefunctions of particles, time-independent Schrödinger equation can be used to solve this problem as expressed below,

$$\hat{H}\psi = E\psi, \qquad \hat{H} = -\frac{\hbar^2}{2m}\Delta + V(x)$$

where ψ is the wavefunction in stationary state with the energy, E, and $\hat{H}$ is Hamiltonian operator, which depends on situation described as potential function $V(x)$, particle's mass m, and Laplace transform Δ with $\hbar$ ($\frac{h}{2\pi}$).

For complicated problem, instead of employing multiple times of Schrödinger equation, it can be solved by density of states–a function that shows multiple intervals of energy with available states in that energy range as expressed in term of carrier density (N) in the energy range of dE with desired density of states (DOS) function (ρ_{energy}),

$$N_{\text{total}} = \int_{E_1}^{E_2} \rho_{\text{energy}}(E)\mathrm{d}E, \tag{1.1}$$

where N_{interval} is carrier density within the energy range, and N_{total} is total carrier density in the system within energy range of E_1 to E_2.

Density of state (DOS) in semiconducting materials is dependent of concentration of carriers, such as impurities and free carriers, which modify the bandgap energy of materials. Localized impurity states, delocalized conduction and valence band states have to be taken into account, especially when an impurity have more than one degeneracy. The free carrier motion is generally restricted to spatial dimension (*i.e.* two, one, and zero-dimension), resulting in different structure of density of states. Such a density of states will be described in this section. As a note, most of this material can be found in comprehensive texts on solid state physics such as [21, 22].

1.1.1 Particles in different dimensions

1.1.1.1 Particles in 1D line

To make clear understanding on density of states in any dimensions, let me begins with an idea of particles moving in one-dimension (1D) line. In 1D system, it is confine in lateral expansion (*i.e.* nanoscale), but infinite in one direction paralleled to the direction of moving particles ($k_{\|}$). One can think as infinite potential well, which is limited to certain regime of $x = 0$ to $x = L$ with potential $V(x) = 0$ in $0 \leq x \leq L$. Meaning that particles

can move freely only in $0 \leq x \leq L$ without leaving which give boundary condition $\psi(0) = \psi(L) = 0$. The wavefunction and energy that quantized of confined particles are

$$\psi_n(x) = \sqrt{\frac{2}{L}} \sin\left(\frac{n\pi}{L}x\right)$$

$$E_n = \frac{n^2\pi^2\hbar^2}{2m^*L^2} = \frac{\hbar^2k^2}{2m^*} \tag{1.2}$$

where $n = 1, 2, 3, ...$, $k = \frac{n\pi}{L}$, L is length of the box, and m^* is effective mass of particle (*i.e.* electron). The higher n represent electron in excited states. From Equation 1.2, we can obtain, $n = \frac{L}{\pi\hbar}\sqrt{2m^*}\sqrt{E_n}$, and differentiation of n by E will give sparse energy density as,

$$g(E) \sim \frac{\mathrm{d}n}{\mathrm{d}E} = \frac{L}{\pi\hbar}\sqrt{\frac{m^*}{2}}\frac{1}{\sqrt{E_n}}. \tag{1.3}$$

An approximated desired density of states function can be now obtained with units of number per unit energy per unit length by dividing previous expression by the length of the box (L). Hence, desired density of states $\left(\frac{g(E)}{L}\right)$ results in

$$\boxed{\rho^{\mathrm{1D}}_{\mathrm{energy}} = \sqrt{\frac{2m^*}{h^2}}\frac{1}{\sqrt{E_n}}.}$$

1.1.1.2 Particles in a 2D plane

In two-dimension (2D) system, the idea of how particles move is similar to that in 1D, but particles are allowed to move into two directions instead of one which means moving direction of particle is now confined on the circle plan in dimension L (*i.e.* x-y plane). In this case, there are two-components in k-space. The potential is zero inside the 2D plane and infinite outside of the box, the wavefunction calculated from Schrödinger equation

will be expressed according to Equation 1.4 with the energy as shown in Equation 1.2,

$$\psi_{n_x,n_y} = \frac{2}{L}\sin\left(\frac{n_x\pi}{L}x\right)\sin\left(\frac{n_y\pi}{L}y\right). \tag{1.4}$$

In two-dimensional case, k and n are considered in two directions as $k^2 = k_x^2 + k_x^2$ ($k_x = \frac{n_x\pi}{L}$, and $k_y = \frac{n_y\pi}{L}$), and $n^2 = n_x^2 + n_y^2$ ($n_x = 1, 2, 3, ...$, and $n_y = 1, 2, 3, ...$), respectively. The constant energy will be proportional to indices n_x and n_y ($E \propto n_x^2 + n_y^2$). Hence, a small change in n (Δn) will give a slight change in larger energy ($E + \Delta E$). Now, the area of expanded n is $2\pi n\Delta n$. Let approximate $\Delta n \to \mathrm{d}n$ and consider one quadrant of circle, which gives area of interest $2\pi n\mathrm{d}n$. Consequently, energy density of interested area is

$$g^{2\mathrm{D}}(E)\mathrm{d}E \sim \frac{1}{4}(2\pi n\mathrm{d}n), \qquad g^{2\mathrm{D}}(E) \sim \frac{\pi}{2}\left(n\frac{\mathrm{d}n}{\mathrm{d}E}\right) \tag{1.5}$$

From the Equation 1.3 and 1.2, we can find that

$$g^{2\mathrm{D}}(E) \sim \frac{\pi}{2}n\frac{L}{\pi\hbar}\sqrt{\frac{m^*}{2}} = \frac{m^*L^2}{2\pi\hbar^2} = \frac{2\pi m^*L^2}{h^2}$$

We can, therefore, identify the desired density of states function of particles in 2D system as $\left(\frac{g^{2\mathrm{D}}(E)}{L^2}\right)$, results in constant value of 2D density of states,

$$\boxed{\rho^{2\mathrm{D}}_{\mathrm{energy}} \sim \frac{2\pi m^*}{h^2}.} \tag{1.6}$$

1.1.1.3 Particles in a 3D box

Let me now consider larger dimension as three-dimension system, each impurity has single degenerate state, resulting in the same concentration of impurities which equals to the density of impurity state. Because it is infinite dimension, impurity can move everywhere and boundary condition of wavefunction ψ does not exist. Meaning that momenta of impurities or particles are free. Spherical and parabolic dispersion relation are considered

for the simplest band structures. We can find the wavefunction in 3D system as expressed in Equation 1.4. Hence, we can plug in three opponents in k-space (k_x,k_y,k_z) as

$$\psi_{n_x,n_y,n_z} = \left(\frac{2}{L}\right)^{3/2} \sin\left(\frac{n_x\pi}{L}x\right) \sin\left(\frac{n_y\pi}{L}y\right) \sin\left(\frac{n_z\pi}{L}z\right)$$

where k and$n$ are again considered in three dimensions as $k^2 = k_x^2 + k_x^2 + k_z^2$ ($k_x = \frac{n_x\pi}{L}$, $k_y = \frac{n_y\pi}{L}$, and $k_z = \frac{n_z\pi}{L}$), and $n^2 = n_x^2 + n_y^2 + n_z^2$ ($n_x = 1, 2, 3, ...$, $n_y = 1, 2, 3, ...$, and $n_z = 1, 2, 3, ...$), respectively. The quantized energy is also given with the same relation as in Equation 1.2

The energy density is now associated with the expansion of n in three dimensions (dn), and the expansion in one quadrant of spherical is considered ($\frac{1}{8}4\pi n^2 \mathrm{d}n$). As described in Equation 1.5, the energy density is

$$g^{3D}(E)\mathrm{d}E \sim \frac{1}{8}(4\pi n^2 \mathrm{d}n), \qquad g^{3D}(E) \sim \frac{1}{2}\pi n^2 \frac{\mathrm{d}n}{\mathrm{d}E}$$

From $\frac{\mathrm{d}n}{\mathrm{d}E}$ in Equation 1.3, such that

$$g^{3D}(E) \sim \frac{1}{2}\pi n^2 \frac{L}{\pi\hbar}\sqrt{\frac{m^*}{2}}\frac{1}{\sqrt{E_n}}$$

$$g^{3D}(E) \sim \frac{\pi}{4}\left(\frac{8m^*L^2}{h^2}\right)^{3/2}\sqrt{E_n}$$

Hence, the desired density of states function of particles in 3D system can be identified as $\left(\frac{g^{3D}(E)}{L^3}\right)$, resulting with no longer constant which possesses the characteristic of $\sqrt{E}$ dependence as expressed below.

$$\boxed{\rho^{3D}_{\text{energy}} \sim \frac{\pi}{4}\left(\frac{8m^*}{h^2}\right)^{3/2}\sqrt{E_n}.}$$

1.1.2 Single-valley in different dimensions

1.1.2.1 Density of states in bulk materials (3D)

The density of states in bulk materials is basically from the idea of 3D box. In this case, let me consider sphere in k-space as depicted in Figure 1.1. The electronic density of states is defined as the number of electron states per unit volume per unit energy. The finiteness of density of states is defined by the *Pauli principle* in which two opposite spinning electrons can only occupy one volume element in the phase space that is defined as three-dimension of real space and three-dimension of momenta space. In volume element, phase space must be distinguishable for which positions (x, y, z) and momenta (p_x,p_y,p_z) of particles follow *Heisenberg uncertainty relation* given by

$$\Delta x \Delta y \Delta z \Delta p_x \Delta p_y \Delta p_z \geq (2\pi\hbar)^3$$

Since momentum relation is $p = \hbar k$, such that

$$\Delta x \Delta y \Delta z \Delta k_x \Delta k_y \Delta k_z \geq (2\pi)^3$$

From Equation 1.1, where $\rho_{\mathrm{DOS}}(E)$ is the density of state per unit energy per unit volume, we can obtain the density of state per unit energy dE by determining unit-volume in k-space in the energy interval of $E + \mathrm{d}E$. By differentiation, we obtain the ratio of volume space per unit energy as $\frac{\mathrm{d}V}{\mathrm{d}E}$ or $\mathrm{d}E = \frac{\partial E}{\partial k}\mathrm{d}k$. Thus, the volume of k-space enclosed within two constant energy surfaces in one dimension can be calculated as

$$V_{k-\mathrm{space}}(E) = \mathrm{d}E \int_{\mathrm{surface}} \frac{\partial k}{\partial E(k)} ds$$

where ds is area element of constant energy surface. However, we can obtain $\nabla_k = (\frac{\partial}{\partial k_x}, \frac{\partial}{\partial k_y}, \frac{\partial}{\partial k_z})$ for volume space in three dimension given by

$$V_{k-\mathrm{space}}(E) = \mathrm{d}E \int_{\mathrm{surface}} \frac{ds}{\nabla_k E(k)}$$

In phase space, a volume of $4\pi^3$ is required by electrons or particles, so the number of states per unit volume is given by

$$N(E) = \frac{1}{4\pi^3}\mathrm{d}E \int_{\mathrm{surface}} \frac{ds}{\nabla_k E(k)}$$

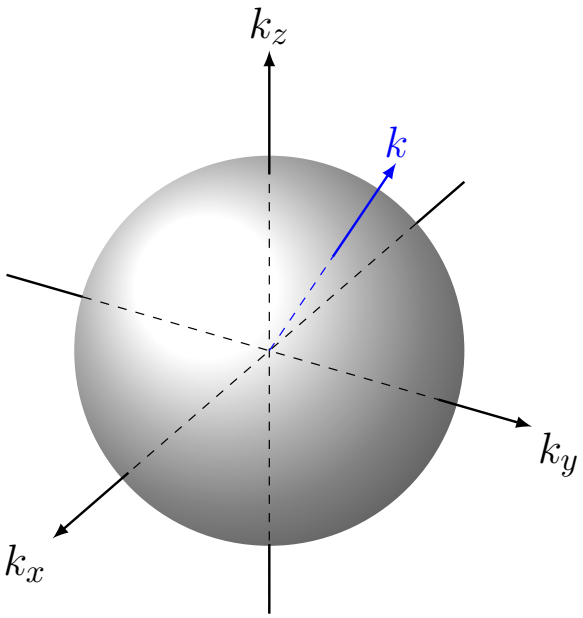

Figure 1.1: Visualization of Ewald's sphere in the three dimensional k-space. States with energies between E and $E + \mathrm{d}E$ from Equation 1.8 lie in the hollow sphere between k and $k + \mathrm{d}k$.

Hence, the density of states per unit energy and unit volume is

$$\rho_{\mathrm{DOS}}(E) = \frac{1}{4\pi^3} \int_{\mathrm{surface}} \frac{ds}{\nabla_k E(k)} \tag{1.7}$$

We now identify the density of states by inserting symmetric parabolic dispersion relation of $E = \frac{\hbar^2 k^2}{2m^* + E_n}$ in Equation 1.7, where k is wave vector, and E_n is potential energy in band edge n, as following expression,

$$\boxed{\rho^{\mathrm{3D}}_{\mathrm{DOS}}(E) = \frac{1}{2\pi^2} \left(\frac{2m^*}{\hbar^2}\right)^{3/2} \sqrt{E - E_n}.} \tag{1.8}$$

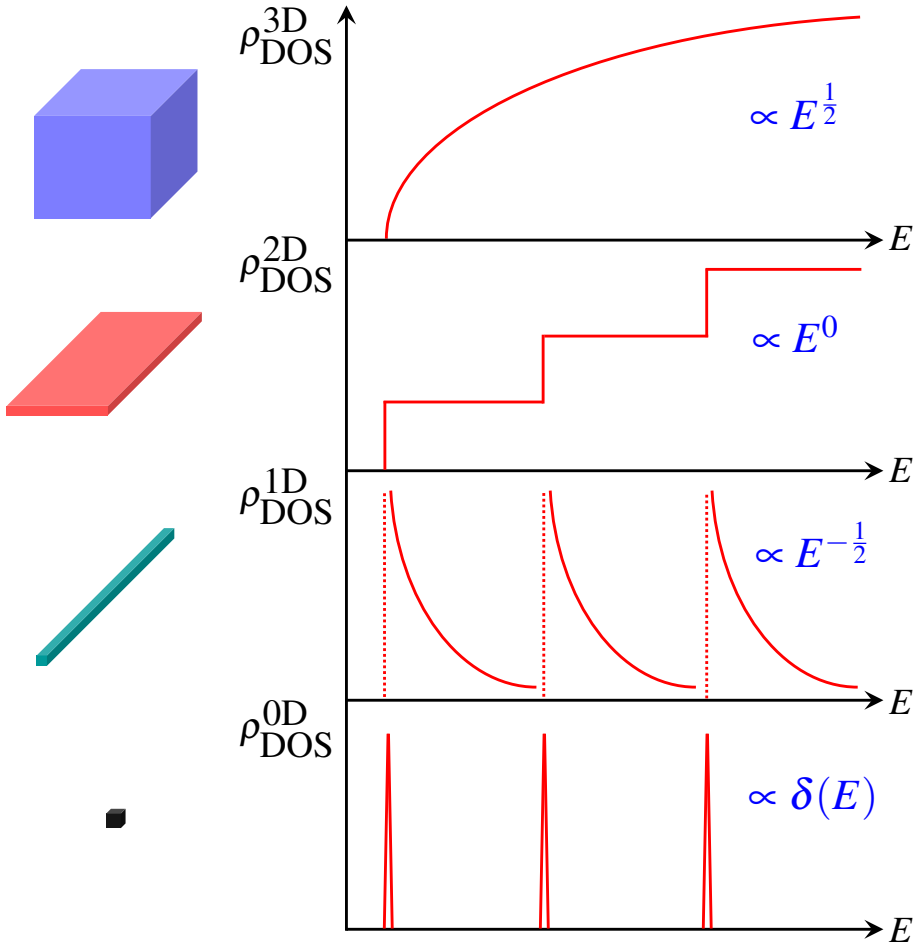

Figure 1.2: Energy-dependent density of states in different dimensions: free electrons in three dimensions (blue, Equation 1.8), confinement in two dimension of a plane (red, Equation 1.9), confinement in one dimension of quantum wire (green, Equation 1.10) and confinement in zero dimension of quantum dot (black, Equation 1.11).

1.1.2.2 Density of states in 2D and 1D

As stated in Section 1.1.1, confinement of charge carrier have to be considered. Thus, dispersion relation along the confinement direction is changed, resulting in change in the density of states. In two dimension, the dispersion is flat (*i.e.* constant k_z), the reduced phase space is now only xy-plane, which is similar to particles in 2D plane. The constant surface energy dispersion

is given by Equation 1.9, resulting in the constant density of states (see Equation 1.6). If the 2D semiconductor has more than one quantum state, the total density of states can be written by sum of difference of quantum states as

$$\boxed{\rho^{\mathrm{2D}}_{\mathrm{energy}} \sim \frac{2\pi m^*}{h^2} \sum_n \sigma(E - E_n),} \tag{1.9}$$

where $\sigma(E - E_n)$ is the function step, and E_n is the energy of quantized states.

On the other hand, confinement of 1D system is restricted to only one direction of motion. The dispersion relation is given by Equation 1.2. The surface integral is also reduced to single point in k-space (k_x). Thus, the volume is k-space is given by

$$V^{\mathrm{1D}}_{k-\mathrm{space}}(E) = \int_{\mathrm{surface}} \frac{\delta(k_x - k_{x_0})}{\nabla_k E(k_x)} ds = \sqrt{\frac{m^*}{2\hbar^2(E - E_0)}} (E \geq E_0).$$

Hence, the volume in phase space of two opposite spinning electrons is given by 2π, and the density of states in 1D is given by

$$\rho^{\mathrm{1D}}_{\mathrm{DOS}}(E) = \frac{1}{\pi\hbar} \sqrt{\frac{m^*}{2(E - E_0)}} (E \geq E_0).$$

In the case of more than one quantized states, the total density of states is given by

$$\boxed{\rho^{\mathrm{1D}}_{\mathrm{DOS}}(E) = \frac{1}{\pi\hbar} \sum_n \sqrt{\frac{m^*}{2(E - E_0)}} \sigma(E - E_n).} \tag{1.10}$$

where E_n is the energy of the quantized states of nanowire, nanotube, *etc.*

1.1.2.3 Density of states in 0D

Finally, let me consider zero-dimension (0D) as quantum box in which confinement is fully restricted in all three dimensions (*no free motion*). Thus, there is no k-space available fro electrons to fill up. Consequently, only two electrons occupy quantum state in 0D. The density of states of 0D dimension is, therefore, expressed by Direc function, δ, given by

$$\rho_{\mathrm{DOS}}^{\mathrm{0D}}(E) = 2\delta(E - E_0)$$

And for more than one quantized state, the density of states in 0D can be described by sum of single state of the density of states, given by

$$\boxed{\rho_{\mathrm{DOS}}^{\mathrm{0D}}(E) = \sum_n 2\delta(E - E_0).} \tag{1.11}$$

1.2 Carbon nanotube

1.2.1 Archetypes of carbon nanotube

Carbon is the element surrounding us not only inside, but also outside our body. it exists everywhere for instance air, wood and metal, the most well-known is charcoal (*i.e.* graphite). Carbon-based materials have been realized as major materials due to their availability. Carbons have been found in many forms depending on atomic arrangement. Diamond is another carbon species, which is well-known in term of luxury valuable. Because of its sp^3 hybridization in which atomic arrangement forms a tetrahedral structure formed by bonding contribution of each carbon atom with neighboring atom. This type of configuration provides an unique optical property with transparency to a bulk carbon material, like diamond. Carbons, on the other hands, can also form an sp^2 hybridization in form of layer or planar structure which gives a different properties. The planar structure of sp^2 is generally found in form of stacked layers as known as bulk or three-dimensional (3D)

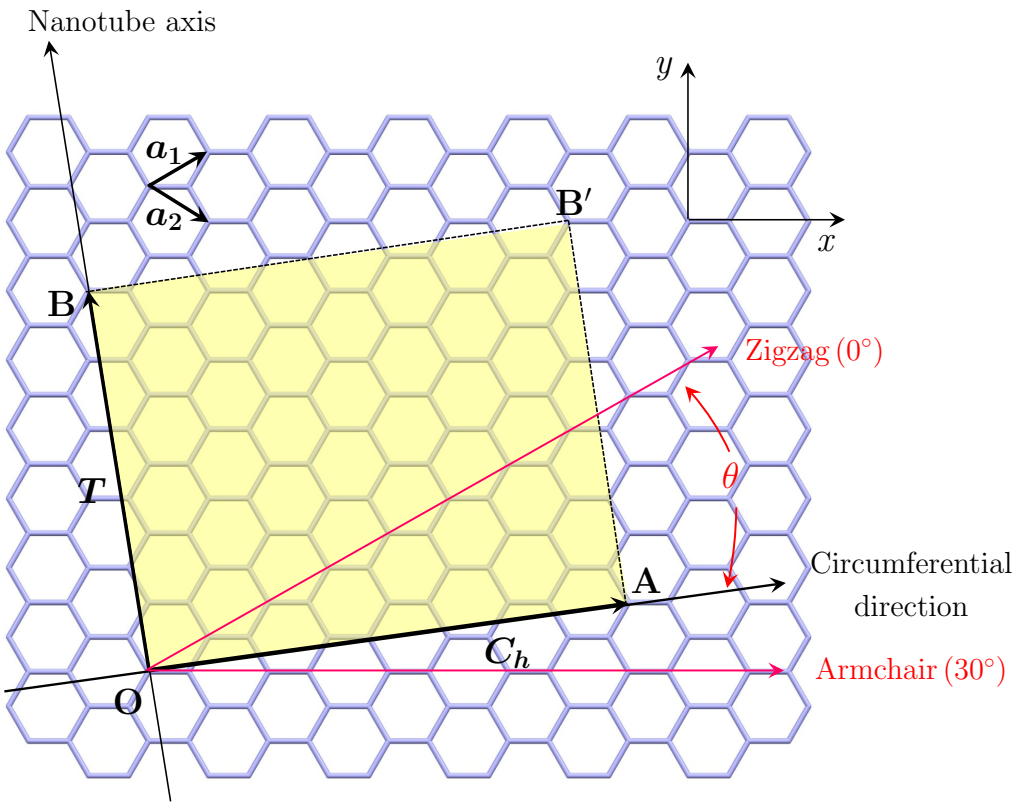

Figure 1.3: Geometry of graphene sheet shows the chiral vector $\boldsymbol{C}_h$ for an SWNT rolling into different orientations with chiral angle θ.

graphite. The van der Waals interaction between layers in graphite is very weak, consequently, they can be separated into single-layered sheet, call *graphene*. Another sp^2 hybridization carbon structure was found to form of *carbon nanotube* which has been proven to be an impressive 1D material with electrical, optical and mechanical properties, especially single-walled carbon nanotube (SWNT). Because of length to diameter ratio, SWNT has been introduced as one-dimension (1D) carbon that give it some very interesting properties and make it become promising material for carbon-based devices. To understand the electronic property of SWNTs affected by their low dimensionality, it is useful to present a formal description of SWNT geometry. As a note, most of this material in this chapter can be found in comprehensive texts such as [6, 23, 24].

1.2.2 Geometry in SWNTs

1.2.2.1 Real-space representation

A SWNT is known as special tube rolled up from graphene sheet, which consists of all carbon atoms formed honeycomb lattice on the wall. It can also be conceived from rolled-up stripe of graphene in which the orientation of the six-membered carbon ring in the honeycomb lattice relative to axis of the nanotube. Interesting, nanotube structure is different upon rolling orientation of graphene sheet, called *chirality* represented as (n,m) that exhibit spiral conformation. To make easy to understand SWNT geometry, one can imagine the envisage lattice of graphene. The structure of graphene is the hexagonal like structure (honeycomb) as shown in Figure 1.3 that has unit cell of hexagonal lattice containing equivalent atomic distance of a_0 (1.42 Å). Based on cartesian coordinates, unit vectors of the cell $\boldsymbol{a}_1$ and $\boldsymbol{a}_2$ are represented by

$$\boldsymbol{a}_1 = \left(\frac{\sqrt{3}a_0}{2}, \frac{a_0}{2}\right), \quad \text{and} \quad \boldsymbol{a}_2 = \left(\frac{\sqrt{3}a_0}{2}, -\frac{a_0}{2}\right) \tag{1.12}$$

where lattice constant is defined as the magnitude of the vector $\boldsymbol{a}_1$ or $\boldsymbol{a}_2$ that is $a \equiv |\boldsymbol{a}_1| = |\boldsymbol{a}_2| = 1.42\text{Å} \times \sqrt{3} = 2.46\text{Å}$. Since the structure of SWNT is envisaged from rolled graphene sheet, the unit cell of nanotube is enlarged when compared to that of the graphene due to the lower symmetry of nanotube. The lattice vectors of graphene which goes around circumferential direction, identifies nanotube structure, so called *chiral vector* ($\boldsymbol{C}_h$). The translational vector ($\boldsymbol{T}$) in nanotube axis which is perpendicular to vector $\boldsymbol{C}_h$, represents one-dimension periodicity of SWNT. The the unit cell of a certain type of SWNT is indicated as a shadowed area in Figure.

The chiral vector $\boldsymbol{C}_h$ is expressed in terms of real-space unit vectors $\boldsymbol{a}_1$ or $\boldsymbol{a}_2$ and two integers n and m ($0 \leq m \leq n$) as $\boldsymbol{C}_h = na_1 + ma_2 \equiv (n, m)$. Since the length of $\boldsymbol{C}_h$ indicates the circumferential length of the SWNT, the diameter of the nanotube (d_t) is expressed as

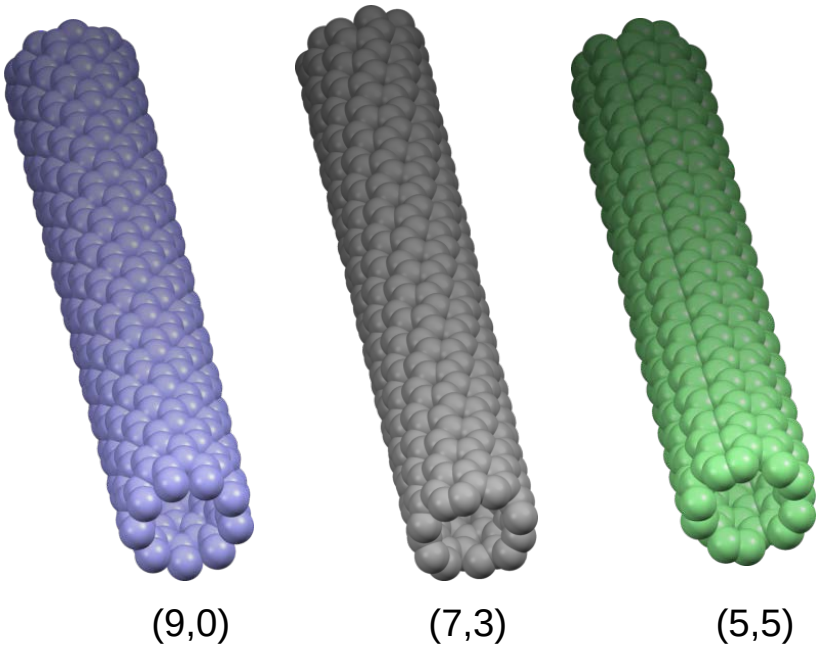

Figure 1.4: Examples of three different geometries of SWNTs: armchair (green), chiral (gray), and zigzag (blue).

$$d_t = \frac{|\boldsymbol{C}_h|}{\pi} = \frac{\sqrt{\boldsymbol{C}_h \cdot \boldsymbol{C}_h}}{\pi} = \frac{a\sqrt{n^2 + m^2 + nm}}{\pi}$$

Due to different rolling orientation of graphene, the angle is formed between $\boldsymbol{C}_h$ and $\boldsymbol{a}_1$ with *chiral angle* θ ($0 \leq \theta \leq 30°$) that produce three different geometries of SWNTs (Figure 1.4), which is expressed as

$$\cos\theta = \frac{\boldsymbol{C}_h \cdot \boldsymbol{a}_1}{|\boldsymbol{C}_h| \cdot |\boldsymbol{a}_1|} = \frac{2n + m}{2\sqrt{n^2 + m^2 + nm}}$$

The translational vector $\boldsymbol{T}$ can be obtained by solving the relationship $\boldsymbol{C}_h \cdot \boldsymbol{T} = 0$, and scaling with the greatest common divisor (d_R) of $(2m + n)$ and $(2n + m)$ in which $d_R = d$ if $n - m$ is not a multiple of $2d$, and $d_R = 3d$ if $n - m$ is a multiple of $3d$, resulting in

$$\boldsymbol{T} = t_1\boldsymbol{a}_2 + t_2\boldsymbol{a}_2 \equiv (t_1, t_2), \quad t_1 = \frac{2m + n}{d_R}, \quad t_2 = -\frac{2n + m}{d_R}$$

The magnitude of vector $\boldsymbol{T}$ is given by $T \equiv |\boldsymbol{T}| = \frac{\sqrt{3}\boldsymbol{C}_h}{d_R}$. The number of hexagons N in the unit cell of a SWNT follows directly from the area of the diatomic in unit cell rectangular of graphene according to relation,

$$N = \frac{|\boldsymbol{C}_h| \cdot |\boldsymbol{T}|}{|\boldsymbol{a}_1| \cdot |\boldsymbol{a}_2| \cdot \sin 60^\circ} = \frac{2(n^2 + m^2 + nm)}{d_R}$$

1.2.2.2 Reciprocal-space representation

While the translational vector $\boldsymbol{T}$ and the chiral vector $\boldsymbol{C}_h$ determine the unit cell of SWNT in the real space, the reciprocal-space vectors can also easily describe solid geometry as illustrated in Figure 1.5. The reciprocal lattice can be given as

$$\boldsymbol{a}_i \cdot \boldsymbol{b}_i = 2\pi\delta_{ij},$$

where $\boldsymbol{a}_i$ is the real-space vectors given in Equation 1.12, and $\boldsymbol{b}_i$ are the reciprocal vectors given by

$$\boldsymbol{b}_1 = \left(\frac{2\pi}{\sqrt{3}a}, \frac{2\pi}{a}\right), \qquad \boldsymbol{b}_2 = \left(\frac{2\pi}{\sqrt{3}a}, \frac{2\pi}{a}\right)$$

Let vectors $\boldsymbol{K}_C$ and $\boldsymbol{K}_T$ be defined as the reciprocal lattice vectors that goes around the circumference direction and along nanotube axis, respectively (*i.e.* $\boldsymbol{K}_C \perp \boldsymbol{T}$, and $\boldsymbol{K}_T \perp \boldsymbol{C}_h$). The reciprocal lattice vectors $\boldsymbol{K}_C$ and $\boldsymbol{K}_T$, therefore, satisfy the relations

$$\boldsymbol{C}_h \cdot \boldsymbol{K}_C = 2\pi, \;\; \boldsymbol{T} \cdot \boldsymbol{K}_C = 0, \quad \text{and} \quad \boldsymbol{C}_h \cdot \boldsymbol{K}_T = 0, \;\; \boldsymbol{T} \cdot \boldsymbol{K}_T = 2\pi. \quad (1.13)$$

By solving the Equation 1.13, the reciprocal vectors $\boldsymbol{K}_C$ and $\boldsymbol{K}_T$ of (n,m) SWNT are defined in term of the reciprocal basis vector $\boldsymbol{b}_1$, $\boldsymbol{b}_2$ and the number of unit cells by

$$\boldsymbol{K}_C = \frac{1}{N}(-t_2\boldsymbol{b}_1 + t_1\boldsymbol{b}_2), \quad \text{and} \quad \boldsymbol{K}_T = \frac{1}{N}(m\boldsymbol{b}_1 - n\boldsymbol{b}_2),$$

In an infinitely 1D solid, only vector $\boldsymbol{K}_T$ will span continuously along nanotube axis, while $\boldsymbol{K}_C$ defines the discrete integer multiples μ of k wave

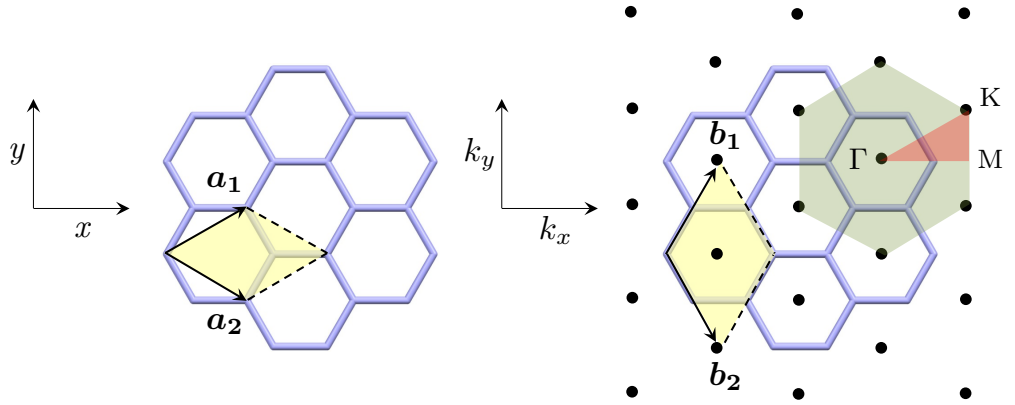

Figure 1.5: The unit cell in real space (left) and Brillouin zone (right) of graphene enclosed by the shadowed rhombus and hexagon in reciprocal (represented by black dots), respectively, and the high-symmetric points in the 2D Brillouin zone conventionally called Γ, K, and M points. The unit vectors and reciprocal lattice vectors are represented by $\boldsymbol{a}_i$ and $\boldsymbol{b}_i$ $(i = 1, 2)$, respectively.

vectors or cutting lines ($\mu \boldsymbol{K}_C$, $\mu = 1 - \frac{N}{2}, ..., \frac{N}{2}$). The $\mu \boldsymbol{K}_C$ will follow the circumferential direction to the exact two equivalent points in the reciprocal space, consequently, μ discrete value is always an even number with an even number of k vectors or cutting lines as shown in Figure 1.6.

1.2.3 Electronic structure of SWNT

Since the nanotube length is much larger when compared to its diameter, SWNT can be therefore though as one-dimensional (1D) nanostructure which the quantum confinement of 1D electronic states is taken into account. The σ bonds in 3D graphite give contribution on in-plane covalent bonds, π bonds respond to weak van der Waals interaction between graphene layers. In the sp^2 hybridization of SWNT structure, while the strong three σ-bonds are shared with three neighbor atoms, the remaining p orbital forms weak π bonds. Since π bands in SWNT are closed to the Fermi level, electron in the p orbital of π bands can be excited to the π^* bands, which is relevant to optical and electrical properties of the sp^2 carbon.

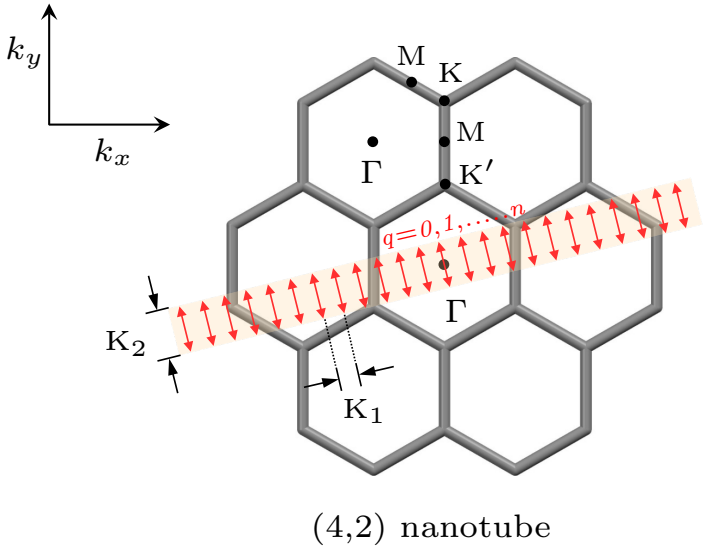

Figure 1.6: Cutting lines in the Brillouin zone for a (4,2) nanotube. The magnitudes of the reciprocal space vectors, $|\boldsymbol{K}_1| = 2/d_t$ and $|\boldsymbol{K}_2| = 2\pi/|\boldsymbol{T}|$, are calculated from $\boldsymbol{C}_h \cdot \boldsymbol{K}_1 = \boldsymbol{T} \cdot \boldsymbol{K}_2 = 2\pi$.

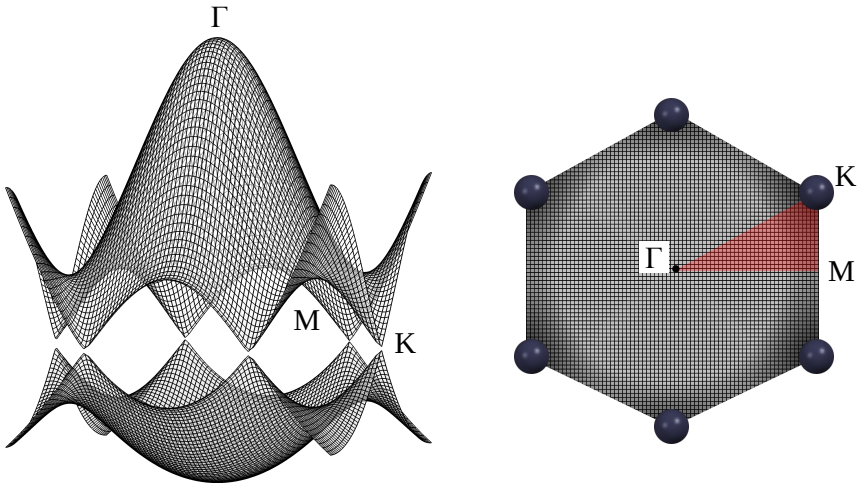

Figure 1.7: Illustration of the full three-dimensional bandstructure in the first Brillouin zone of graphene (left) with its couture map of π and π^* in electronic density of states in reciprocal space (right) [6].

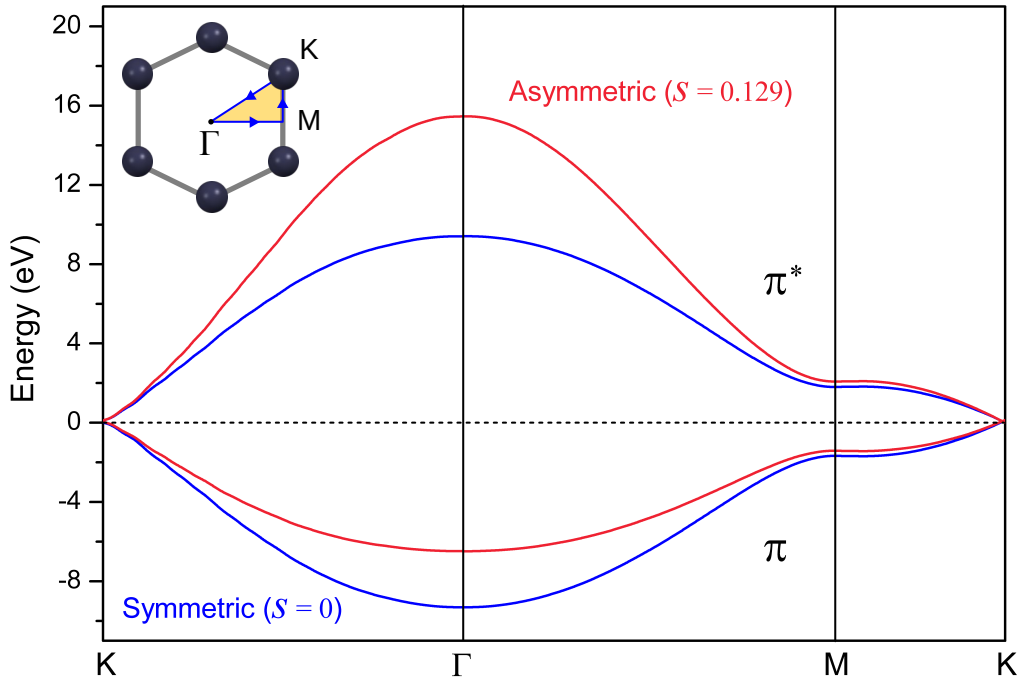

Figure 1.8: The energy dispersion relation of graphene along the triangle ΓMK in Equation 1.14. The parameters were $\epsilon_{2p} = 0$; $t = -3.033\,\text{eV}$; $s = 0.129$ [25] for the asymmetric dispersion relation, and $s = 0$ for the respective symmetric dispersion relation.

In real space, unit cell of SWNT is much larger that of a 2D graphene sheet, but the Brillouin zone (BZ) of the nanotube is much smaller that the BZ of a grapehene (Figure 1.7). Brillouin zone-folding technique has been generally used to obtain the energy $E(k)$ and phonon $\omega(k)$ dispersion relations. Using the definition of the structure of SWNT, its electronic structure can be obtained by a tight-binding calculation from 2D graphite. The energy dispersion relation of $2p$ in 2D graphite $E_{g,2\text{D}}(\boldsymbol{k})$ is given by

$$E_{g,2\text{D}}(\boldsymbol{k}) = \frac{\epsilon_{2p} \pm t\omega(\boldsymbol{k})}{1 \pm s\omega(\boldsymbol{k})}, \tag{1.14}$$

where ϵ_{2p} is the orbital energy of $2p$ orbital, t and s are, respectively, the transfer and overlap integral, and the signs of $\pm$ is given for bonding (π,+) and anti-bonding (π^*,-), while the 2D dispersion relation $\omega(\boldsymbol{k})$ is given

according to the relation,

$$\omega(\boldsymbol{k}) = \sqrt{1 + 4\cos\frac{\sqrt{3}k_x a}{2}\cos\frac{k_y a}{2} + 4\cos^2\frac{k_y a}{2}}.$$

The band structure of 2D graphene is shown in Figure 1.8. Due to the distance of π and the Fermi level in 2D graphene, the valence and conduction bands just touch one another at the $\boldsymbol{K}$ point, resulting in semi-metal property. In case of SWNT, its energy band gap can be though from the energy dispersion relations of 2D graphene. When the energy dispersion relation of 2D graphite is denoted as $E_{g,2\mathrm{D}}(k)$, thus N pairs of 1D energy dispersion relation $E_\mu(k)$ can be expressed by

$$E_\mu(k) = E_{g,2\mathrm{D}}\left(k\frac{\boldsymbol{K}_T}{|\boldsymbol{K}_T|} + \mu\boldsymbol{K}_C\right), \quad \mu = 0, ..., N-1, \text{and} -\frac{\pi}{|\boldsymbol{T}|} < k < \frac{\pi}{|\boldsymbol{T}|}$$

where k denotes the wave number along the SWNT axis. If these energy dispersion curves are collected (or folded) into the first Brillouin zone of the 2D graphite by translating them using multiples of $\boldsymbol{K}_C$ and $\boldsymbol{K}_T$. The wave vectors possibility in the case of SWNTs are limited from the case of 2D graphite. If the cutting line (along vector $\boldsymbol{K}_T$) pass through the $\boldsymbol{K}$ point, the 1D energy bands will have zero energy gaps and the density of state at Fermi energy level has a finite value, then that SWNT will be metallic. On the other hand, it will be semiconducting in the case of non-zero energy gaps when the cutting line does not pass through the $\boldsymbol{K}$ point. It can be simply described as

$$\text{properties} \begin{cases} \text{metallic} & \text{if} \quad \text{mod}\ (n-m, 3) = 0 \\ \text{semiconducting} & \text{if} \quad \text{mod}\ (n-m, 3) = 1, 2 \end{cases}$$

The formation of discrete bands is a result of the periodic boundary condition around circumference direction of the SWNT. Van Hove singularities are present in the resulting electronic density of state (Figure 1.9). Since the (6,5) nanotube is an intrinsic semiconductor, the density of state at

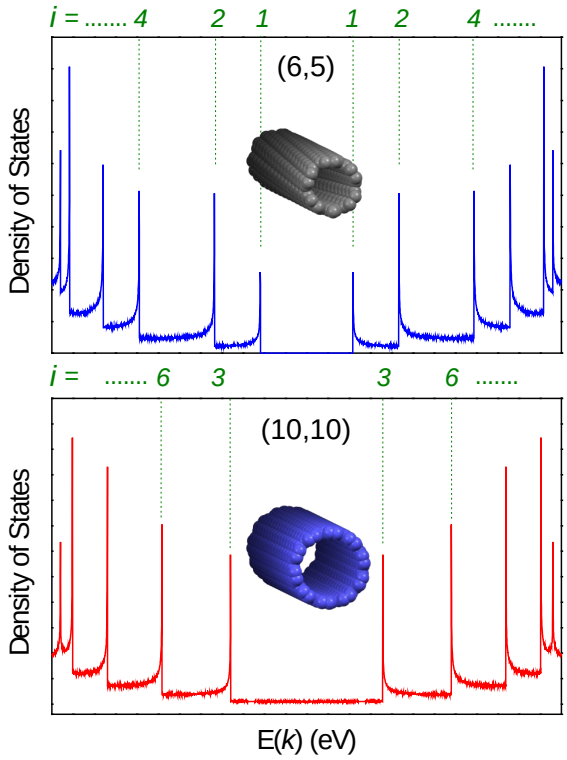

Figure 1.9: The density of states of semiconducting (6,5) and metallic (10,10) nanotubes. The density of states of nanotubes are reproduced from http://www.photon.t.u-tokyo.ac.jp/index.html.

Fermi level is zero. On the other hand, the density of state for the (10,10) nanotube is more than zero because it is inherently metallic.

Therefore, one of the most important characteristics of SWNTs is that the difference of metallic/semiconducting transport properties is determined by the chirality. Figure 1.10 shows the chiral mapping of (n,m) nanotubes that are either semiconducting (blue hexagons) or metallic (red hexagons). Any chirality is specified either by two integers (n,m) or equivalently. Among these, the nanotubes with m=0 (*i.e.* $\theta = 0°$) and n=m (*i.e.* $\theta = 30°$) chirality are termed of *zig-zag* and *armchair* types, respectively. This is because of their shapes at the edges that look like a zigzag and an armchair, but there is one type of SWNT which does not belong to both types that are called *chiral* type, as shown in Figure 1.10.

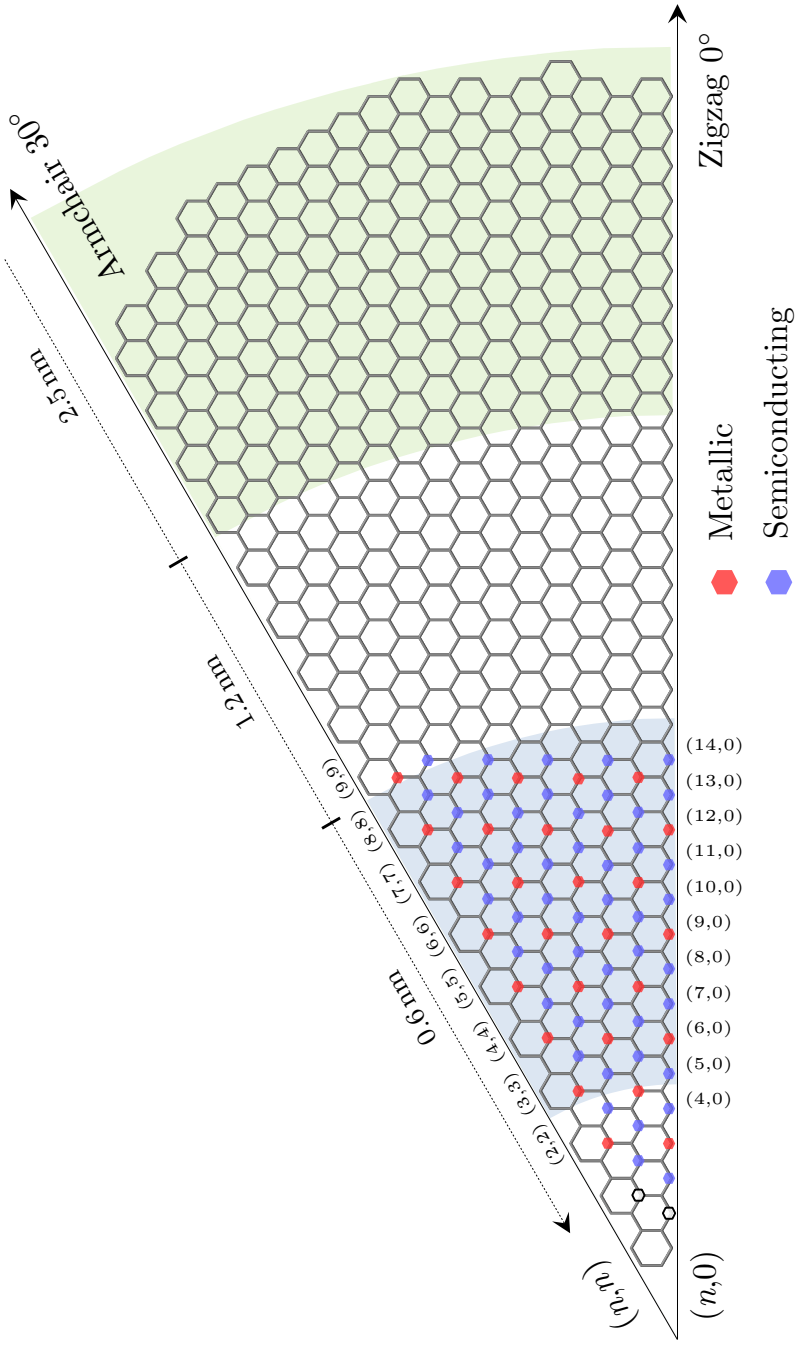

Figure 1.10: Representation of the symmetry-dependent electrical properties of SWNTs, where each dot corresponds to a specific chirality.

1.3 Electronic properties and spectroscopy

In this section, characterization methods on SWNTs would be presented to obtain information of electronic structure and diameter, including optical technique which is commonly used in nanotube field. Furthermore, electron microscopes are also employed for revealing the morphologies and structure of as-grown SWNTs. Even though electron microscopy sometime cannot give more information such as, diameter and impurity, it can be used to see larger area of sample than optical tools, where only small amounts or areas of sample can be only used.

1.3.1 Raman spectroscopy

1.3.1.1 Scattering process

Raman scattering the inelastic scattering of photon concerned with the phenomenon of change of frequency when light is scattered by molecules. The presence of scattered lines of shifted frequencies can be understood by considering the incident light to consist of photons of energy. For collision with a molecule, a photon may be elastically scattered without energy change, giving rise to the *Rayleigh scattering*, which is the most scattering event of the process. However, collision may be inelastic, they may cause the molecule to get a quantum transition to a higher energy level, which make the photon loses energy and is scattered with lower frequency. If the molecule is already in an energy level above its lowest, an encounter with a photon may cause it undergoing to a lower energy transition, which the photon is scattered with increased frequency. Thus, Raman shifts are equivalent to the energy changes involved to transitions of the scattering species. Raman shifts also correspond to vibrational or rotational transitions of the scattering molecules, but the photon is never absorbed, just rather perturbs the molecule and induces it to undergo this phenomena.

Considering the energy level of the scattering molecule by incident light with frequency ν_0 ($\Delta E_i = h\nu_0$) with initial energy gap between valence and

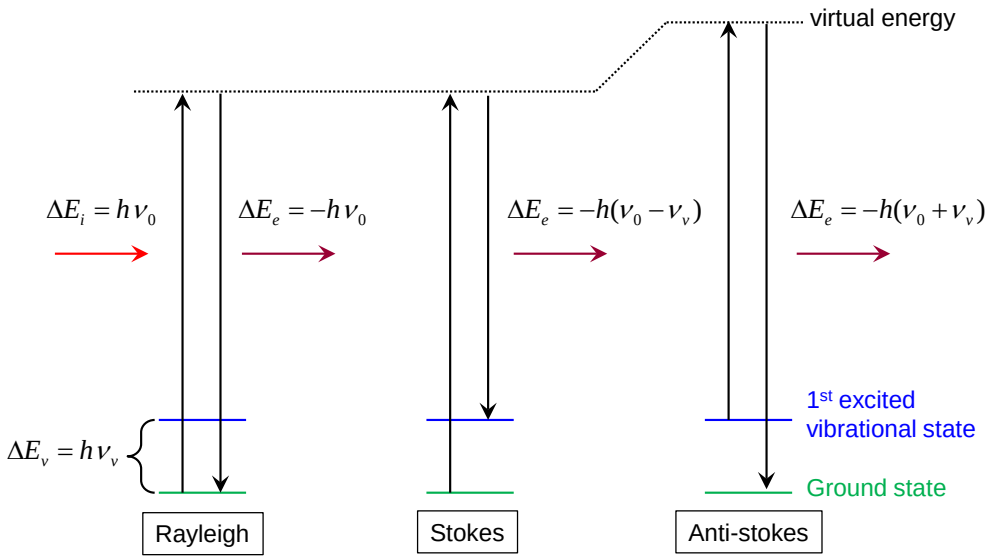

Figure 1.11: Excitation of scattering events in Raman scattering processes comprising of elastic (Rayleigh) and inelastic (stokes and anti-stokes) scatterings. The figure is adapted from http://en.wikipedia.org/wiki/Raman_scattering.

the first excited vibrational states of $\Delta E_v = h\nu_v$ as shown in Figure 1.11, the state of scattering molecule remains unchanged and the energy is conserved if incident and emitted photons have the same energy, resulting in elastic scattering called *Rayleigh scattering*. However, the excited electrons can either loss or adsorb more energy after scattering, which leads to the Raman effect. The *Stokes process* is the scattering event in which excited electron adsorbs energy and emit photon with less energy than the adsorbed photon $(-h(\nu_0 - \nu_v))$. Excited electrons, on the other hand, can also emit photon with more energy than adsorbed photon, so that emitted photon can reach ground state, resulting in the *anti-Stokes* scattering. Therefore, it can be note that the Raman scattering is incoherent and Rayleigh scattering is coherent. The events of scattering can be simply explained that (i) electron is excited from valence band to conduction band by absorbing photon, (ii) the excited electron is scattered by emitting or absorbing phonons, and (iii) the electron relaxes to valence band by emitting photons.

Resonance Raman spectroscopy are rich in information about structure, properties of nanotubes, and even impurity. It can also be used to identify nanotube diameter. SWNT has large unique and optical properties due to 1D confinement of electronic and phonon states, called *van Hove singularities* (vHS) in the nanotube density of state (DOS). The singularities in DOS and correspondingly in the electronic joint DOS (JDOS), are related for various optical phenomena. When a vHS in the JDOS of the valence and conduct bands is matched with the energy of incident photons, resonant enhancement will be occurred in the corresponding photophysical process, which is involved to the transitions in a molecular system. Therefore, resonantly enhanced Raman scattering allows this to obtain the information of vibrational properties of nanotubes. In SWNT for instance, Raman spectrum will be also depended on nanotube orientation as obtain from single crystal sample [26].

1.3.1.2 Raman spectroscopy of SWNTs

Resonance Raman scattering by excited laser is powerful tool to characterize nanotube structure due to its unique property of electronic density of state, which is expressed in term of chirality (n,m). This results in different energy in singularities of SWNT and different resonance. This signal can be used identify the (n,m) structure of SWNT. In Raman scattering process, electron can emit one, two, or multiple phonons after scattering depending on scattering events as seen in different Raman shifts and peak shapes (Figure 1.12).

The most dominant feature of Raman mode is tangential mode, which provides a signature and nature of carbon nanotube [27]. This mode involves to one-phonon emission or first-order Raman corresponding to a resonant excitation of *in-plane* optical phonons, which appears around $1960\,\mathrm{cm}^{-1}$ for 2D graphite. Since SWNT has different structures compared with that of graphite for the axial and transverse in-plane vibrational modes, the tangential G mode in nanotubes will give a multiple-peak feature, named

G-band. The G-band position is slightly different in energy (*i.e.* different in Raman shift). This energy difference causes energy of G band to split into two peaks: G^+ and G^- peak, where G^+ has higher energy. The G^+ and G^- indicate atomic displacement along the tube axis and circumferential direction, respectively. The G^- feature can be used to identify the difference of semiconducting and metallic SWNTs. In the presence of free electrons in case of metallic nanotube, the feature of the G^+ is soften and broadened from Fano resonance, called *Breit-Wigner-Fano* (BWF) lineshape [28–30], resulting in lower frequency than G^-. On the other hand, the frequency of G^+ is higher than G^-, and no BWF Fano resonance is observed with the Lorentzian lineshape for semiconducting nanotubes [30].

Another first-order Raman mode that only appears in carbon nanotubes, is called *radial breathing modes* (RBM band) as shown Figure 1.12). This RBM mode corresponds to coherent atomic vibration of the carbon atoms in radial direction, and is used to distinguish SWNTs in the sample. This mode is resonance *out-of-plane*, which vibrates perpendicular to lattice plane and opposite to G mode [31], and in resonance when the energy of the incident photons matches with the energy gap E_{ii} in DOS of each SWNT, giving rise to different frequency of RBM peaks that usually appear in the range of 100–400 cm^{-1}.

The absorbed photon can also scatter from $\boldsymbol{k}$ to $\boldsymbol{k}+\boldsymbol{q}$ states, and scatters back to $\boldsymbol{k}$ state before recombining with hole and emitting a photon at a $\boldsymbol{k}$ state. By scattering with defects or impurity, scattering events in this case will be one elastic and one inelastic events, caused by defects in sample, called *one-phonon double-resonance Raman spectra*. Frequency of emitted phonons is dispersive with different excitation energies [32–34]. Hence, information of defects or impurities can be obtained from resonance Raman spectroscopy, which is identify by broad feature of disordered band (D band) around 1350 cm^{-1} as shown in Figure 1.12. The sharper feature, on the other hand, comes from nanotube structure itself (high curvature of nanotube). Usually, both of these features are overlapped to each other. On the other

hand, The so-called *two-phonons double-resonance Raman spectra* can also occurred when emitting phonon scatter with another emitting phonon. This scattering event will give rise to Raman shift of about 2700 cm^{-1}, called *2D* or *G′* band.

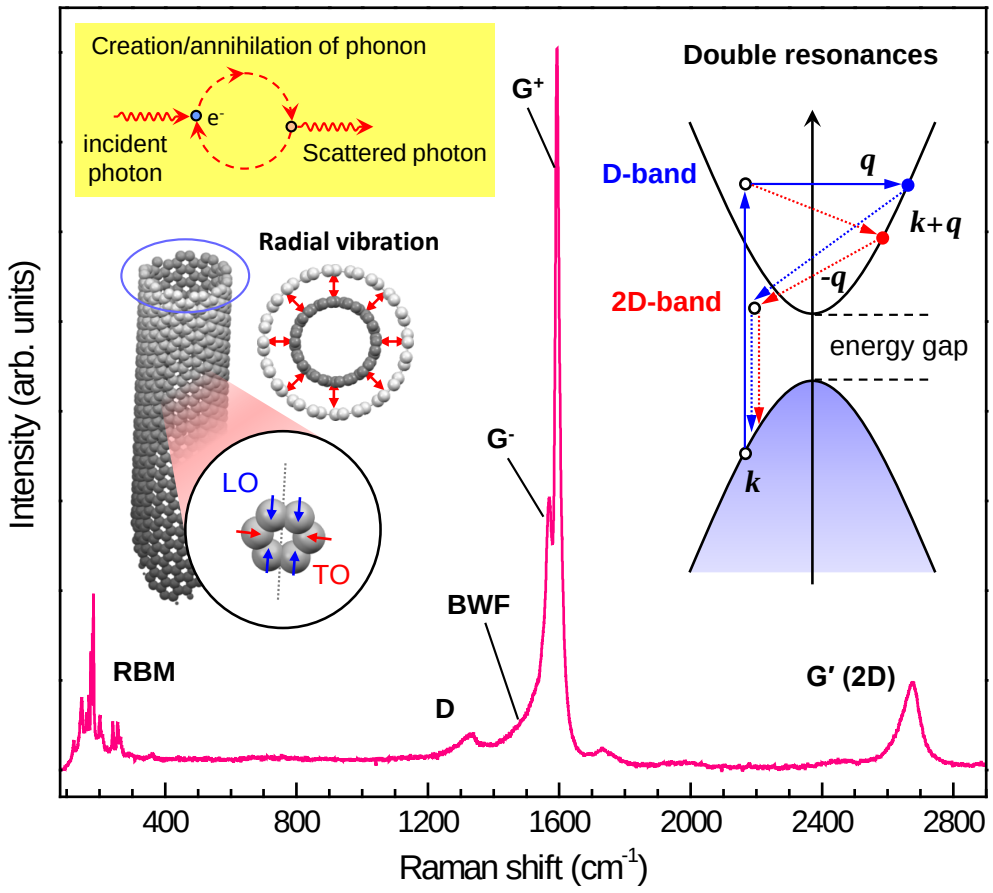

Figure 1.12: A resonance Raman spectrum from vertically aligned SWNTs excited by 488 nm excitation laser, shows typical different resonance Raman modes; RBM (100-400 cm^{-1}), G-band (1594 cm^{-1}), D-band (1320 cm^{-1}) and G′ (2D) band (2680 cm^{-1}). Different vibration modes are illustrated, and the scattering event for D-band and G′ band is explained by illustrated double-resonance phonon scattering.

1.3.2 Optical spectroscopy

1.3.2.1 Absorption in general

In optical absorption spectroscopy, it is used to characterize with incident light in the range of ultraviolet and visible radiation, which is the near infrared region of the electromagnetic spectrum (around 1500–3300 nm), called *UV-Vis-NIR* spectral regions. Once light in the range of UV-Vis-NIR collide with medium, it will be adsorbed before passing through medium, depending on light propagation. From Beer-Lambert law (Figure 1.13), the absorbance of a sample is proportional to the thickness of the sample and the concentration of the absorbing species in the sample, the intensity of absorbed incident light is found to be exponential decreased as in the equation $I(L) = I_0 exp^{-\alpha Lc}$, where I_0 is the intensity of incident light, I_L is the intensity of light at optical path length L, α is the absorption coefficient and c is concentration of absorbing species in the material. The absorbance which is related to the incident intensity, can be expressed in terms of intensity from the following equation

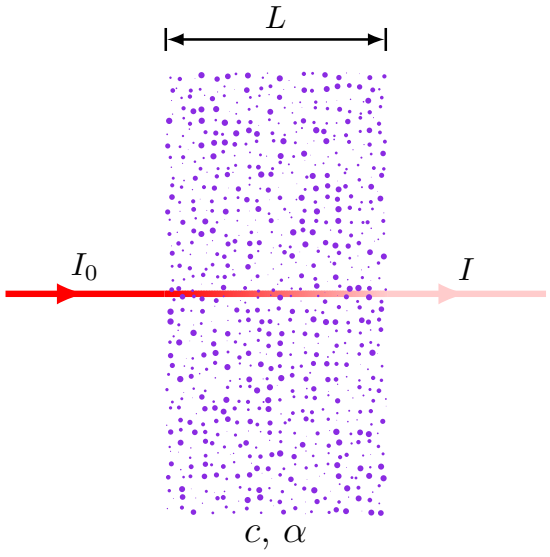

Figure 1.13: Schematic of light absorption through medium. The figure is reproduced from http://www.texample.net/.

$$A = -\log_{10} \frac{I}{I_0},$$

where A is an absorbance of material at a given wavelength. Thus, we obtain the correlation of UV-Vis-NIR light and absorbance for each molecule in material, and we can use it to characterize the structure of material. Moreover, features of absorption spectrum correspond to electronic states of materials, which can be also used to characterize electrical structure of materials. In general, many properties of materials, especially optical property, such as bonds or composition inside materials, optical tools are often used to assist by the principle of optical absorption because optical properties are direct consequence of the electronic nature of materials. In semiconducting and metallic materials, their band structures are different that they are overlapped for metallic materials, and split out to be gap for semiconducting. The electron can cross to the conduction band much easier for metallic materials, but energy is needed to excite the electron in valence band to cross over the gap reach to conduction band since there is small gap in between two bands.

1.3.2.2 Optical transition of SWNT

In one-dimensional material as SWNT a unique feature of its DOS is discrete energy of state, unlike continuous DOS as in three-dimensional materials as shown in Figure 1.14. Both metallic and semiconducting SWNTs exhibit vHSs in their DOS depending on chirality, which involve to valence and conduction bands. Meaning that diameter of nanotube is inversely proportional to energy transition as expressed by Kataura plot (Figure 1.15, left panel). Hence, diameter of nanotubes can be evaluated by absorption energy (*i.e.* absorption wavelength). The electrical structure is a bit different from general materials due to restriction of the energy transitions with symmetry considerations [35], which is depended on the polarization of incident light to nanotube axis that results in highly anisotropic absorption. Absorptivity will be strongest when the polarization parallel to SWNT

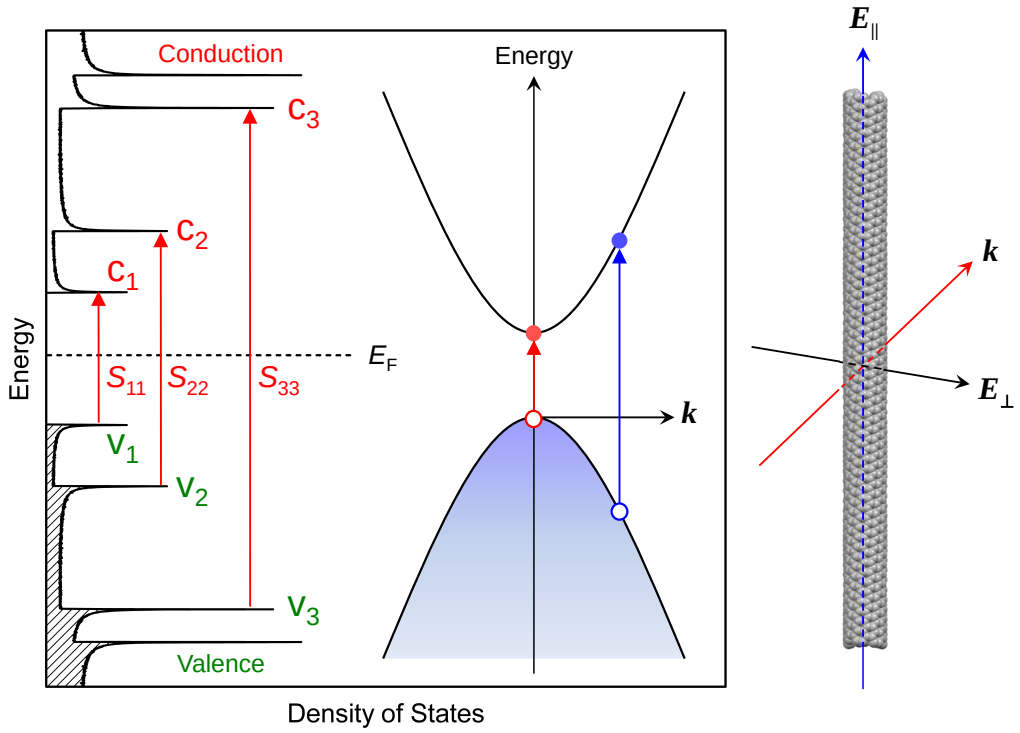

Figure 1.14: Example of van Hove Singularity (vHS) of semiconducting (7,5) nanotube. This vHS is reproduced from http://www.photon.t.u-tokyo.ac.jp/index.html.

axis, and weakest when polarization perpendicular to SWNT axis. The optical transition is generally occurred from valence state to conduction state with same order of transition (*i.e.* $v_1 \rightarrow c_1$, $v_2 \rightarrow c_2$, $v_3 \rightarrow c_3$,...). These transitions are represented as E_{11}^{S}, E_{22}^{S}, E_{33}^{S},..., or S_{11}, S_{22}, S_{33},... for semiconducting nanotubes, and E_{11}^{M}, E_{22}^{M}, E_{33}^{M},..., or M_{11}, M_{22}, M_{33},... for metallic nanotubes. However, crossover transition ($c_1 \rightarrow v_2$, $v_2 \rightarrow c_1$,...) can be observed by cross-polarized optical absorption [36]. Energy separation differences can be resolved by different absorption energy that will show up in different absorption peaks. However, the transition process of photon occurs in UV-Vis-NIR range. The first (E_{11}) and second (E_{22}) electronic transitions of bulk SWNTs can be distinguished by the optical absorption spectroscopy. Due to bundle formation of nanotubes, the E_{11} peak is broaden

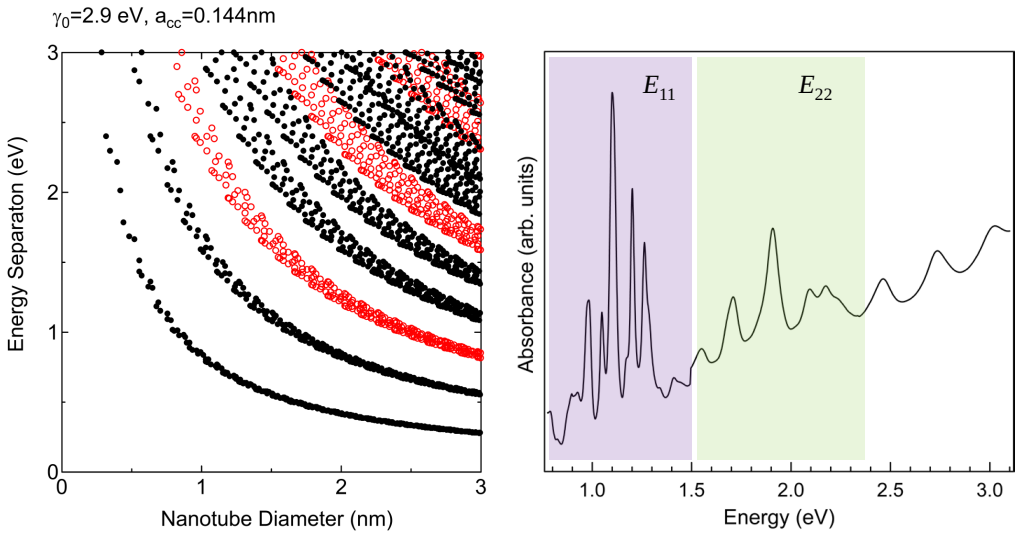

Figure 1.15: Kataura plot of nanotube diameter correlated with band gap energy (energy separation) of various chiralities (left), and an example of absorption spectrum of dispersed SWNTs synthesized from HiPco process. Kataura plot is reproduced from http://www.photon.t.u-tokyo.ac.jp/index.html.

and cannot be easily resolved because of nanotube population. The mean diameter of bulk SWNTs is, therefore, evaluated from the E_{11} and E_{22} transitions by comparative with Kataura plot [37]. However, well resolvable of the E_{11} transition can be seen in dispersed nanotubes. Figure 1.15 (right panel) shows optical spectrum of dispersed SWNTs synthesized by HiPco process, which can be simply obtained by dispersing nanotubes using sodium deoxycholate (DOC) as a surfactant (see more detail in Section 1.4.2.2). The E_{11} and E_{22} and M_{11} electronic transitions are well resolved. The presence of different chirality can be assigned. Therefore, optical absorption spectroscopy can efficiently give information about the structure of SWNTs and their mean diameter.

1.3.2.3 Photoluminescence Excitation spectroscopy

In semiconducting materials, photons can be absorbed (electromagnetic radiation) and re-radiated again. This can be expressed as an excitation to a higher energy state before returning to a lower energy state accompanied by the emission of a photon, called *photoluminescence* (PL), which is used to measure purity and crystalline quality of semiconductors. On the other hand, no excitonic luminescence can be produced in metallic materials in which electron is excited resulting in optical absorption, but hole is immediately filled by another electron out of many available in metal. Thus, PL cannot be used for metallic materials because of lack of exciton production. The simplest PL processes are resonant radiations, in which photon of a particular wavelength is absorbed, and an equivalent photon is immediately emitted. This process involves no significant internal energy transitions of the chemical between absorption and emission. Interestingly, when the chemical undergoes to internal energy transitions before re-emitting the energy from the absorption event, the fluorescence will be occurred. Many kinds of PL are existed depending upon the aspect of fluorescence. Time-resolved photoluminescence (TRPL) is also one of methods. This PL is a very sensitive technique to resolve overlapping absorption signals of defects, or to distinguish emission signals by their different time decay features, where the sample is excited with a light pulse and then the decay in PL with respect to time is measured. This technique is useful in measuring the minority carrier lifetime of semiconductors for elements in group of III-V.

Another specialized form of PL is phosphorescence, in which the energy from absorbed photons undergoes intersystem crossing into a state of higher spin multiplicity, usually a triplet state. Once the energy is trapped in the triplet state, transition back to the lower singlet energy states is quantum mechanically forbidden, meaning that it occurs much slower than other transitions. The result is a slow process of radiative transition back to the singlet state, sometimes lasting minutes or hours. This is the basis for “glow

in the dark" substances. In addition, another form of PL which is also well known, is photoluminescence excitation (PLE). In the case of material as SWNT, this PLE is used as powerful and efficiency method to characterize electrical, optical properties, specific tube structure, and chirality of SWNTs because of its special 1D structures and vHSs.

As stated before, PL measurement has some optical limitations that it can be used to characterize semiconductors. Thus, PLE is also limited for only semiconducting nanotubes (*i.e.* not fluoresce with metallic nanotubes) and small-diameter SWNTs. When the incident light is passed through

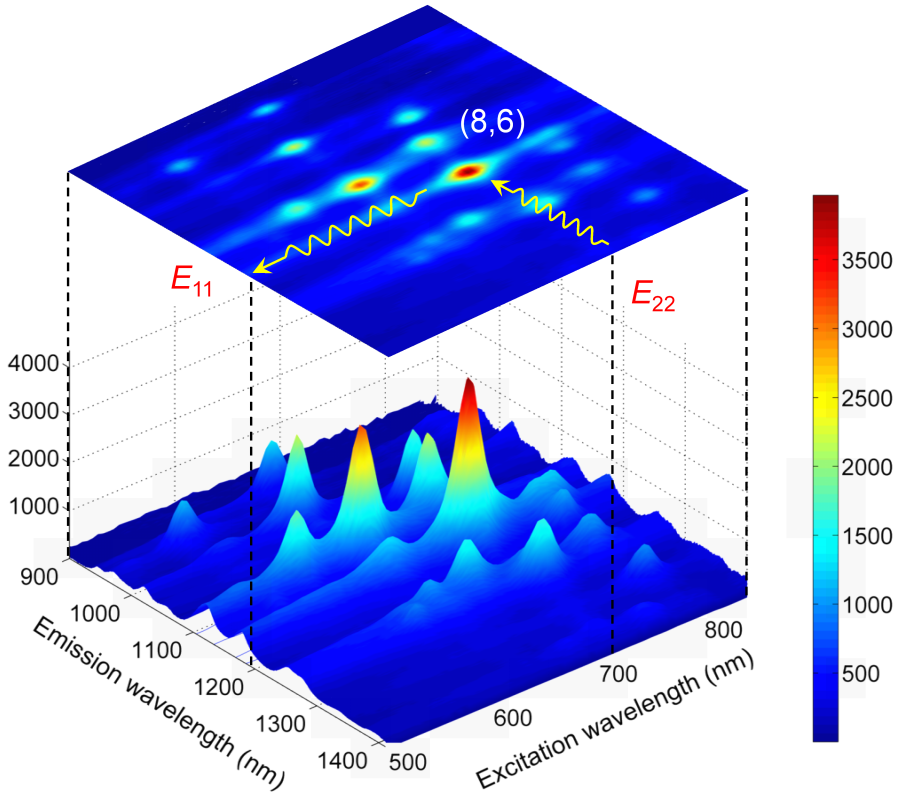

Figure 1.16: The photoluminescence excitation (PLE) map of dispersed SWNTs synthesized from HiPco process which is described by the density of electronic states in which electron is excited by photon with excitation energy of E_{22} before decaying to the first electronic transition with emission transitions equal to E_{11}.

the SWNT sample, light will be absorbed by electron at photon energy of the E_{22} ($v_2 \rightarrow c_2$), which will create an exciton (electron-hole pair). An excited electron and hole will relax and back to the lowest energy state (*i.e.* E_{11}) with emitted photon energy near energy of the E_{11} ($v_1 \rightarrow c_1$) before recombining of electron-hole pair at the lowest energy state. Meaning that both energy transitions will be changed with different chiralities. Thus, in PLE map, each distinct peak corresponds to emission from the first electronic band gap (E_{11}) of a semiconducting nanotube as shown in horizontal axis, which has first been excited to the second band gap (E_{22}) in vertical axis. Each peak also corresponds to specific chirality of SWNT that shows up with different peak intensity corresponding to population of that chirality as shown in Figure 1.16. PLE spectroscopy also correlates with optical absorption spectroscopy in which optical transition can be characterized in the same way. However, PLE signal is reduced as increasing aggregation of individual nanotubes in which PLE signal is quenched due to bundle formation [38]. Even though it is difficult to characterize nanotube bundles, PLE spectra could be observed in some cases [39–42].

1.3.3 Photoemission spectroscopy

An electron can be taken out by photo-induced photon energy when incident photon energy is greater than electron binding energy as known as photoemission, which was later on explained by Einstien with photoelectric effect [43]. Once photon with energy of $h\nu$ is absorbed by an electron in a solid which are very close to the surface, an electron with absorbed energy greater than summation of binding energy ($B.E.$) and workfunction of a solid (ϕ) will be lifted above a vacuum level with certain kinetic energy ($K.E.$), which is simply given by $K.E. = h\nu - B.E. - \phi$.

The same photoemission event can occur with an x-ray photon in which photons are produced from x-ray beam so called *x-ray photoelectron spectroscopy* (XPS). In XPS measurement as shown in Figure 1.17, photo-emitted electrons excited from x-ray beam and leaving from surface in ultra-high

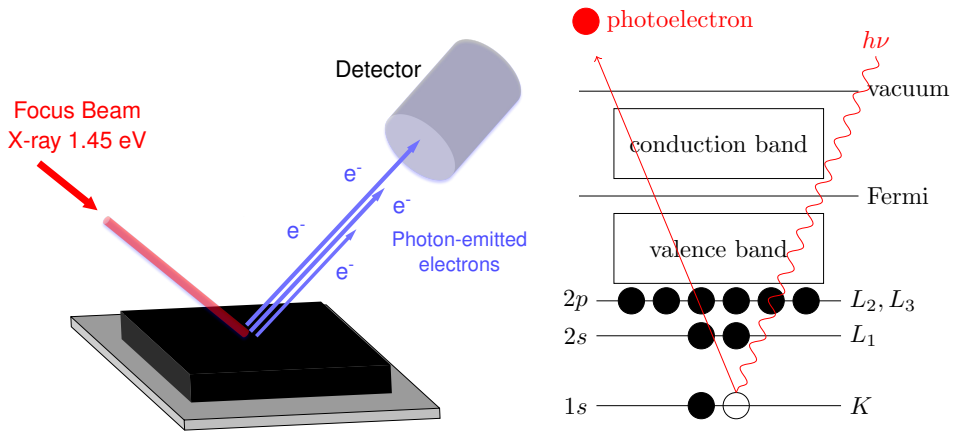

Figure 1.17: An artistic impression of photoemission event in which an photo-emitted electron is excited by x-ray photon energy (left) and raised up from K-shell to vacuum level with the energy of $h\nu$ (right). The figure in right panel is reproduced from http://www.texample.net/.

vacuum (UHV) will be collected by detector. It is basically measured to term of photonelectron intensity and bind energy, which is characteristic of core electron for each element. Each peak in XPS spectrum corresponds to electron configurations within the atom (*e.g.* *1s*, *2s*, *2p*, *3s*,...), and represents number of photo-emitted electrons from the element at a certain binding energy. Atomic percentage value can be calculated by dividing signal intensity (or peak area) by relative sensitivity factor and normalized overall with elements detected, and is dependent of atomic cross section of each atom. It is, therefore, a surface analysis technique which is useful for elemental identification, chemical state, relative composition, and valence band structure in surface scale.

XPS can also be used to identify carbon hybridization in carbon materials. Graphite is carbon material consisting of sp^2 hybridization. On the other hand, nanodiamond or amorphous carbon has sp^3 hybridization which has higher binding energy. Hence, C1s peaks will show up in different peak position (*i.e.* different binding energy). In case of clean SWNTs (Figure 1.18), an sp^2 C configuration is basically the only hybridization presented in the

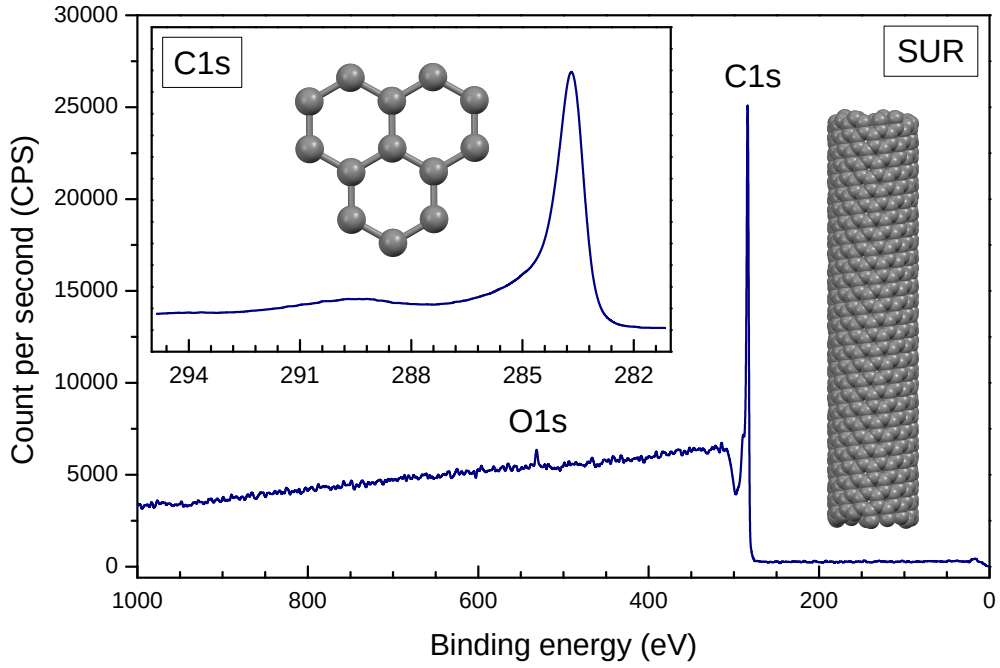

Figure 1.18: An example of x-ray photoelectron spectrum showing a clean survey scan spectrum and C1s core level of sp^2 from SWNTs (inset).

sample that gives rise to a strong asymmetric Doniach-Šunjić lineshape [44] of C1s core level at about 284–287 eV with a weak broad peak of π-π^* transition at about 290 eV.

1.3.4 Near-edge x-ray absorption spectroscopy

X-ray absorption spectroscopy (XAS) is method used to characterize electronic structure in crystal materials by exciting electrons in conduction band with photon energy from x-ray. X-ray is generally from Synchotron which can provides tunable high energy x-ray beam. The encounter high energy photon have to be adequate to lift electron from core shell into the conduction band. Another electron from valence band will later on fall in the electron hole in the atomic core shell. While valence band electron is falling down, the photon energy will be released and transferred to the third electron the outer shell prior to exciting into a vacuum state so call *Auger*

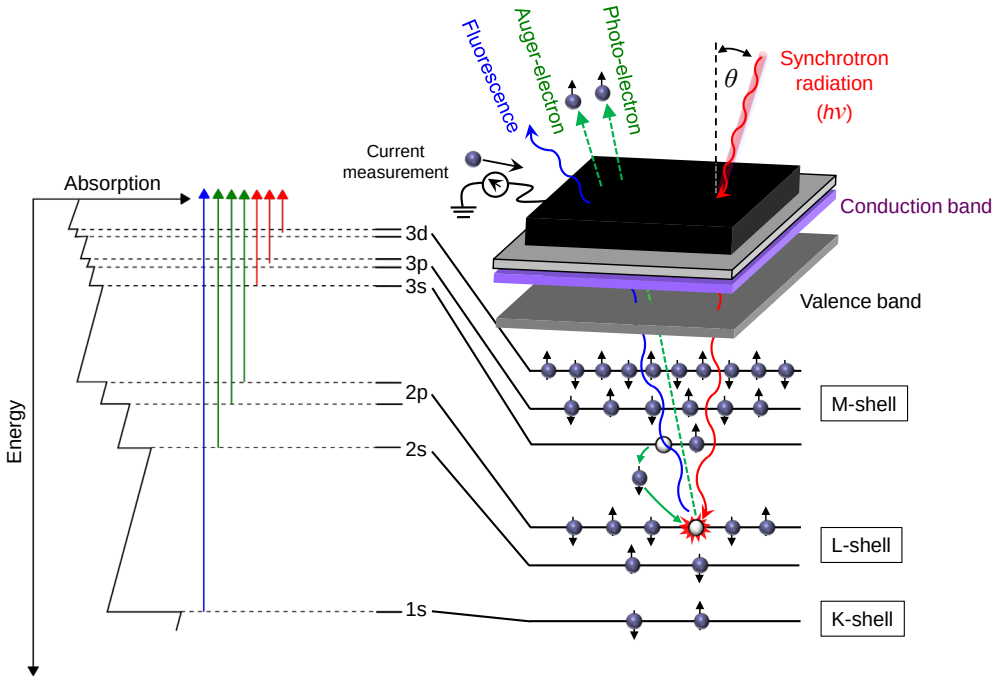

Figure 1.19: Schematic representation of the Auger process in near-edge x-ray absorption. Lost electron is refilled again by additional electron, which is used to measured at different photon energy. The figure of absorption fine structure is reproduced from http://en.wikipedia.org/wiki/X-ray_absorption_spectroscopy.

electron. The Auger electron is also measurable as a function of photon energy which is highly surface sensitive, similar to XPS. Upon photo energy hits on the sample in which conductive sample is required, it can either make transmission through the sample or yield photoelectrons leaving from sample, which causes the loss in photoelectrons depending on absorption coefficient. Since sample is conducting, loss in photoelectrons can be compensated by applying current through the sample. This can be accurately performed and measurable in term of drain current as illustrate in Figure 1.19.

The absorption close to the absorption edge additionally gives the largest variations in the intense and narrow resonance of x-ray absorption, resulting in fine structure of the sample. Hence, The so-called *near-edge x-ray absorption fine structure spectroscopy* (NEXAFS) is used to identify absorption

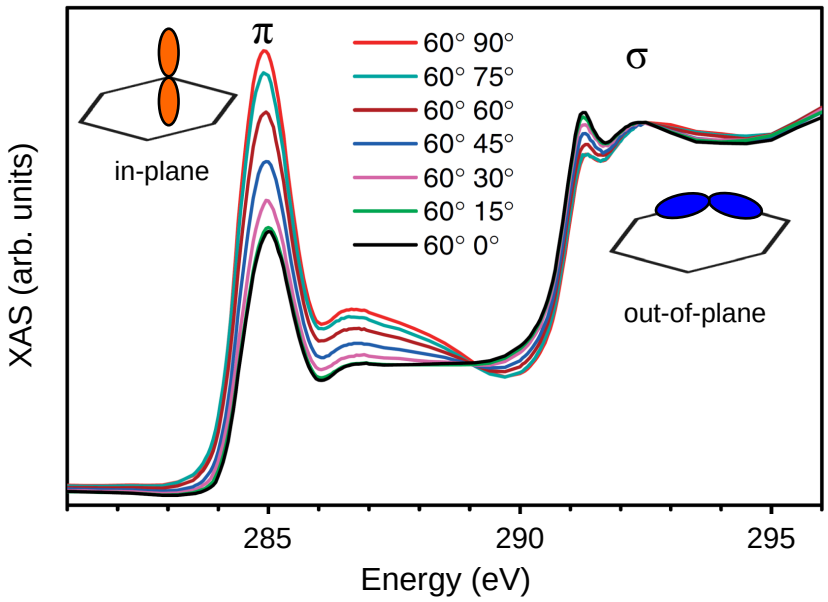

Figure 1.20: An example of near-edge x-ray absorption fine structure (NEXAFS) spectrum of VA-SWNTs with polarization-dependent x-ray absorption. The figure is reproduced with permission from [45], Copyright © 2007 by John Wiley & Sons.

edge structure. The NEXAFS can also give an information of σ-σ^* and π-π^* transitions of the sample, unlike XPS in which σ-σ^* transition cannot be seen. These σ and π orbitals are dependent of polarization of the linear x-ray beam. They can be, therefore, clearly revealed using polarized x-ray beam which is one importance aspect of NEXAFS. Figure 1.20 shows an example of polarization dependence of C1s of VA-SWNTs in NEXAFS. The π and σ signal response to their orientations.

1.3.5 Electron microscope

Electron microscopy is widely used in many fields of studies because of its necessity. It is often used to examine morphology or thorough information of samples. There are many kinds of electron microscopy depending on purpose of studies, but their principles are basically similar, in which electron

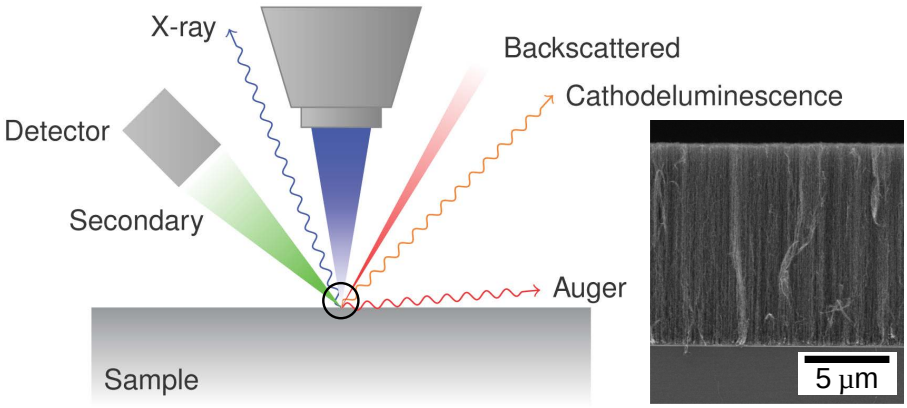

Figure 1.21: The principal of scanning electron microscopy (SEM) imaging emitted secondary electrons from SWNT sample. The schematic of SEM is reproduced from http://www.texample.net/.

beam is used to image morphology or structure of sample. The resolution of electron microscope can be from low to high resolution depending on desired magnification, which can be reach to 100 000× depending on type of microscopes. One of the most common electron microscope is *scanning electron microscopy* (SEM), in which images are produced by scanning an electron beam over a sample in a raster pattern cross surface, and then detecting the scattered secondary electrons, the emitted electrons from the surface are recorded as shown in Figure 1.21. The image is then shown in 3D image. However, the electron beam is not projected through the whole sample area. This generates a lower-resolution image, but allows the direct mapping of surface features. Another kind of SEM, which can improve resolution, is a *field emission SEM* (FE-SEM) by using a field emitter to obtain an intense electron beam.

Besides there is another kind of electron microscope Figure 1.22 that is capable of even higher magnification (over 1 000 000×). Instead of detecting scattered electrons from sample, it rather detecting electrons that have passed through the sample (transmission). A microscope operating on this principle is called a *transmission electron microscope*, or TEM. This is

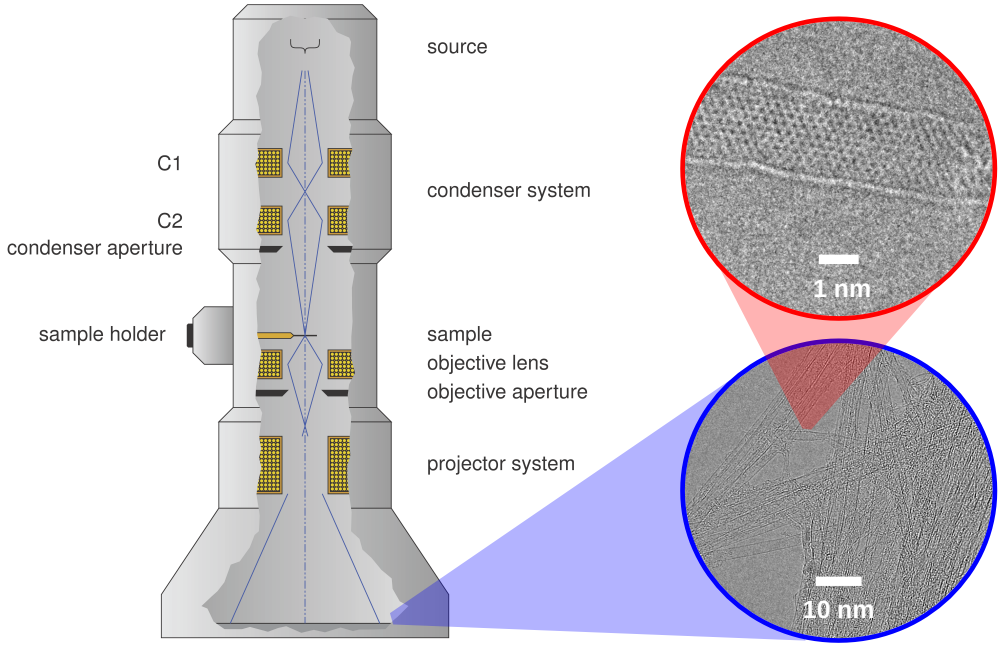

Figure 1.22: The principal of transmission election microscope (TEM) in which the dispersed SWNTs are imaged by excited electrons passing through the sample (blue), and a high-resolution TEM (HRTEM) image of individual SWNT showing nanotube wall and carbon atom network (red). The schematic of TEM is reproduced from http://www.texample.net/.

accomplished by accelerating electrons to high energies (typically $> 100\,\mathrm{keV}$) and special process of sample preparation so that it is thin enough for the incident electrons to pass through, and the resulting pattern of electron transmission and absorption is magnified onto a viewing screen. The image generated is, however, a 2D map of the sample's density, which can be used to map topography in thin samples. A good TEM is capable of atomic resolution, thus gives an extremely accurate picture of the crystal structure of a material, which can be even performed at high resolution (HRTEM) and can give reliable statistical information, diameter and chirality distribution of SWNT, and impurities inside sample. The HRTEM image of SWNTs produced from alcohol is shown in Figure 1.22 (red). The single-layered tube wall, C-C bond length, and chirality can be identified from the image.

1.4 Synthesis and bulk SWNTs

1.4.1 Synthesis of SWNTs

Synthesis of zero-dimension (0D) bucky fullerenes in 1985 by R. E. Smalley's research group [46] was the major breakthrough for future generations of carbon in which they were awarded to the Nobel prize in chemistry in 1996. Soon after discovering 0D carbon, it again amazed all researchers with discovering missing 1D carbon known as carbon nanotube in 1993 by Iijima [47]. By meanwhile, there were many attempts to study on single-walled structure along with many reports on experimental study. SWNTs were discovered by Iijima and Ichihashi [47, 48] in 1993, following their discovery, higher quality of SWNTs with a few defects, such as the arc discharge [49] and laser over method [50] methods could be produced. By meanwhile, they could not be produced in required scale for most experiments. Another simple new method was developed again by H. Dai and coworkers at R. Smalley's laboratory at Rice University by producing SWNTs with chemical vapor deposition (CVD) [51], in which carbon monoxide (CO) was used as a carbon source for CVD growth that reacted with metal catalyst particles inside a heated reactor. Because of its simple and controllable, this method became the most common for SWNT production. In the late 1990, it was the first time that gram-scale quantities of SWNTs could be synthesized with high reproducibility by synthesizing at high pressure using the same CO as carbon source by the same research group. This process was a high-pressure disproportional reaction of CO (HiPco) [2] due to synthesis method. This process was popular and widely used at many laboratories in the world, and had been become important and many significant advancements. The 2D carbon allotrope as graphene, on the other hand, has been finally discovered by A. Geim and K. Novoselov in 2004 [4, 5] in which they were awarded to the Nobel prize in 2010. It seems that carbon nanotube research has been faded upon graphene was discovered. Still, impressive properties of carbon nanotube have aroused many researchers to continue researching on

nanotube. Carbon nanotube has been proven to be much more wonderful 1D material. Nevertheless, many challenges in nanotechnology still need to be improved and investigated.

1.4.2 Alcohol-catalytic CVD

With the variety of synthesis methods on SWNT production, impurities of as-synthesized product (*i.e.* amorphous carbon, multi-walled carbon nanotubes, and catalyst particles) always come along with nanotube formation. Nevertheless, this problem was minimized when alcohol was used as the carbon feedstock gas [52]. The nanotubes synthesized from alcohol contain less impurities with high percentage of SWNT existing. Once alcohol (*i.e.* ethanol) is decomposed, the OH radical in ethanol reacts with carbon molecules that have dangling bonds and etches them away, resulting in less amorphous carbon [3, 52]. The so-called *alcohol catalytic chemical vapor deposition* (ACCVD) has become one of the most popular methods with low-cost and high-purity of SWNTs. The understanding of growth mechanism on ACCVD process is, however, not yet well explored. Consequently, the reaction of a carbon-containing molecule with a metal catalyst particle before precipitating a nanotube in the general CVD process is still

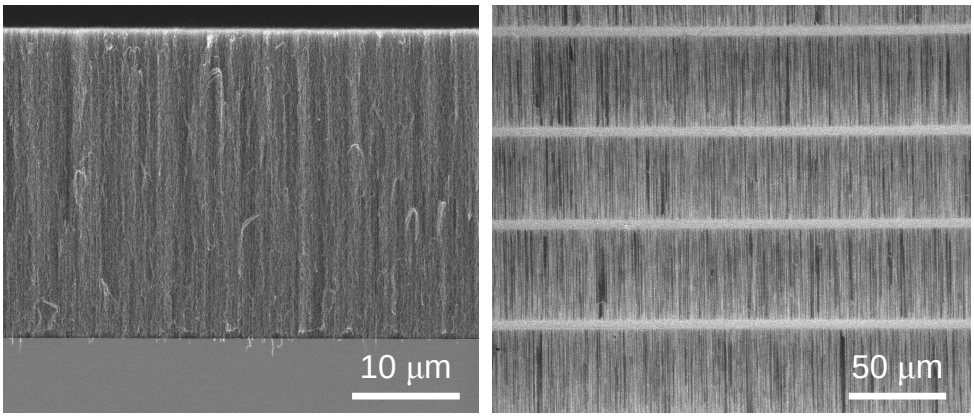

Figure 1.23: Example of different morphology of SWNTs synthesized from ethanol: vertical align (left panel), and horizontal align (right panel).

being investigated by many different methods, including molecular dynamics simulations [53].

Many properties of SWNT are anisotropic, thus control over the orientation is highly desirable for exploiting these anisotropic properties. Controlling over the diameter of nanotubes during synthesis is, therefore, one of crucial purposes to meet a requirement for high performance application. Another key parameter correlated to anisotropic properties of nanotubes, is their morphology. In all of synthesis methods together with advance in nanotube research, many forms of nanotube morphology can be successfully synthesized such as random structure, vertically aligned [54], and horizontally aligned [55–57] SWNTs as shown in Figure 1.23. The combined simple and lost-cost ACCVD with catalyst deposition processes allow us to investigate key parameters that affect on nanotube diameter and their morphology as the following Section.

1.4.2.1 Catalyst loading

A *liquid dip-coating process* [58] was firstly introduced to produce vertical aligned fashion of SWNTs. It is an easy and simple process by just dip-coating substrate into catalyst solution. Initially, cobalt (Co) acetate $[(CH_3COOH)_2Co{\cdot}4\,H_2O]$ and molybdenum (Mo) acetate $[(CH_3COOH)_2Mo]$ with desired metal concentration of 0.01 wt.% each – depending on desired morphology – were dissolved in each batches of 40 g ethanol. The catalyst loading was performed by submerging an optically fused quartz, and/or silicon substrates into a separated catalyst solution batches. Once substrate was immersed into Mo-acetate solution for 3 min, it was then withdrawn from the solution at speed of $4\,\mathrm{cm/min^{-1}}$, and baked in air at 400°C for 5 min to remove the acetate and oxidize the metals prior to reproducing this process with the Mo-coated substrate with Co-acetate solution as illustrated in Figure 1.24. The resulting dip-coated and oxidized metal catalysts on substrate are nearly uniform with mono-dispersed catalyst particles $105\,\mathrm{particles}/\mu\mathrm{m}^2$ with diameters of approximately 1.5 nm [59]. Furthermore, formation of

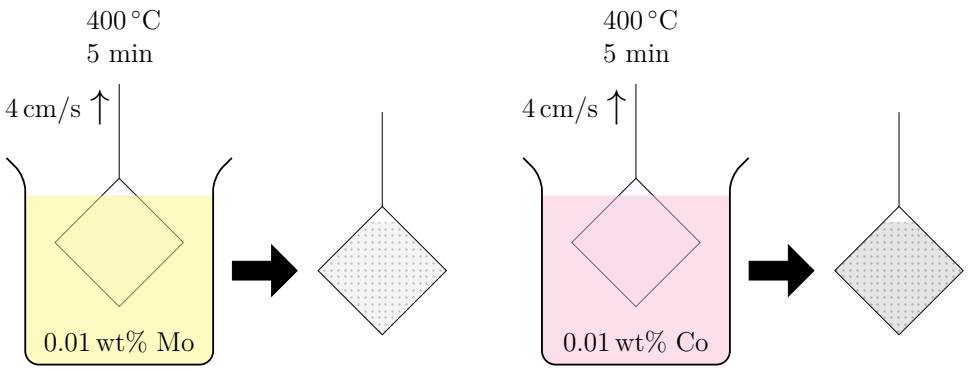

Figure 1.24: Schematic of dip-coating process.

oxide after baking resists and prevents agglomeration of catalysts on the substrate surface at high temperature (growth temperature, *e.g.* 800°C).

Another catalyst loading used to gain high yield and reduced the diameter of SWNTs, is *impregnation* process. With this process, the morphology of nanotubes can no longer be controlled in the vertical orientation. The catalyst powder was prepared by using impregnation of Co and iron (Fe) catalysts. The preparing process is followed previous report [3, 52], which was developed from the procedure originally presented by Shinohara research group [60, 61]. Co-acetate (105.7 mg) and iron acetate $[(CH_3CO_2)_2Fe]$ (77.8 mg) were dissolved in 40 mL of ethanol along with 1 g of USY-type zeolite powder (TOSOH Corp. HSZ-390HUA, over 99% SiO_2). The concentration of each metal species over the total catalyst powder is 2.5 wt.%. The mixture was bath sonicated for 1 h. It was then dried in a oven at 80°C for 24 h to remove ethanol solvent. The resultant brown powder was ground into fine powder by a mortar and stored in oven at 80°C for future use.

1.4.2.2 SWNT dispersion

Characterization process can be in general performed on as-synthesized SWNT samples. Some of optical processes are, however, restricted to individual nanotubes or small nanotube bundles, which allow to access important details of nanotube structures (*i.e.* diameter, chirality). In pho-

toluminescence process, bundling effect can incur an exciton recombination that quenches photoluminescence signal which the electronic transition of SWNTs cannot be seen. On the other hand, it can be observed from the optical absorption spectroscopy even in bulk nanotube sample, but no specific chiralities can be observed. In order to overcome this problem, debundling process is necessary to individualize nanotube sample. Thus, liquid-based process is required for homogeneously dispersion. Additionally, it also allows carbon nanotubes to be applied for some applications such as, thin film fabrication [62–64], or solution-based field effect transistor (FET) [65–67].

Dispersion is generally required for the early step of nanotube separation process [68–70], which can be simply performed by dispersing nanotube sample in solution (D_2O, H_2O, *etc.*) with desired surfactants that act as stabilizer. Efficient surfactants are usually sodium dodecylbenzene sulfonate (SDBS), sodium dodecyl sulfate (SDS), sodium deoxycholate (SDC). Carbon nanotube solution after mixing with 0.1 % DOC, for example, will be mildly sonicated to dissolve surfactant, and debundled by ultrasonicating before centrifugating to removed undesired nanotube bundle that stay on the bottom part of dispersion. The supernatant is finally extracted for further characterization or applications.

Chapter 2

Nitrogen-doped SWNTs

The nanotube properties are in general difficult to control as they are pristine with broad diameter distribution. Even though they can be modified by indirect diameter tuning, the electrical property is still not suitable for some specific applications. Some other methods to isolate individual SWNTs for electrical fabrication have, therefore, been recognized as nanotube separation [68–70]. In order to separate nanotubes into each chirality, the SWNT sample needs to be firstly dispersed with surfactant, ultrasonicated, and centrifuged before passing through density-gradient process [70]. The separation process seems to be well expected for the future electronic device fabrication, the resultant SWNTs from this process are, however, found to be defective and shortened due to incorporation of surfactants and strong cutting effect from ultrasonication. Thus, another possible way beside separation is direct post-treatment by chemical doping to modify charge transfer state [16–18]. The doping process can also be performed during growth process by introducing any carbon feedstocks containing desired dopants which introduce heteratoms into carbon lattice, while nanotubes are growing [71–73].

2.1 Electronic states of N-doping SWNTs

Simultaneous doping during synthesis generally requires dopants which have suitable atomic sizes as carbon atom depending upon desired electronic structures, for instance p-type, feedstocks are often chosen to contain boron (B) which always need one more electron to fulfill its stable bonding in the sp^2 carbon network. Electronic modification as p-type behavior can be, however, easily observed in the presence of atmosphere due to their sensitivity to oxygen [74]. Nitrogen (N), on the other hand, has brought considerable attention on carbon materials [75–80], including graphene [81–84] for n-type characteristic in which N has one more free electron that exhibits electron donor behavior that has become one of envisioned motivation in nanotube field. Meanwhile, incorporation of N in carbon nanotube or graphene can also enhance adsorption reactivity that have been investigated on oxygen reduction and gas sensor applications [85–90].

It has become more attractive when N configuration incorporated into sp^2 carbon network can turn into many different configurations during synthesis, resulting in different intrinsic properties (Figure 2.1). Nitrogen-doping can be defined as nitrogen is incorporated into sp^2 carbon network. It was found that there are three main nitrogen configurations in sp^2 carbon network are which may occur as (i) pyridinic, (ii) graphitic (substitution, sp^2), and (iii) pyrrolic nitrogen structures. Figure 2.1 shows variety of nitrogen configurations in sp^2 graphene structure. These three structures affect on electronic and transport properties differently. In the pyridic structure of nitrogen, nitrogen atom is two-fold coordinated, and contribute one p electron to the π band. The hybridization of pyrrolic nitrogen structure is similar to that of pyridinic one, but nitrogen atom is formed sp^3 coordination, and two p electrons will stay at the π state. Note that it is not necessary for nitrogen to stay in a five-membered ring as pyrrolic structure. Since electrons suit the π state, these two configurations of nitrogen doping, therefore, exhibit as electron acceptor or p-type doping for pyridinic configuration, and neutral for pyrrolic configuration. On the other hand, the one electron suit the π^* state when

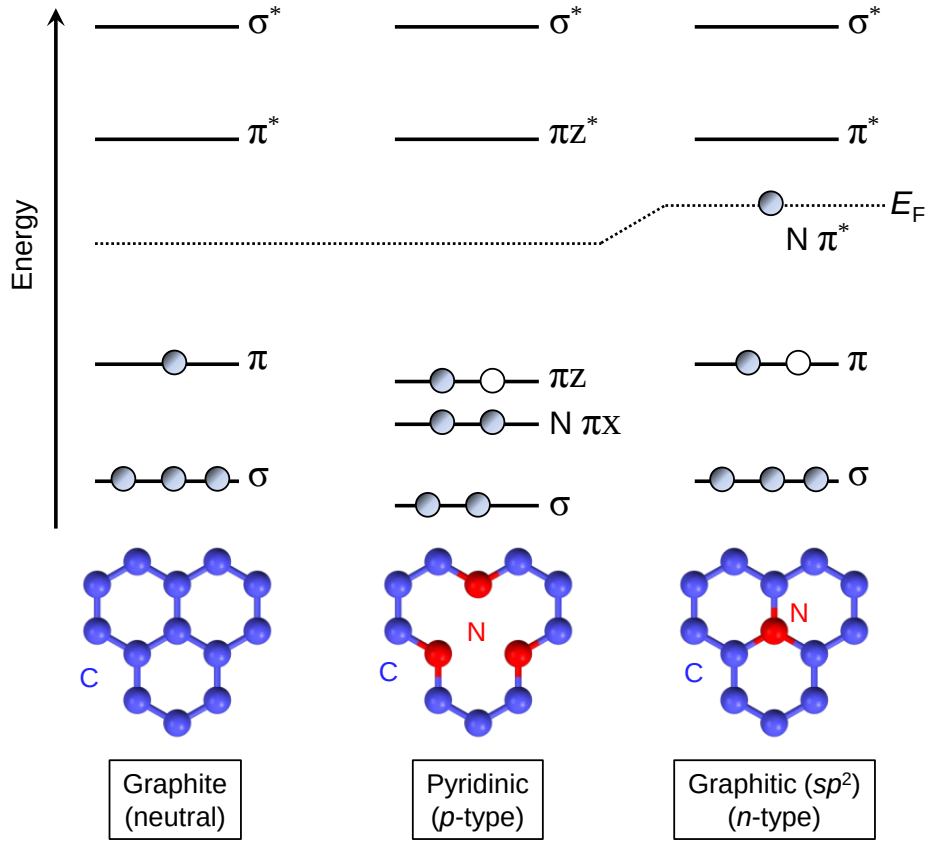

Figure 2.1: Illustrated nitrogen configurations-dependent electronic properties of nitrogen-incorporated SWNTs.

carbon atom is replaced (substituted) with nitrogen atom in the network (*i.e.* sp^2 formation). Meaning that three electrons contribute to σ bonds with three surrounding carbon atoms, left only one unused electron in the π state. This free electron is, however, forced to occupy the π^* state, resulting in the localized states (impurity level) above the Fermi level [78, 91, 92], which acts as electron donor. The substitutional nitrogen is, therefore, expected to have the *n*-type characteristic as observed in carbon nanotubes [92] and graphene [81, 83, 84].

However, depending on predominance of existing nitrogen configurations, nitrogen doping can cause a change in electronic property as *p*- or *n*-type. Figure 2.2 show an example of *n*-type characteristic of the σ^* observed

in the N site incorporated sp^2 C lattices of single-layered graphene [84]. Although an incorporation of nitrogen heteroatom can create the impurity level to upshift or downshift close to conduction and valence bands, due to electric dipole moment the electron back backscattering from the dopant states is increased, which causes a lower in conductance, especially pyridinic site [78, 93], and decrease in mean free path [94].

2.2 Doping-dependent diameter change

Synthesis of N-doped carbon nanotubes have been studied by many different synthesis processes [95–104]. While carbon nanotubes are being synthesizing, nitrogen can either leave the system or incorporate into a network of sp^2 carbon structure as pyridic, substitutional, or pyrrolic sites. It has been suggested that N-doped carbon nanotubes are in general contributed as bamboo shape by pyrrolic contribution [103] with minority of substitutional, and pyrrolic structures. The content of nitrogen incorporated in carbon nanotube walls is dependent of the solubility of nitrogen in the catalyst at growth temperature [96]. Although this nitrogen content is proportional to N-containing feedstock concentration, most of nitrogens do not contribute in nanotube formation [98, 104].

While nitrogen doping seem to induce more defective than pristine undoped carbon nanotubes [71], nitrogen incorporation causes the diameter change. As nitrogen is incorporated or doped during growth process, tube diameter seems to be changed in the presence of more nitrogen source but the reason for constrained nitrogen content remains unclear. An slight increasing in the mean SWNT diameters from 1.6 to 1.67 nm has been previously shown by just introducing 500 ppm of ammonia with carbon feedstock [105]. It should be noted that ammonia (NH_3) can also act as etching agent for carbon nanotubes or nanofibers [106]. It is in this case plausible that ammonia may selectively etch away small-diameter SWNTs presented in the sample. Contrarily, a mean diameter tends to be reduced

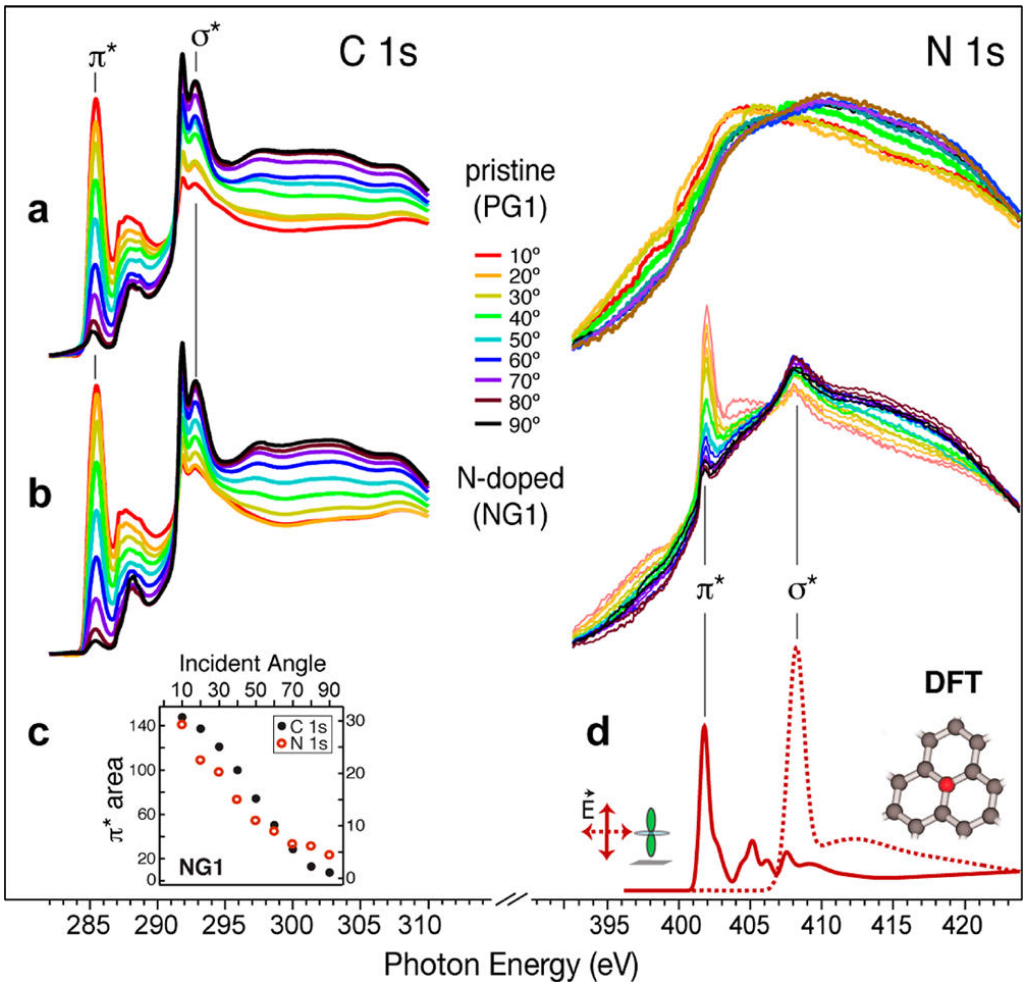

Figure 2.2: (a, b) X-ray absorption spectra (XAS) of the C1s (left) and N1s (right) absorption edges show clear π^* and σ^* resonances of carbon and nitrogen in N-doped graphene, indicating electron-donor state of incorporated N confirmed by the density functional theory (DFT) calculation (d), and (c) polarization dependence of π^* state of C edge indicates in-plane orientation in graphene. The figure is reproduced with permission from [84], Copyright © 2012 by The American Physical Society.

when feedstock used contains nitrogen radical. A reduction in diameter was found in N-doped SWNTs when acetonitrile concentration in ethanol is increased with the maximum nitrogen content of $\sim 1.5 \pm 0.02$ at.% [107]. Similar work has also been reported on the same acetonitrile feedstock [108].

Ibrahim and co-workers [108] found a significantly change in nanotube mean diameter from 1.8 to 0.86 nm when acetonitrile mixtures were 0 and 100%. The nitrogen content was in this case ~ 2 at.% in maximum. As the SWNT diameter decreases, the energy formation seems to favor pyridinic-divacancy configuration rather than forming substitutional nitrogen site to lower the energy formation [109], while substitutional nitrogen configuration seems to be more favorable in graphene [83, 84]. Further studies on nitrogen configuration-controlled process consequently need to be deserved to identify dopant configuration and electronic property in SWNTs.

Even though there have been many intensive studies on growth mechanism of pristine nanotubes (undoped) either from experimentally or theoritically, it is still explicitly unclear due to the complexity of carbon feedstock and the interaction of catalyst to active molecules. It is even more sophisticated when nitrogen is presented in the precursor. Growth process can either occur via based or root growth mechanisms. For N-doped carbon nanotubes, it generally responsible to growth of bamboo-like morphology that can occur via based growth [110, 111] or root growth processes [112]. This simple mechanisms can be easily observed by how carbon material are growing. The further detailed growth mechanism is, however, still under discussion. It has been assumed that a precursor is dissociated at the catalyst before C and N prior to cracking CN bond [111]. This may imply the reason why there is the presence of nitrogen gas inside carbon materials [113–117]. Simulation results at the first stage of N-doped carbon nanotube growth [118–121] seem to shade light to a more clear image of how nitrogen act at the catalyst, but further studies on the role of nitrogen needs to be addressed.

Chapter 3

Synthesis of small-diameter VA-SWNTs

3.1 Introduction

The ability to tune the electrical and optical properties of SWNTs is a long-standing goal of nanotube synthesis. SWNTs synthesized by conventional methods are inherently devoid of chirality control. However, their electronic properties may be controlled indirectly by narrowing the diameter range to confine the number of possible chiralities. Supporting materials and templates [1, 122–126] have been used to influence the diameter of SWNTs via catalyst morphology or cap formation [127], although these nanotubes still require additional post-processing in order to extract them from the supporting (powder) materials. A potentially non-templated approach to control the nanotube diameter is by the choice of carbon feedstock, such as carbon monoxide [1, 122], ethanol (EtOH) [123], methane [128], acetylene [129], ethylene [130], or other organic chemical sources [131]. Acetonitrile (AcN; CH_3CN) has been used to synthesize nitrogen (N)-doped carbon nanotubes [79, 90, 101, 107, 108, 132–135], and some groups have reported a reduction in SWNT diameter due to the presence of nitrogen [107, 108]. Pint and co-workers [132] have also recently scaled up N-doped

SWNT synthesis by a water-assisted approach using acetonitrile as the C/N feedstock.

Here I employ pure and mixed EtOH and/or AcN feedstocks to grow vertically aligned (VA-) SWNTs by no-flow CVD from Co/Mo binary catalyst. The mean diameters of the VA-SWNTs synthesized from identically prepared catalyst particles are as different as 2.1 nm for pure ethanol feedstock and 0.7 nm for pure AcN feedstock. If a mixed feedstock is employed, the atomic nitrogen concentration saturates at 1.2 at.%. This saturation correlates with the decrease in mean diameter.

3.2 Diameter modulation by acetonitrile

3.2.1 Synthesis of small-diameter VA-SWNTs

VA-SWNT arrays [54] were synthesized from Co/Mo binary catalyst by a no-flow CVD process [136] using mixtures of acetonitrile and ethanol as the carbon feedstock. This mixture was varied from 0% to 100% acetonitrile by volume (hereafter just %), and all other parameters were kept unchanged as reported in Ref. [136]. Catalyst was loaded onto fused quartz substrates by dip-coating into separate solutions of Mo-acetate and Co-acetate dissolved in ethanol (metal species content 0.01 wt.% each). The process is based on that described in Ref. [58]. During heating of the CVD system, the Co/Mo binary catalyst were reduced under Ar containing 3% H_2 at a flow rate of 300 sccm and a pressure of 40 kPa. After reaching the growth temperature of 800°C in 25 min, the system was evacuated and then sealed before introducing 40 μL of feedstock. The feedstock was introduced all at once, but the vapor pressure soon stabilized at approximately 1.7 kPa. The reaction time was 3 min in all cases, and after synthesis the CVD chamber was evacuated and cooled to room temperature while flowing 300 sccm Ar. As-grown VA-SWNT arrays were characterized by scanning electron microcopy (SEM, 1 kV acceleration voltage, S-4800, Hitachi Co., Ltd.), UV-Vis-NIR absorption spectroscopy (UV-3150, Shimadzu Co., Ltd.)

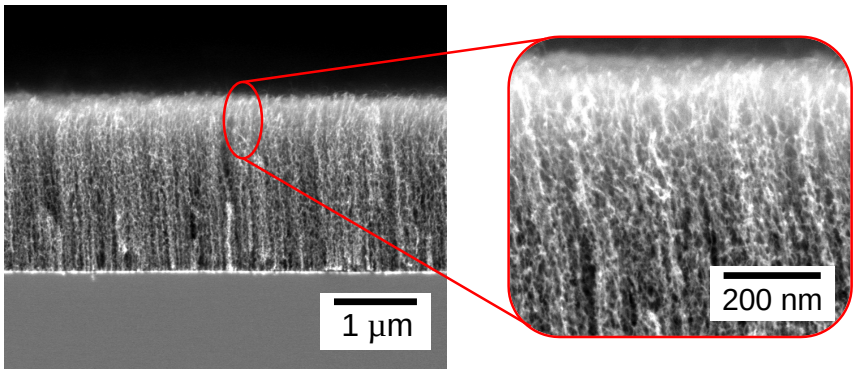

Figure 3.1: SEM images of a VA-SWNT array synthesized by no-flow CVD using pure acetonitrile as a feedstock. Adapted with permission from [137], Copyright © 2012 by John Wiley & Sons.

and resonance Raman spectroscopy (Chromex 501is with Andor DV401-FI) using excitation wavelengths of 488 and 633 nm. For transmission electron microscopy (TEM, JEOL 2000EX operating at 120 kV), the SWNTs were dispersed in ethanol and the dispersion was dropped onto Cu microgrids. For X-ray photoelectron spectroscopy (XPS, PHI5000 VersaProbe, 1.486 keV), VA-SWNT arrays were transferred [138] onto a Si wafer (50 nm oxide layer) and heated to 250°C for 10 min to dehydrate the sample. For further UV-Vis-NIR and photoluminescence excitation spectroscopy (PLE, HORIBA Jobin Yvon Fluorolog *i*HR320, equipped with a liquid-nitrogen-cooled GaAs detector), SWNTs synthesized on USY-zeolite powder [3, 52] using mixed feedstocks were dispersed in 5 mL D_2O with 1 wt.% sodium deoxycholate (DOC) surfactant. The fluorescence emission wavelength range was recorded from 900 to 1400 nm, while the excitation wavelength was scanned from 500 to 850 nm in 5 nm steps. After bath sonication for 10 min and an additional 30 min of ultrasonication (Hielscher Ultrasonics GmbH UP400S with H3/Micro Tip 3 at a power flux level of 400 $W \cdot cm^{-2}$), the suspension was centrifuged for 15 min at 85 000 rpm (327 000 g). Finally the supernatant was extracted. The supernatant was also used for further XPS measurements of a SWNT film formed by vacuum filtration [139]. The dispersed SWNT film thickness was examined to be more than 30 μm.

3.2.2 Characterization of small-diameter VA-SWNTs

Ethanol (EtOH) is a well-established carbon source for SWNT synthesis [3, 52]. Figure 3.1 clearly shows the capability of AcN to act as a source for VA-SWNT synthesis [54]. The film thickness is found to be thinner than for VA-SWNTs synthesized from conventional alcohol catalytic CVD [52, 54]. TEM images in Figure 3.2 show clean SWNTs are obtained from both pure EtOH (left) and pure AcN (right). In fact, no catalyst particles

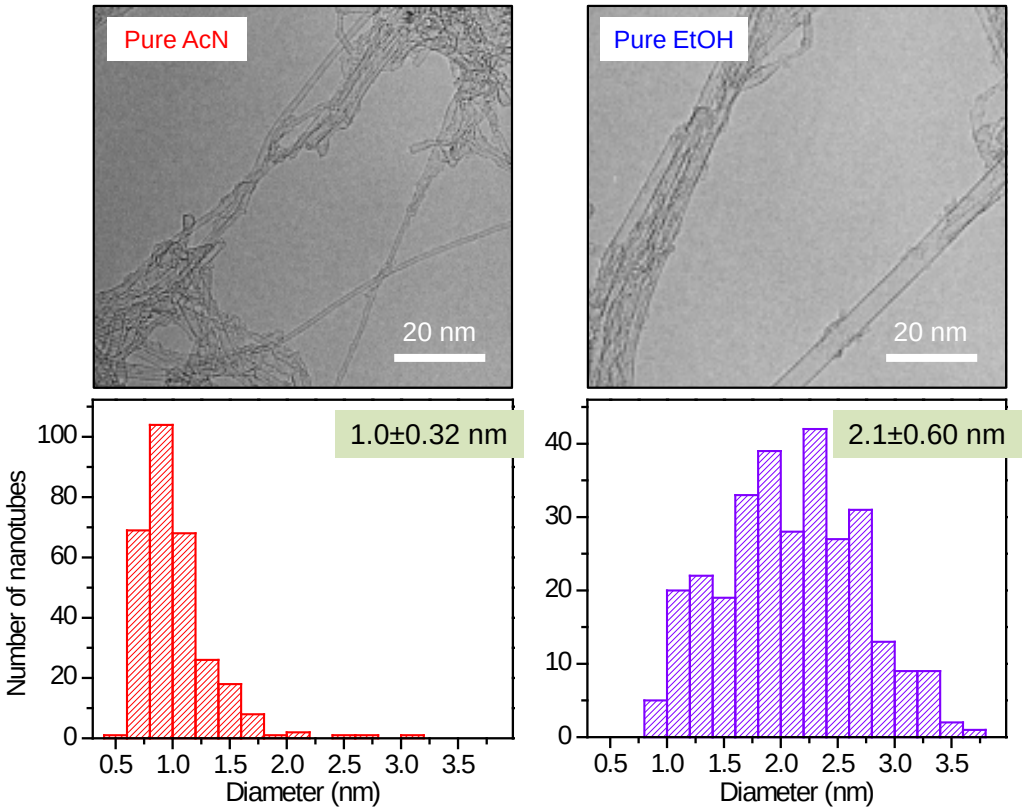

Figure 3.2: TEM micrographs of SWNTs grown from pure acetonitrile (AcN) and pure ethanol (EtOH). The vastly different diameters are directly visible, and shown by histrograms of SWNT diameter distributions obtained from TEM observations of pure EtOH-grown and pure AcN-grown SWNTs with the number of measurements $N = 300$ for each case. The observed mean diameters are 2.1 ± 0.60 nm and 1.0 ± 0.32 nm for pure EtOH and pure AcN, respectively. TEM images are adapted with permission from [140], Copyright © 2012, Elsevier.

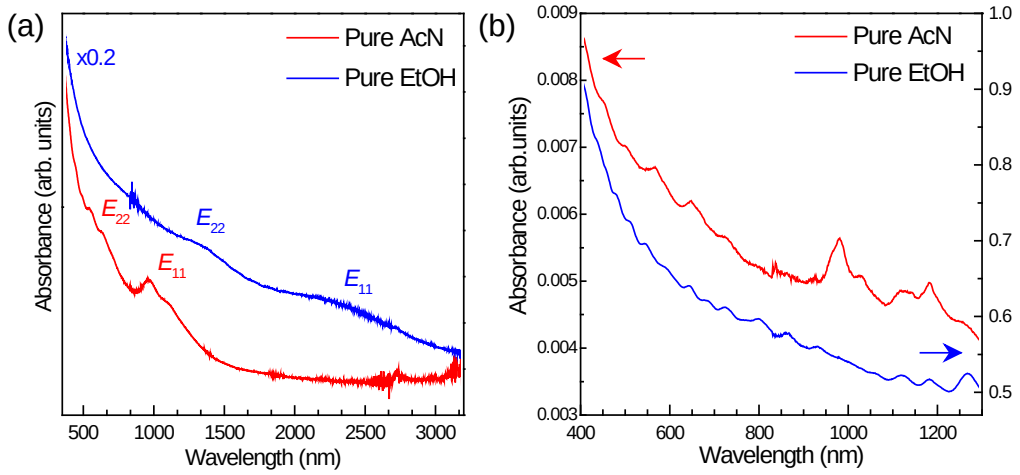

Figure 3.3: (a) Optical absorption spectra of as-grown VA-SWNTs synthesized with different feedstocks show a dramatic difference in the first optical transition energies E_{11}^S [140], and (b) shows optical absorption spectra from SWNTs dispersed in D_2O using DOC as a surfactant. Adapted with permission from [140], Copyright © 2012, Elsevier, and permission from [137], Copyright © 2012 by John Wiley & Sons.

were encountered during TEM observations. Visual inspection of TEM micrographs show significantly narrower SWNTs are synthesized from pure acetonitrile feedstock.

Optical absorption spectra are shown in Figure 3.3. The first optical transitions (E_{11}^S) are observed at 2250 nm (0.55 eV) and 1000 nm (1.24 eV) for pure ethanol-grown (*Et*-) and pure acetonitrile-grown (*Ac*-) SWNTs, respectively. The mean diameters of the samples were evaluated using the empirical Kataura plot reported in [141], and are 2.1 and 0.8 nm for *Et*-SWNTs and *Ac*-SWNTs, respectively (see diameter evaluation in Section 3.3.3). The mean diameters evaluated from optical absorption are in agreement with that made from TEM images (Figure 3.2) indicate a reduction in mean diameter from 2.1 ± 0.60 nm to 1.0 ± 0.32 nm when the feedstock was changed from pure EtOH to pure AcN.

Figure 3.4a shows resonance Raman spectra of as-grown SWNTs synthesized from both ethanol and acetonitrile. The diameters were evaluated

from the RBM region using the following empirical relation [141],

$$\omega_{\mathrm{RBM}} = \frac{217.8}{d} + 15.7, \tag{3.1}$$

where ω_{RBM} is the Raman shift of the RBM peaks, and d is nanotube diameter in nm. In the empirical Kataura plot [141] the 488 and 514 nm energies excite the first metallic resonance of 0.8 nm *Ac*-SWNTs. The 633 nm excitation wavelength excites the semiconducting resonance in *Ac*-SWNTs. For 2.1 nm *Et*-SWNTs all three excitations lie in the intermingled bands of E_{33}^S and E_{44}^S optical transitions. The strong BWF lineshape in the G-band of *Ac*-SWNTs for 488 and 514 nm excitation is a hallmark of metallic resonance as seen in Figure 3.4b. The position of the G^+-band is 1594 cm^{-1} for all excitations in both samples. RBM peaks confirm selective resonances with diameters between 0.8 and 1.0 nm in *Ac*-SWNTs and between 1.2 and 2.3 nm in *Et*-SWNTs.

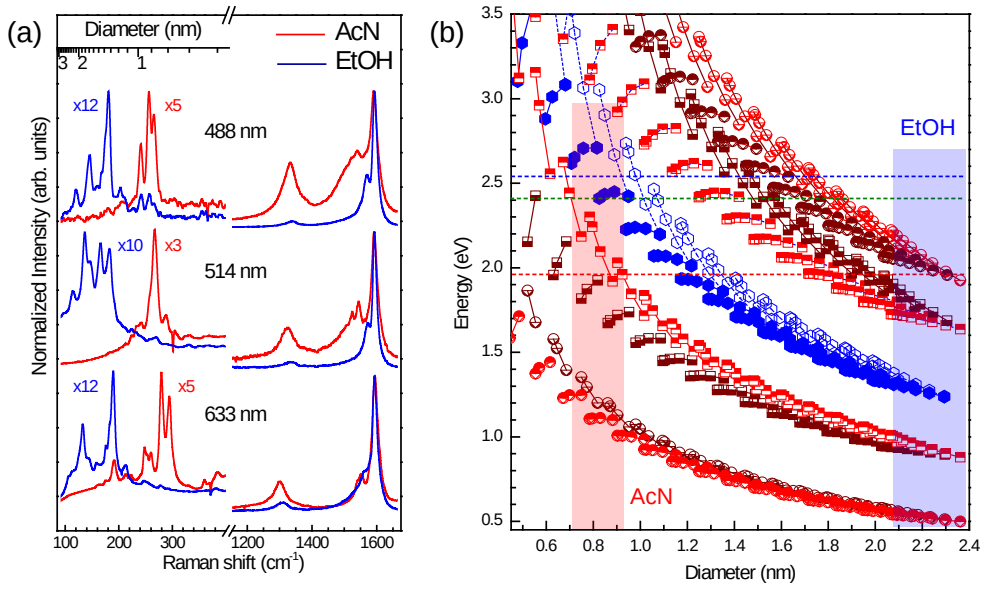

Figure 3.4: (a) Resonance Raman spectra obtained using three different excitation wavelengths from acetonitrile (AcN-) and ethanol (EtOH-) grown SWNTs, and (b) Kataura plot showing an distinguishable electronic behaviors at 488 and 633 nm excitation energies. Reproduced with permission from [137], Copyright © 2012 by John Wiley & Sons.

In the metallic resonance at 488 nm excitation, a large increase in D-band intensity is observed for *Ac*-SWNTs (Figure 3.4a). The G/D ratios at this excitation wavelength in the *Et*- and *Ac*-SWNTs are 19.8 and 3.2, respectively. For 633 nm excitation, the G/D ratios in the pure AcN-grown and pure EtOH-grown SWNTs are 4.3 and 16.7, respectively. The large D-band is primarily due to defects corresponding to lattice distortion of kink structures observed by TEM (Figure 3.2). The higher curvature of small-diameter *Ac*-SWNTs [33] may contribute to the large D-band. The linear dependence of D-band frequency dispersion on excitation laser energy (E_{laser}) has been previously reported [33]. Reference [33] also reports a downshift of the D-band frequency for narrow-diameter SWNTs. We observed an offset of 10 cm^{-1} in D-band frequency in *Ac*-SWNTs for all three E_{laser} measurements (Figure 3.4). We also observe an offset of 41 cm^{-1} in G′-band frequency (Figure 3.10c). This is in agreement with Raman studies on different diameter sizes of inner and outer walls in double-walled CNTs [142].

PLE maps of dispersed *Ac*-SWNTs and *Et*-SWNTs are presented in Figure 3.5. Each peak in the PLE map corresponds to an E_{22}^S absorption and an E_{11}^S emission by one semiconducting chirality. For *Ac*-SWNTs the peak intensities are clustered at shorter excitation and emission wavelengths, whereas in *Et*-SWNTs they are strongest at longer wavelengths. The markings for individual chiralities in Figure 3.5 reveal clear-cut differences in the relative population between dispersed *Ac*-SWNTs and *Et*-SWNTs. The peak positions are found to be indistinguishable. The strongest peaks for *Ac*-SWNTs stem from (6,5), (8,3), (7,5), and (7,6) nanotubes, whereas (8,6),(8,7), (7,6) and (7,5) nanotubes are dominant for *Et*-SWNTs. The diameters accessible by PLE mapping are limited by the narrow semiconducting window and the centrifugation step, which enriches the population of small-diameter SWNTs [143]. The shift in PLE intensities from longer to shorter wavelengths for *Et*-SWNTs and *Ac*-SWNTs is therefore only reminiscent of—but no longer quantitative to—the diameter shift from 2.1 to 0.8 nm in the as-grown *Et*-/*Ac*-SWNTs.

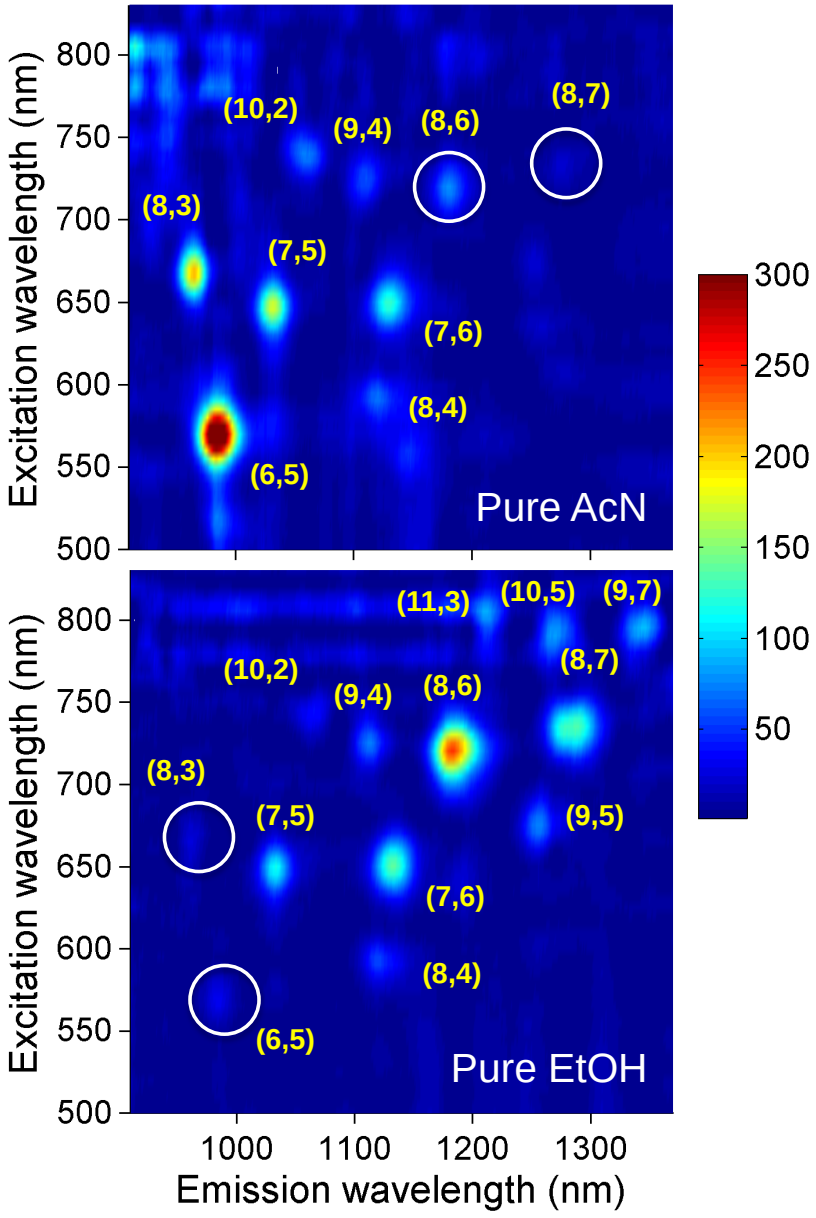

Figure 3.5: Photoluminescence excitation (PLE) maps of acetonitrile (AcN)- and ethanol (EtOH)-grown SWNTs measured from the same dispersed SWNTs as measured in optical absorption (Figure 3.3b). Reproduced with permission from [137], Copyright © 2012 by John Wiley & Sons.

3.3 Diameter tailoring

3.3.1 Influence on flat substrate

The SEM micrographs in Figure 3.6 clearly demonstrate the viability of pure acetonitrile and its mixtures for the synthesis of VA-SWNTs on flat substrates. Thickness of nanotube film (yield) decreases with an increasing of nitrogen feedstock, which may imply an influence of N containing species on the reaction dynamics [118]. Note that there is a bright thin layer observed on the top of 5% AcN-grown SWNT film, which may also be plausibly caused by incompatible reaction of different feedstock decompositions. Optical absorption spectra of as-grown VA-SWNT arrays (Figure 3.7) reveal the change in the E_{11}^S transition into small-diameter SWNTs by adding acetonitrile into ethanol feedstock. The E_{11} position lies in between the E_{11} transition of pure ethanol (0%) and pure acetonitrile (100%). The mean

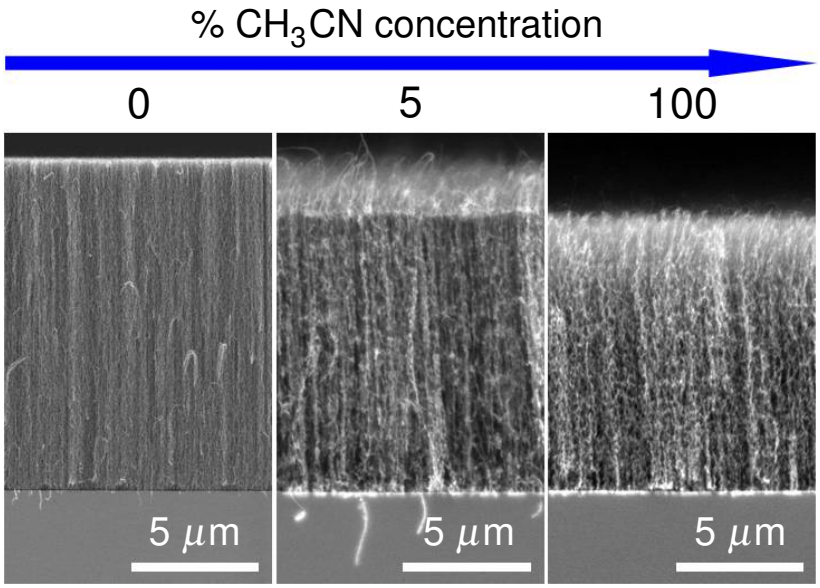

Figure 3.6: SEM micrographs of VA-SWNT arrays synthesized by no-flow CVD using different ethanol/acetonitrile mixed feedstocks (0, 5 and 100 vol.% acetonitrile, CH_3CN). Reproduced with permission from [140], Copyright © 2012, Elsevier.

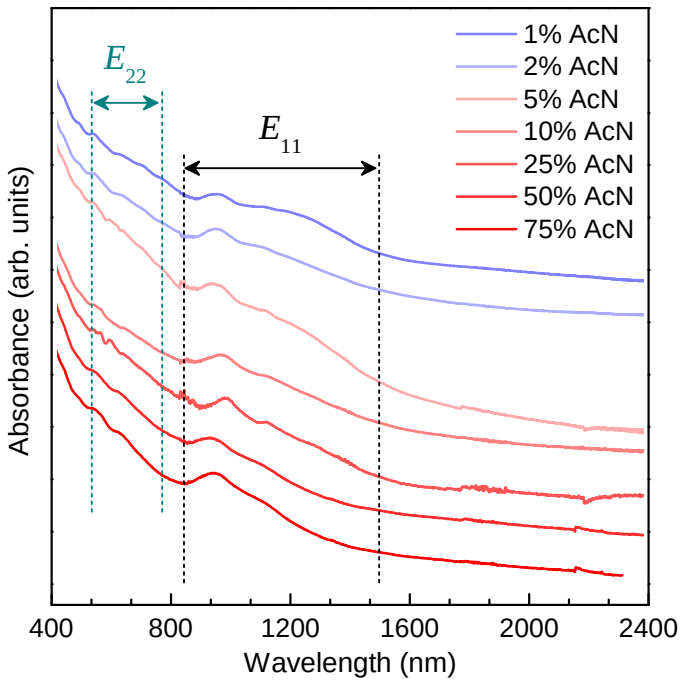

Figure 3.7: Optical absorption spectra of a VA-SWNT arrays synthesized from varied acetonitrile (AcN) concentrions from 1 vol.% to 75 vol.% indicate the first optical transition E_{11} lies in between the E_{11} of pure acetonitrile (100%) and pure ethanol (0%) as shown in Figure 3.3a.

diameters of VA-SWNTs (see Section 3.4) are therefore in between 2.1 and 0.7 nm when acetonitirile was added from 0% to 100%.

Figure 3.8 shows the RBM, D and G lines in resonant Raman spectra measured using 488 and 633 nm laser excitations for different feedstock mixtures. The RBM frequency again scales as the inverse of nanotube diameter according to Equation 3.1 [141]. The D line is only Raman active in the presence of lattice distortions. The splitting of the G line into G^+ and G^- peaks is diameter dependent [30], and the G^- is softened in small-diameter SWNTs [144, 145] as observed with different nanotube diameters (Figure 3.9). In these spectra, the large-diameter RBM peaks at $\sim$190 cm^{-1} are predominant for marginal amounts of acetonitrile in the feedstock. However, this peak begins to diminish and a new RBM peak at $\sim$280 cm^{-1} arises when the concentration of acetonitrile in the feedstock

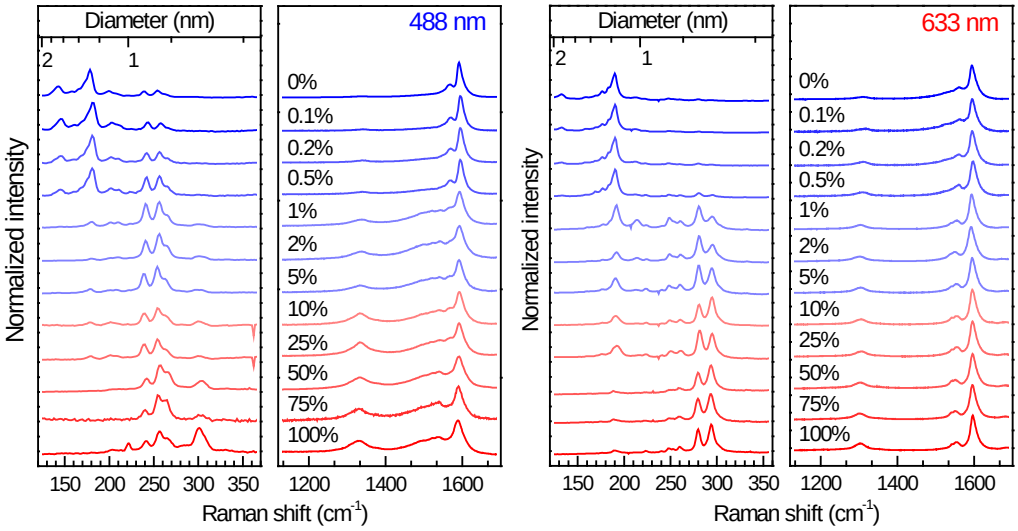

Figure 3.8: Resonance Raman spectra at 488 nm (left) and 633 nm (right) excitations of VA-SWNT arrays grown using different acetonitrile (AcN) concentrations. The tube diameter is evaluated from RBM peak positions using the relation $\omega_{\mathrm{RBM}} = 217.8/d + 15.7$ [141]. Adapted with permission from [140], Copyright © 2012, Elsevier.

reaches 1%. After their sudden appearance, the small diameter RBM peaks at $\sim$280 cm^{-1} grow gradually with increased acetonitrile concentrations in the feedstock.

Here the smaller diameters exhibit a strong Fano resonance and the larger diameters are purely in semiconducting resonance (see Figure 3.10a). It can be clearly seen that the Fano resonance emerges with increasingly small doses of acetonitrile. The position of the G$^+$ line is 1594 cm^{-1} for all samples and for both excitation wavelengths. The RBM peak positions confirm selective resonances with diameters between 0.7 and 1.0 nm when adequate amounts of acetonitrile are added to the feedstock, and diameters between 1.2 and 2.3 nm for pure ethanol (Figure 3.8).

Linear scaling of the D line position with E_{laser} and its diameter dependence have been reported earlier [33]. Figure 3.10b shows a plot of the D line frequencies against E_{laser}. The dispersion of D band is due to electron-phonon coupling when Δk is in resonance with Δq with E_{laser} ($\Delta k = \Delta q$) [146].

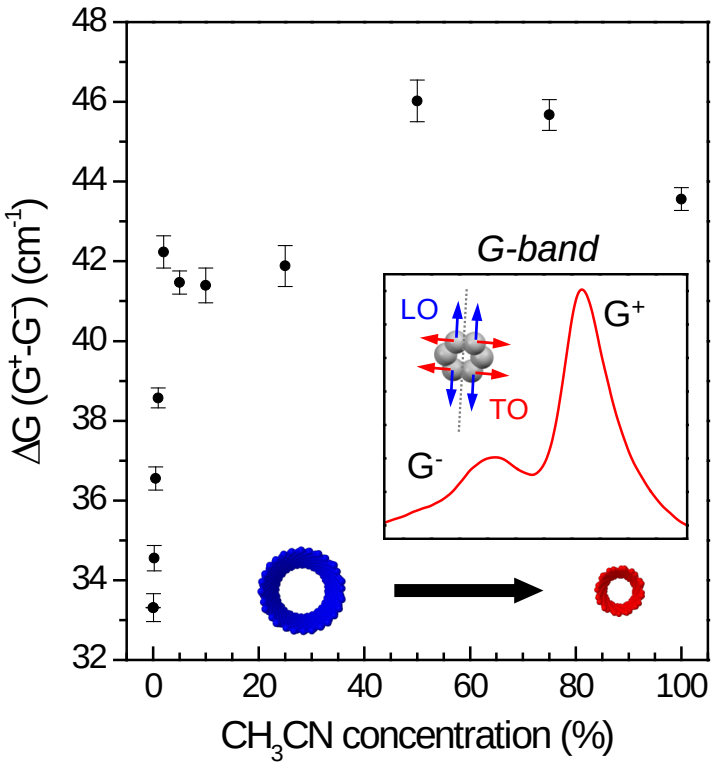

Figure 3.9: High frequency Raman spectra at 488 nm excitation of VA-SWNT arrays grown using different acetonitrile (AcN) concentrations show enhanced splitting of G^+ and G^- due to diameter reduction.

The parallel dispersions for small-diameter pure AcN-grown SWNTs and large-diameter pure EtOH-grown SWNTs are offset by 10 cm^{-1} with parallel slopes of 57 cm^{-1}/eV due to the diameter range differences. The structured G′ lines of both samples were fitted using Lorentzian peaks. The G′ line for the pure EtOH sample was empirically fitted using five peaks at 2615, 2642, 2663, 2680, and 2697 cm^{-1}, whereas four peaks at 2616, 2635, 2661 and 2688 cm^{-1} were used for the pure AcN sample. The offset in the G′ line frequency (peak maximum) at 488 nm (Figure 3.10c) was found to be 41 cm^{-1} (from 2677–2636 cm^{-1}).

These two distinct G′ positions have been observed as distinct components in undoped double-walled carbon nanotubes [142], dispersed HiPco SWNTs [147] and also N-doped SWNTs [148]. Reference [148] interprets

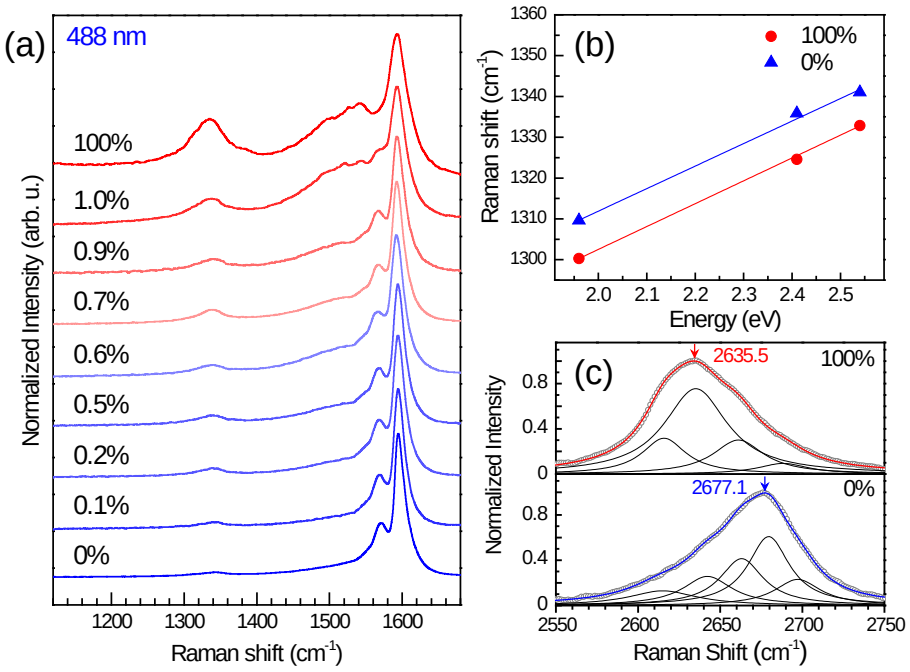

Figure 3.10: (a) For 488 nm Raman excitation, the strong Fano lineshape clearly increases with a marginal increase in the concentration of acetonitrile (AcN) in the feedstock. (b) The D band frequency is found to have an offset of 10 cm^{-1} for different E_{laser}, and (c) a large shift in the G′ line frequency is due to vastly different diameters (red and blue arrows represent G′ line positions for pure AcN (100%) and pure EtOH (0%), respectively). Adapted with permission from [140], Copyright © 2012, Elsevier.

the n-type doping from substitutional N as the origin of the lower frequency G′ peak, whereas in Ref. [147, 149] the two different G′ positions were discussed as resonances of SWNTs with different diameters. As discussed in Section 3.4 and Section 4, we also find a total of 1.2 at.% incorporated N in the pure AcN-grown SWNTs based on XPS measurement. Therefore, in our comparison of pure acetonitrile and ethanol samples intrinsic n-doping via sp^2 N and very different diameters with common resonances should be taken into account. The relation between nanotube diameter and G′ frequency is used according to the Equation 3.2 [149],

$$d \approx \frac{53.2}{70E_{laser} - \omega_{G'} + 2524} \quad \text{nm}. \tag{3.2}$$

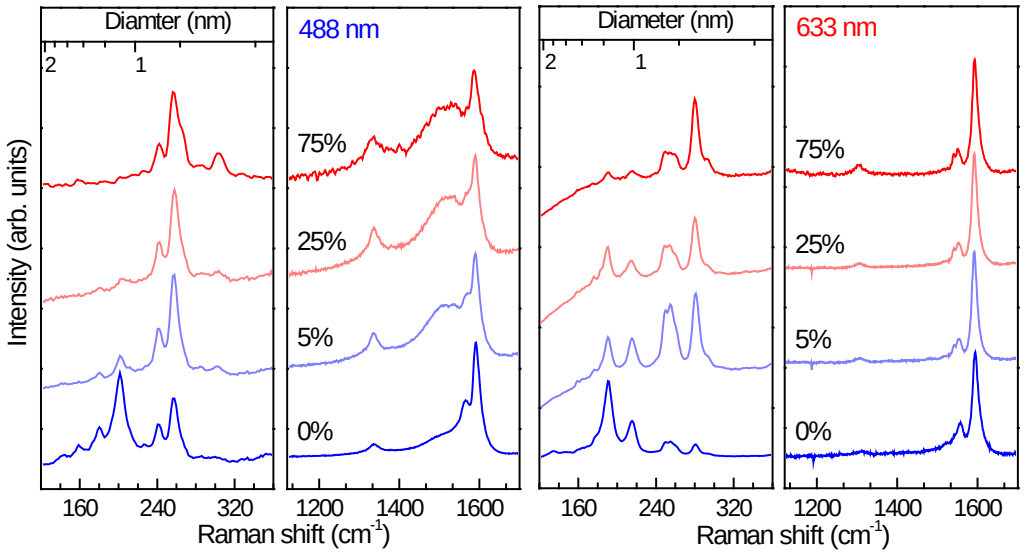

Figure 3.11: Resonance Raman spectra of as-grown SWNTs on zeolite particles from various concentrations of mixed ethanol/acetonitrile (AcN) feedstock. Adapted with permission from [150], Copyright © 2012 by John Wiley & Sons.

The mean diameters evaluated from G′ frequencies of 2635.5 cm^{-1} for pure AcN and 2677.1 cm^{-1} for pure EtOH, are exactly 0.8 and 2.1 nm, respectively which are in agreement with that evaluated from the optical absorbance and TEM observation (Figure 3.3 and Figure 3.2). By comparing to the G′ spectra in Refs. [147–149] we conclude that the major effect is the common resonances from SWNTs with vastly different diameters. An additional influence of localized *n*-type doped N sites may be imposed on the discrete chirality pattern of the structured G′ peaks in pure AcN and pure EtOH samples.

3.3.2 Influence on zeolite

The small-diameter SWNT growth *via* the catalyst support has been well established with alcohol CVD process [52, 54, 123]. With small certain size of its pores, zeolite has been used as catalyst immobilizer at the pore site [52, 54]. By lowering growth temperature [123], small diameter nanotube

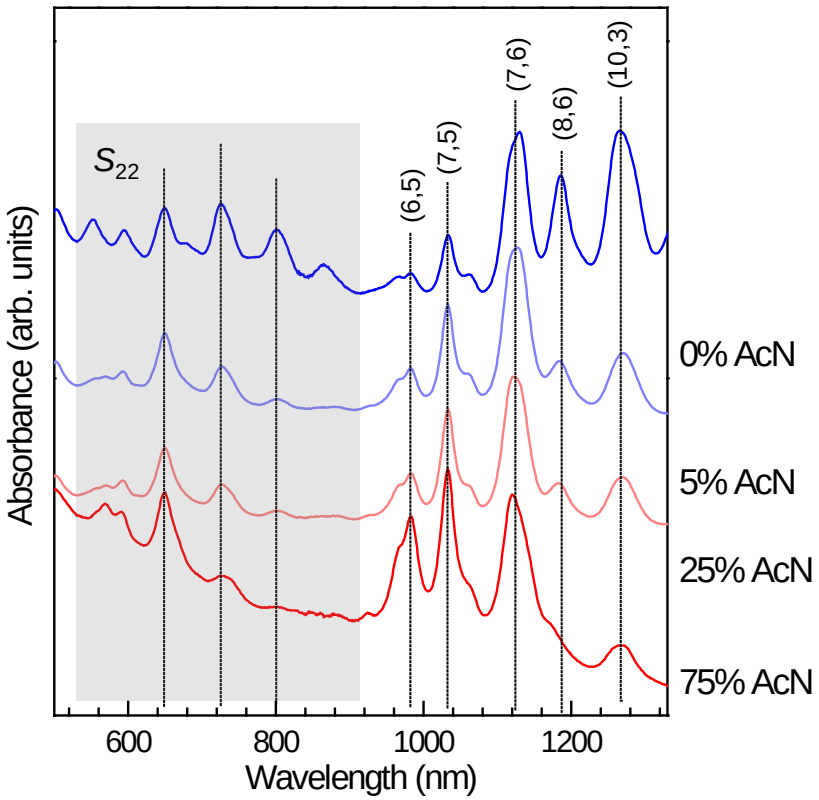

Figure 3.12: Optical absorption spectra of individualized SWNTs suspended by DOC surfactant. SWNTs were synthesized with various concentrations of mixed ethanol/acetonitrile (AcN) feedstock. Adapted with permission from [150], Copyright © 2012 by John Wiley & Sons.

is more pronounced. However, controlling diameter of nanotubes on zeolite at the same preferential growth temperature (*i.e.* 800°C) by other parameters– for instance, pressure, gas flow rate–seems to have less influence on the catalyst agglomeration. Using acetonitrile as a feedstock, reduction in SWNT diameter is thus rather expected.

Figure 3.11 shows the resonance Raman spectra of 488 and 633 nm excitation wavelengths, indicating strong resonance of more narrow SWNTs at higher concentration of acetonitrile mixtures along with predominance in BWF lineshape observed at 488 nm excitation wavelength. The more pronounced BWF lineshape implies a substantial increasing of the more

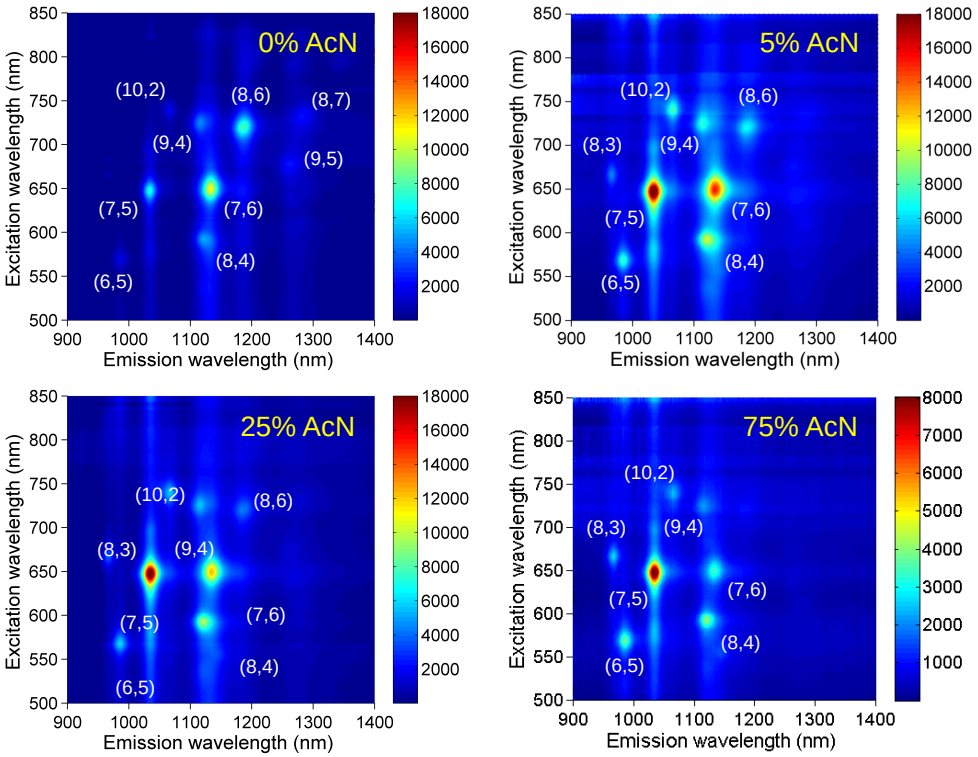

Figure 3.13: PLE maps of individualized SWNTs synthesized from different concentration of mixed feedstocks obtained from the same solution as obtained in Figure 3.12. Reproduced with permission from [140], Copyright © 2012, Elsevier.

narrow metallic SWNTs (see Figure 3.4b). Optical absorption spectra of individualized SWNTs reveal narrow peaks stemming from individual chiralities as shown in Figure 3.12. Figure 3.12 shows a shift towards smaller diameters with increasing concentrations of AcN in the feedstock.

The diameter of SWNTs synthesized from Co/Fe catalysts on zeolite powder [3, 52] using different mixed feedstock recipes was also found to be smaller than for pure ethanol. The PLE maps of SWNT synthesized from pure EtOH and mixed AcN/EtOH feedstocks are depicted in Figure 3.13. A clear redistribution of spectral weight towards shorter emission and excitation wavelength is observed with an increasing acetonitrile concentration. A plot showing PLE peak area for different tube diameters is presented in

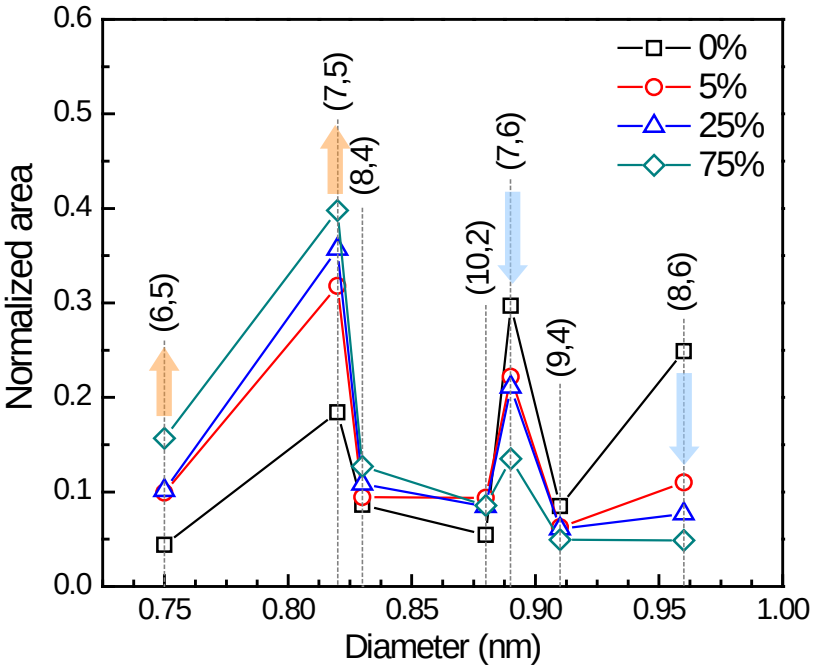

Figure 3.14: Plot of normalized PLE peak areas versus tube diameter for dispersed SWNTs synthesized on zeolite powder using different feedstock mixtures (0 to 75 vol.% acetonitrile, AcN). The orange and blue arrows represent increasing and decreasing abundance with increasing concentration of AcN feedstock. Reproduced with permission from [140], Copyright © 2012, Elsevier.

Figure 3.14. The PLE spectra were obtained from micelle-suspended SWNTs grown on zeolite support (see Figure 3.12), and the normalized peak area was evaluated using the ratio of the area of each peak to the sum of the total peak areas ($A_{(n,m)}/\sum A_{(n,m)}$). Upon increasing the concentration of acetonitrile in the feedstock, the abundance of (6,5) and (7,5) nanotubes appears to increase, whereas the abundance decreases for (7,6) and (8,6) nanotubes. This is in agreement with the absorbance spectra indicating acetonitrile promotes the growth of small-diameter nanotubes.

The small-diameter selective growth from mixed feedstock proves the viability of nitrogen, even a small fraction of acetonitrile was introduced. All optical spectroscopic methods also show a consistent results on this

finding (*i.e.* significant reduction in the mean diameter). The mean SWNT diameter as small as ∼1 nm is produced with pure EtOH due to templated catalyst particles during impregnation process by the nanoporous zeolite morphology, which immobilizes the catalyst during growth process as stated at the beginning of this section. With this pore size, SWNT diameter is in this case restricted by pore size, so that the diameter cannot go larger than 1 nm. However, the upper limit of nanotube diameter is shrunk in the presence of nitrogen during growth process for the same batch of catalytic power. There is in fact declining in yield for high concentrations of AcN as observed in VA-SWNT growth (see Section 3.3.1). The detailed mechanism of incorporated nitrogen to smaller diameters will be discussed in Section 5.

3.3.3 Evaluation of SWNT mean diameter

In general, the SWNT diameter can be optically or physically characterized by TEM or spectroscopic methods. Even though TEM is a straightforward approach to image a clear structure of nanotube, including diffraction patterns of different chiralities, it can at the same time damage the nanotube structure by strong acceleration voltage (knock-on damage) [151], which is often used to image further detail of atomic lattice. On the other hand, spectroscopic methods have been employed to characterize not only the mean diameter and chirality, but also electronic property of SWNT. Therefore, optical absorption spectroscopy provides a distinguishable optical transition and more details on nanotube structure. As stated in Section 1.3.2, mean diameter of SWNTs can be spectroscopically evaluated from the first optical transition E_{11} [152], while resonance Raman spectroscopy requires many excitation energies [141, 153]. In a combined optical transition relation with resonance Raman results [153], the following empirical relation can be obtained,

$$E_{ii}(p, d_t) = \beta_p \cos\frac{3\theta}{d_t^2} + \frac{ap}{d_t}\left[1 + b\frac{\log cd_t}{p}\right], \tag{3.3}$$

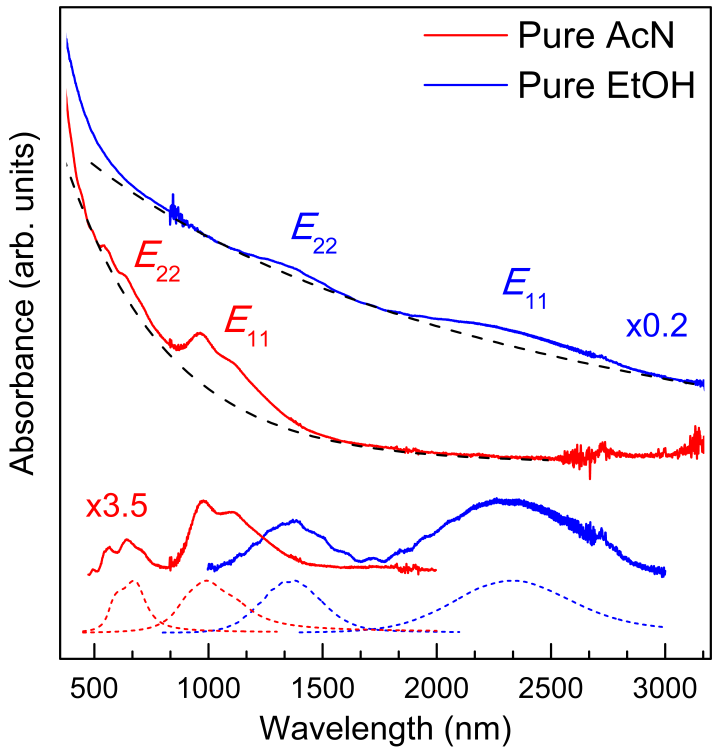

Figure 3.15: UV-Vis-NIR spectra of VA-SWNTs grown from acetonitrile (AcN) and ethanol (EtOH). The black dashed lines represent exponential and hyperbolic background contributions for the case of AcN and EtOH, respectively, and the lower spectra are after background subtraction. Mean diameters were determined from the empirical relation of electronic transition energy (red and blue dashed lines) to be 0.7 and 2.1 nm, respectively (see text). Reproduced with permission from [140], Copyright © 2012, Elsevier.

where β_p is 0.05 and -0.07 for E_{11}^{S} ($p=1$) and E_{22}^{S} ($p=2$), respectively. $a=1.049$ eV·nm, $b=0.456$ and $c=0.812$ nm^{-1}, while tube diameter in nm (d_t) with chiral angle θ (from 0 to 30°) are considered here, which are expressed in term of chirality (n,m) according to the following equations,

$$d_t = \frac{\sqrt{3}a_{c-c}}{\pi}\sqrt{n^2+m^2+nm},$$

$$\theta = \cos^{-1}\left(\frac{2n+m}{2\sqrt{n^2+m^2+nm}}\right).$$

Considering interval of minimum diameter of 0.5 nm and maximum diameter of 3 nm, number of possible chiralities in this diameter range is calculated to be 299 chiralities. The Lorentzian function with Cauchy distribution in Equation 3.4 was used to fit within possible chiralities.

$$f(x;\mu,\Gamma) = \frac{1}{\pi\Gamma\left[1+\left(\frac{x-\mu}{\Gamma}\right)^2\right]} = \frac{1}{\pi}\left[\frac{\Gamma}{(x-\mu)^2+\Gamma^2}\right] \tag{3.4}$$

Figure 3.15 shows an example of the mean diameter evaluation for both *Et*- and *Ac*-SWNTs, which is determined using the empirical relation described in Equation 3.3. In either SWNTs dispersed in aqueous solution or solid bundled, a lifetime broadening Γ of 65 meV was used [154]. However, background contribution of metallic nanotubes in the optical absorption spectra has to be considered. In these cases, the exponential and hyperbolic background contributions are used for acetonitrile and ethanol cases, respectively. The positions and widths of the E_{11}^{S} and E_{22}^{S} peaks are reproduced by diameter distributions centered at 0.7 and 2.1 nm with full-width half-maxima (FWHM) of 0.24 and 0.6 nm for pure acetonitrile-grown and ethanol-grown SWNTs, respectively. The resulting mean diameters are consistent with that observed by TEM (Figure 3.2).

3.4 Nitrogen-doped SWNTs

XPS spectra of VA-SWNTs on flat substrates synthesized from mixed feedstock are shown in Figure 3.16. The survey scans in the inset show a strong C1s peak and a weaker O1s peak. The sp^2 C1s peaks show an asymmetric Doniach-Šunjić lineshape. The well-established [100, 108, 155] binding energy of the C1s at 284.6 eV is used for calibration. The chemical shifts of different bonding environments of incorporated N give rise to one narrow peak at 404.2 eV and a broadened peak at 400.8 eV. The broad peak at 400.8 eV corresponds to sp^2 and pyridinic N configurations, and the narrow peak at 404.2 eV corresponds to molecular nitrogen (N_2) [79, 83, 101, 107, 108]. The atomic concentrations of 0.2 at.% sp^2 and pyridinic N, and 1.0 at.% N_2 molecule for SWNTs grown from pure AcN were determined from the relative XPS peak intensities and the relative atomic cross section of C:N = 1:1.8 [156]. An approximate 1:5 ratio of sp^2 with pyridinic N and N_2 molecule is uncommon for N-doped SWNTs [79, 101, 107, 108], unlike observation in multi-walled carbon nanotubes [114, 115]. The detail of N_2 finding will be discussed in Section 4.

As revealed by the optical spectra discussed in Section 3.3.1 and 3.3.2, a marginal addition of AcN (0.1%) causes the tube diameter to be dramatically reduced from 2.1 to 1.1 nm, whereas higher AcN concentrations further reduce the mean diameter to 0.7 nm. XPS spectra indicate the N content is only gradually reduced when reducing the AcN concentration from 5% to 1%, but a steep change in N content is observed between 0.5% and 1% AcN. Since the N content at 5% and 1% is clearly beyond what a simple scaling by 5% or 1% would predict, we propose total N in carbon nanotubes saturates slightly above 1 at.%. Very remarkably, the saturated incorporation correlates with the reduction of the mean diameter (Figure 3.17). The vividly displayed correlation in Figure 3.17 points at the incorporation of N as the cause of diameter reduction. The saturated maximum N_2 content of 1 at.% presented inside nanotubes is, however, found to be much lower than fully packed N_2 case inside considered (6,6) SWNT ($\sim$ 3.7 at.%), which can be explained by

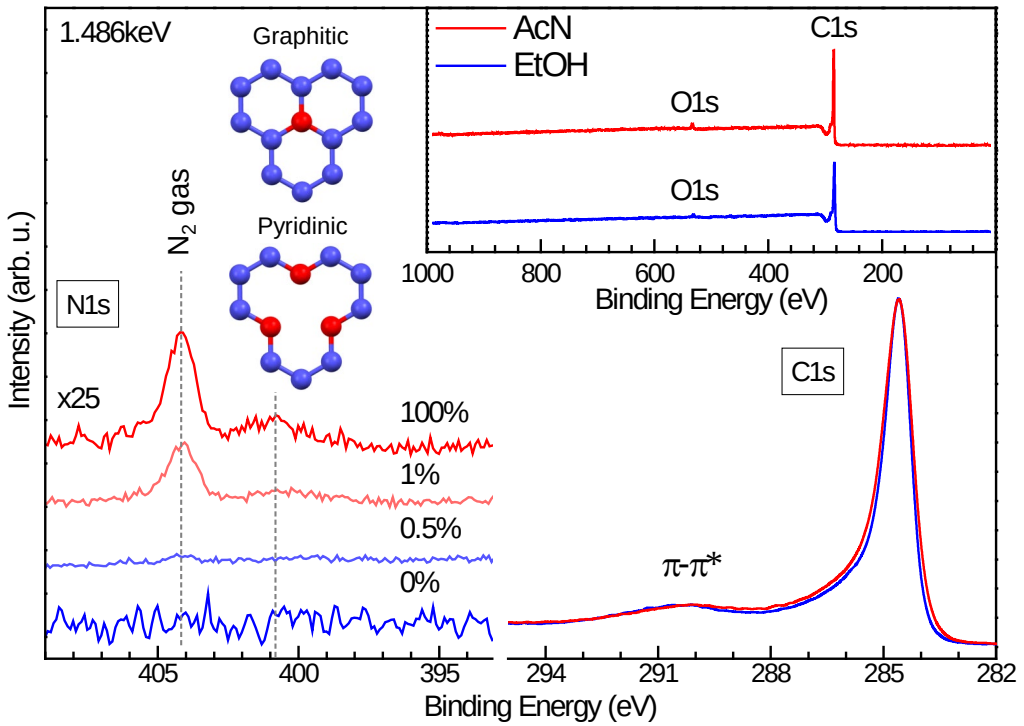

Figure 3.16: The main panel shows C1s and N1s core level XPS spectra of VA-SWNTs synthesized from different feedstocks. For synthesis from pure acetonitrile (100%, AcN), the N1s profile is composed of ∼0.2 at.% for sp^2 and pyridinic N, and ∼1 at.% for N_2 (blue and red balls represent C and N atoms, respectively). Corresponding survey scans are provided in the inset. Adapted with permission from [140], Copyright © 2012, Elsevier.

thermodynamically unfavorable at high temperature (*i.e.* 800°C).

As observed by TEM (Figure 3.2), some of SWNTs are defective and kink, which may not be able to contribute luminescence process of PLE measurement, and the major contribution may be from less defective nanotubes (*i.e.* no N incorporation). To investigate whether or not separated SWNTs (small diameter) can contribute in photoluminescence process, the XPS measurement was performed on filtrated nanotube film after separation. The XPS survey presented in Figure 3.18a shows the characteristic peaks of carbon, oxygen, as well as sodium. The latter is related to the reference DOC surfactant that was used to disperse SWNTs. As shown in Figure 3.18b, the

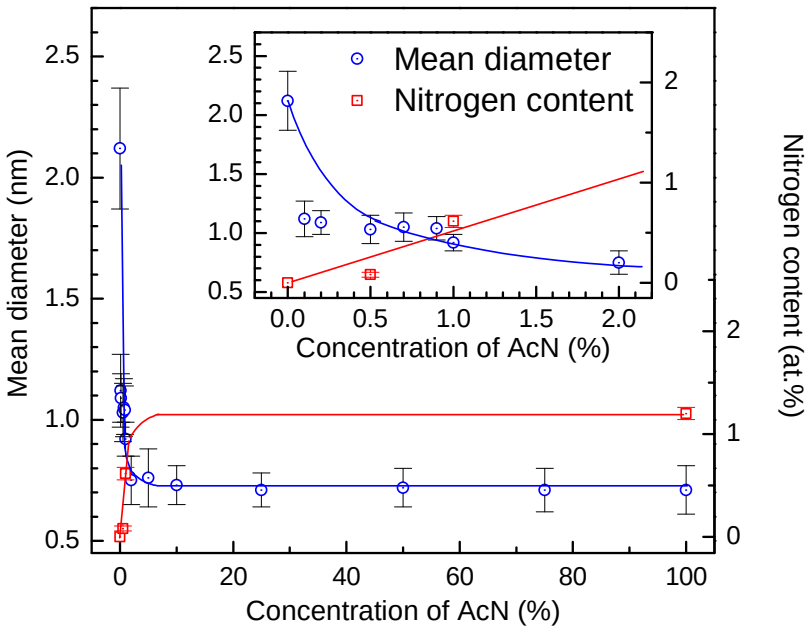

Figure 3.17: A plot showing mean diameters of VA-SWNTs based on UV-Vis-NIR and XPS spectra of SWNTs synthesized using feedstock mixtures containing different concentration of acetonitrile in ethanol. A dramatic decrease in diameter is seen at low N content, followed by a saturation behavior for higher CH_3CN concentrations. Reproduced with permission from [140], Copyright © 2012, Elsevier.

C1s lineshape and binding energies in sp^2 carbon network of SWNTs and molecular DOC surfactant are inherently different and well distinguishable. Hence, the archetypical C1s lineshape of SWNTs is not strongly influenced by the presence of DOC molecules. By comparing N-doped, EtOH-grown SWNTs, and DOC reference, the N1s peak is observed only if the feedstock contained AcN. The appearance of the N1s signal reveals characteristic chemical shifts of incorporated nitrogen into nanotubes (∼400 eV) and N_2 molecule (∼404 eV). In the present concentration of 5% AcN in the feedstock, there is a total of ∼1 at.% of substitutional sp^2 N, pyridinic N, and N_2 molecule. A concentration of 5% AcN is sufficient to reach the maximum attainable nitrogen doping [140].

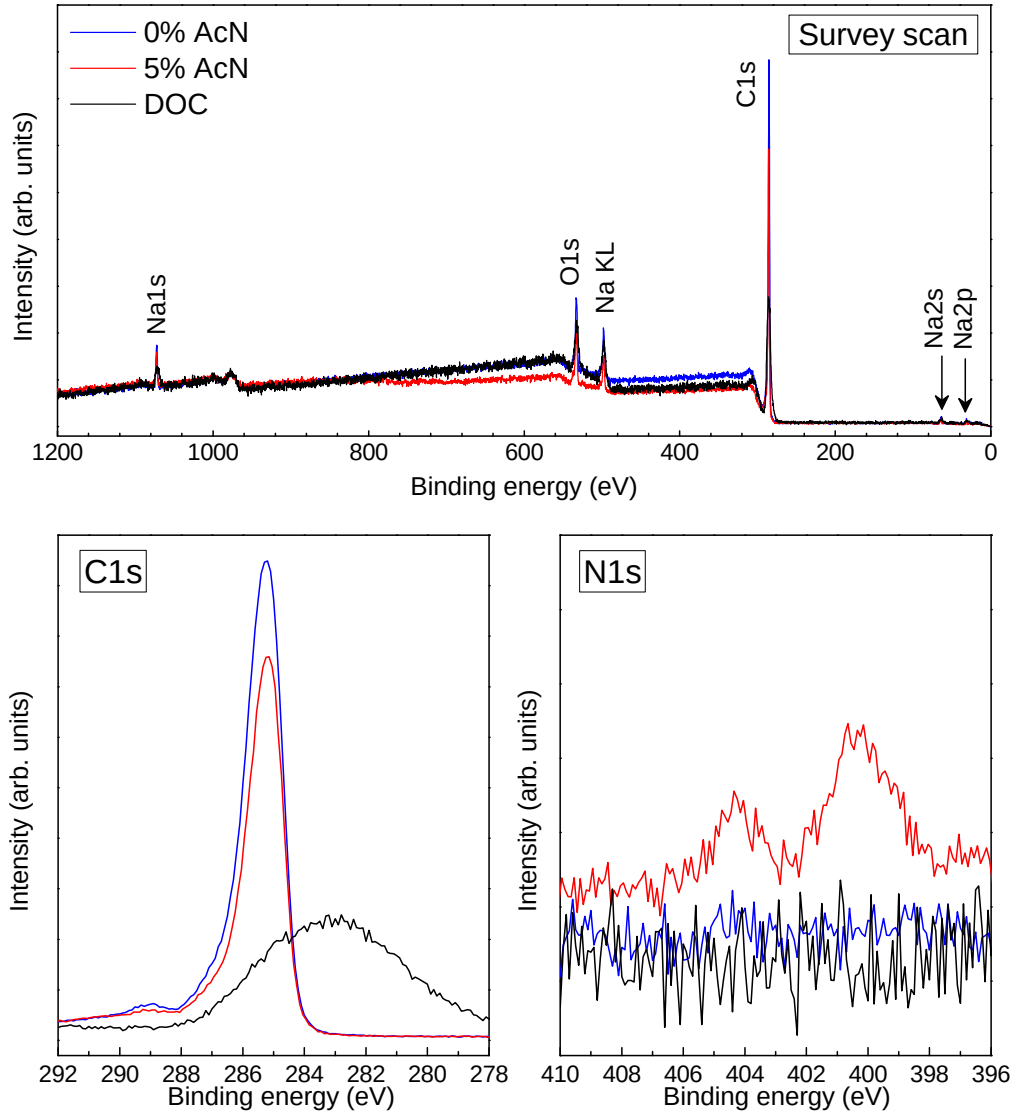

Figure 3.18: (a) XPS survey scan of SWNTs grown from pure ethanol (0%) and 5% acetonitrile (AcN) with (b) C1s and (c) N1 scans. The DOC surfactant is used as reference spectra. Adapted with permission from [150], Copyright © 2012 by John Wiley & Sons.

Chapter 4

One-Dimensional Nitrogen molecule

4.1 Introduction

Such nanoscale 1D space inside SWNTs has been attracting many studies relative to the interaction of carbon atoms and encapsulated elements. The nanospace inside SWNTs have been initially realized for high efficiency of hydrogen storage [157–159]. The confined nanospace has been later on used to the variety of metals oxides by opening nanotube caps after synthesis and re-filling desired metals [160], including 0D carbon allotrope as fullerenes (peapods) [161, 162] and nanowires [163]. However, gas molecules can be encapsulated during synthesis, which does not require any cap opening afterward. One of the possible ways is using feedstock that contains the desired elements, which is basically similar to doping process. Making use of nitrogen as dopant has been previously studied [76], while encapsulated nitrogen molecules (N_2) has been found as by-product from decomposition of carbon feedstock [113]. The somewhat encapsulated N_2 molecules are linearly restricted in certain direction by host nanotube-induced interaction inside the confined nanospace of multi-walled carbon nanotubes (MWNTs) or hollow carbon nitride nanofibers [114–116]. Still, sufficient alignment of

1D N_2 molecules is remained unclear.

In this Section, encapsulated N_2 molecules and their alignment are studied on nitrogen doping of small-diameter SWNTs during synthesis process (see Section 3) by employing high resolution NEXAFS along with molecular dynamics simulations (MD). The origin of N_2 is studied by isotope $^{15}N_2$ labeling. The fingerprint of co-axially aligned N_2 molecules observed from NEXAFS is observed with polarization dependence that is in agreement with the MD simulation results in which the movement of N_2 is clearly minimized as diameter of host VA-SWNTs reduces.

4.2 Encapsulated nitrogen gas

Nitrogen-doped VA-SWNTs grown on Co/Mo binary catalysts were synthesized using no-flow CVD [54, 58, 164] (see Section 3). The concentration of 5% acetonitrile (5% AcN) mixture into ethanol (EtOH) was used as a feedstock [140], while pure EtOH was used as a reference. The SEM image of a 5% AcN-grown SWNTs is depicted in Figure 4.1(left panel, inset), revealing growth in vertical fashion of 6 μm high SWNT array. The XPS spectrum of the 5% AcN sample shows a narrow asymmetric Doniach-Šunjić profile in the C1s core level of the sample as shown in Figure 4.1 (left panel). The N1s core level of 5% AcN-grown SWNTs consists of chemical shifts of pyridinic and graphitic nitrogen configurations near 399–400 eV and molecular N_2 near 404 eV (Figure 4.1, right panel), whereas the N1s peaks do not appear in the XPS spectra of EtOH-grown SWNTs (see Figure 3.16 in Section 3).

Figure 4.2 reveals viability of N_2 molecules in N-doped SWNTs. Vanishing of N_2 after opening cap and annealing is determined by the area of peak at $\sim$ 404 eV as shown in Figure 4.2. One can think of N_2 deflating from interior of nanotubes, which indicates the corresponding N_2 peak at $\sim$ 404 eV, unlike strong hindering observed on trapped N_2 inside complicated structured crystal material [165]. Its content of $\sim$ 0.03 at.% is found to be insignificant diminished as compared with pristine sample (0.3 at.%). Note that the

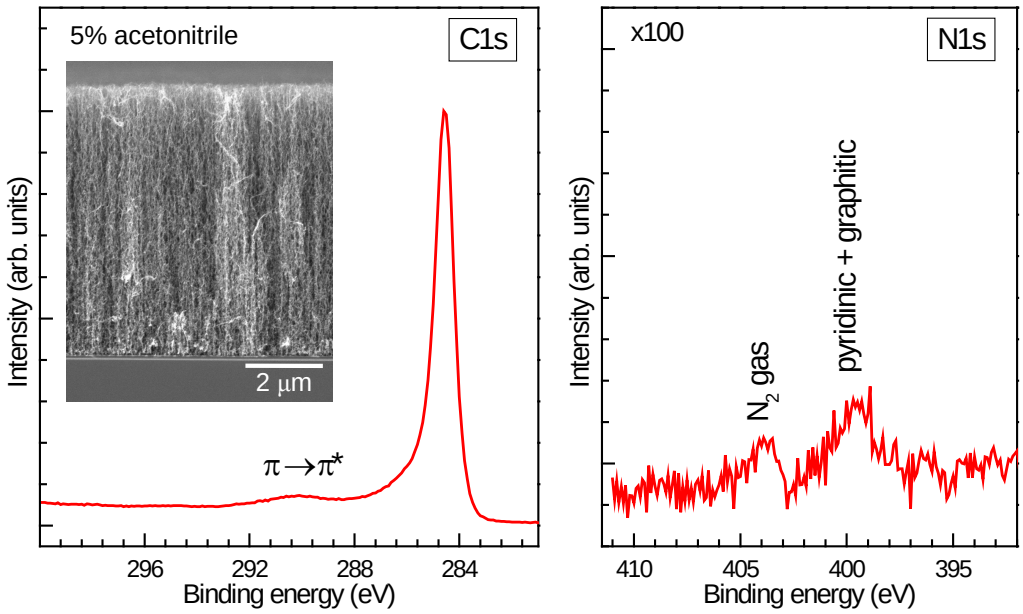

Figure 4.1: XPS spectra of the C1s (left panel) and the N1s (right) core levels of VA-SWNTs synthesized from 5% acetonitrile (5% AcN) (inset). Adapted with permission from [117], Copyright © 2013 by Elsevier.

observed binding energy of encapsulated N_2 molecules is significantly lower than that of free molecular N_2 gaseous (409.9 eV) [166]. This can be explained by electron screening for N1s core-holes due to weak interaction between N_2 molecules and the matrix, which has also been similarly observed from physisorption process of N_2 molecules on metal surfaces [167, 168]. The similar scenario has also been found in MWNTs [96, 169]. The effect from interaction of nanotube wall and interstitial N_2 molecules would reduce the energy gap between lowest unoccupied molecular orbital (LUMO) and highest occupied molecular orbital (HOMO) of N_2 as molecule density increases [170]. A decrease in binding energy of N_2 is, therefore, dependent of density of encapsulated N_2, as well as, how molecules are packed in the interior of nanotubes, which tends to have diameter dependent. However, the further study on diameter-dependent binding energy of encapsulated N_2 need to deserved. The observed shift in C1s was found to be approximately 0.1 eV without broadening (Figure 4.2), which is plausibly caused disappearance of

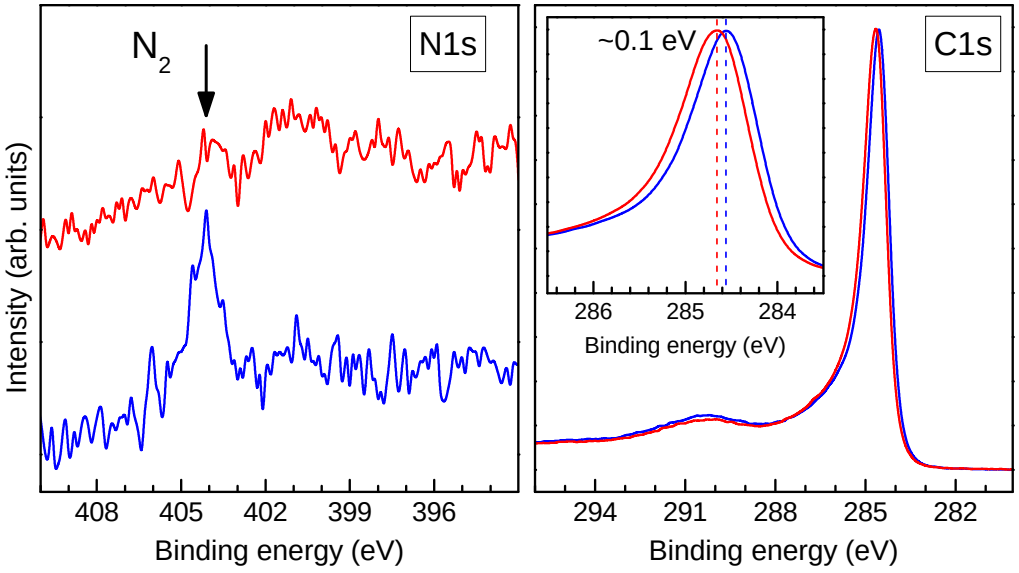

Figure 4.2: Photoemission spectra of the N1s and C1s of 10% AcN-grown SWNTs before (blue line) and after (red line) cap opening and annealing.

core-holes screening, resulting in binding energy raised up by 0.1 eV.

Following disappearance of N_2, one can expect dwindling in electron-phonon coupling interaction from additional harmonic coupling between filling atom (*i.e.* N) and carbon atom, resulting in change in G-band linewidth (Figure 4.3) [171]. Figure 4.3 shows comparison of G-band linewidth before and after annealing. The G-bands were fitted using one fixed Fano lineshape at 1571 cm^{-1}, one fixed Lorentzian peak at 1607 cm^{-1}, and one free Lorentzian peak for EtOH case, and one fixed Fano lineshape at 1521 cm^{-1}, five fixed Lorentzian peaks at 1486, 1552, 1568, 1607 cm^{-1}, and one free Lorentzian peak for 10% AcN case. Considering G-band linewidth of 10% AcN-grown SWNTs, while G-band frequency is maintained, its linewidth is narrower by $\sim 1.1\,cm^{-1}$. This narrowing indicates disappearance of harmonic coupling of N_2 molecules and carbon atoms in nanotubes. Note that there is no neither significant change in G-band linewidth for EtOH-grown SWNTs, nor annealing and impurity effect. Another reason for narrower in G-band linewidth can be plausibly from lose in interaction of N_2 molecules

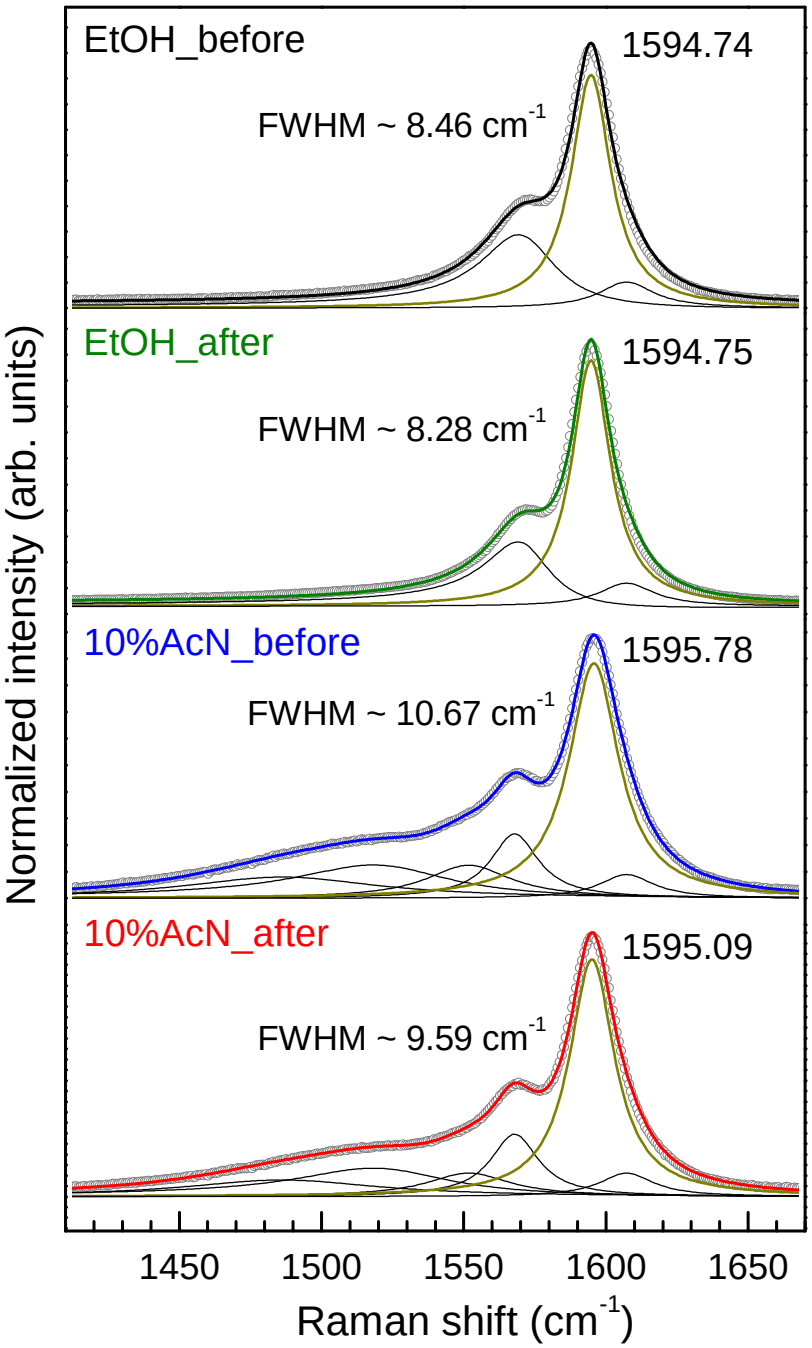

Figure 4.3: High frequency G-band spectra of SWNTs before and after cap opening and annealing. Reducing in G-band linewidth is due to absence of coulomb interaction from encapsulated N_2 molecules [171].

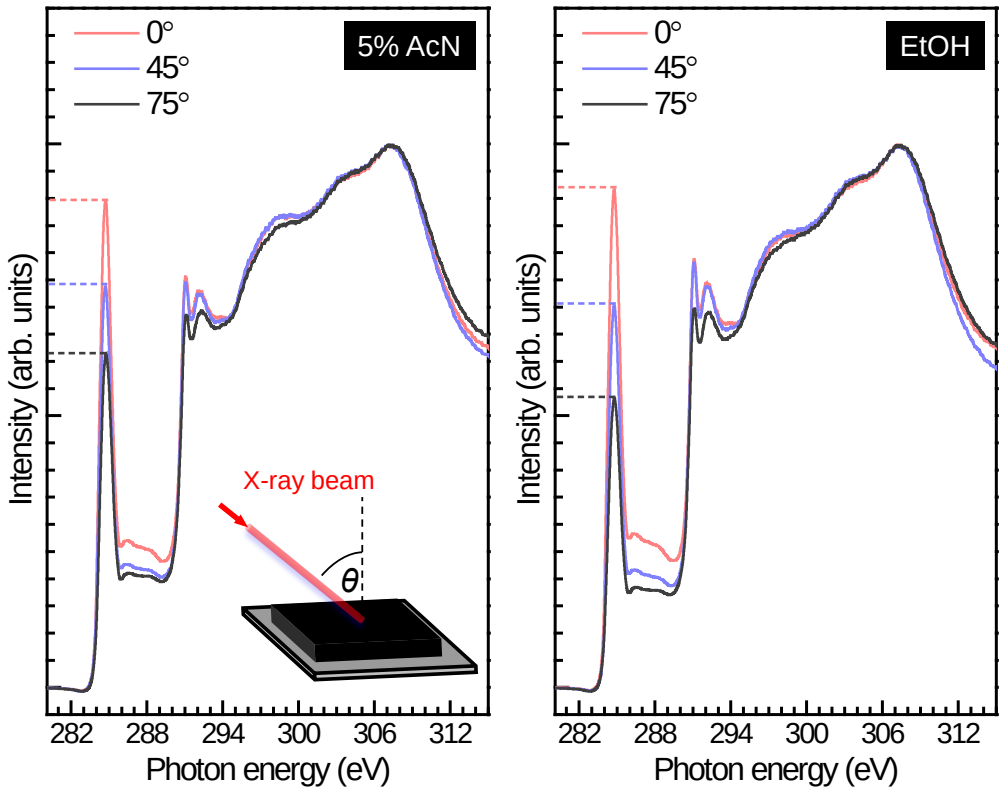

Figure 4.4: Near-edge x-ray absorption fine structure spectroscopy (NEXAFS) of carbon edge (C1s) with different incident angles between the SWNT axis and the linearly polarized incident X-ray beam. Spectra are scaled to the maximum in the $\sigma^\star$ resonance. Adapted with permission from [117], Copyright © 2013 by Elsevier.

in which no effect of coulomb interaction due to N_2 on π-electrons of carbon atoms, resulting in longer phonon lifetime and narrower in G-band linewidth.

X-ray absorption spectroscopy (XAS) measurement was conducted at BL27SU at the SPring-8 synchrotron facility. The beamline is dedicated to soft X-ray absorption spectroscopy. The samples were mounded with molybdenum stage. The XAS spectra were recorded in bulk sensitive drain current mode (∼100 nm). The alignment of SWNTs is detected by changing the incident angle between the linearly polarized X-ray beam and normal direction to SWNT array (nanotube axis). In order to remove any atmospheric adsorbates, both samples were annealed in ultra high vacuum

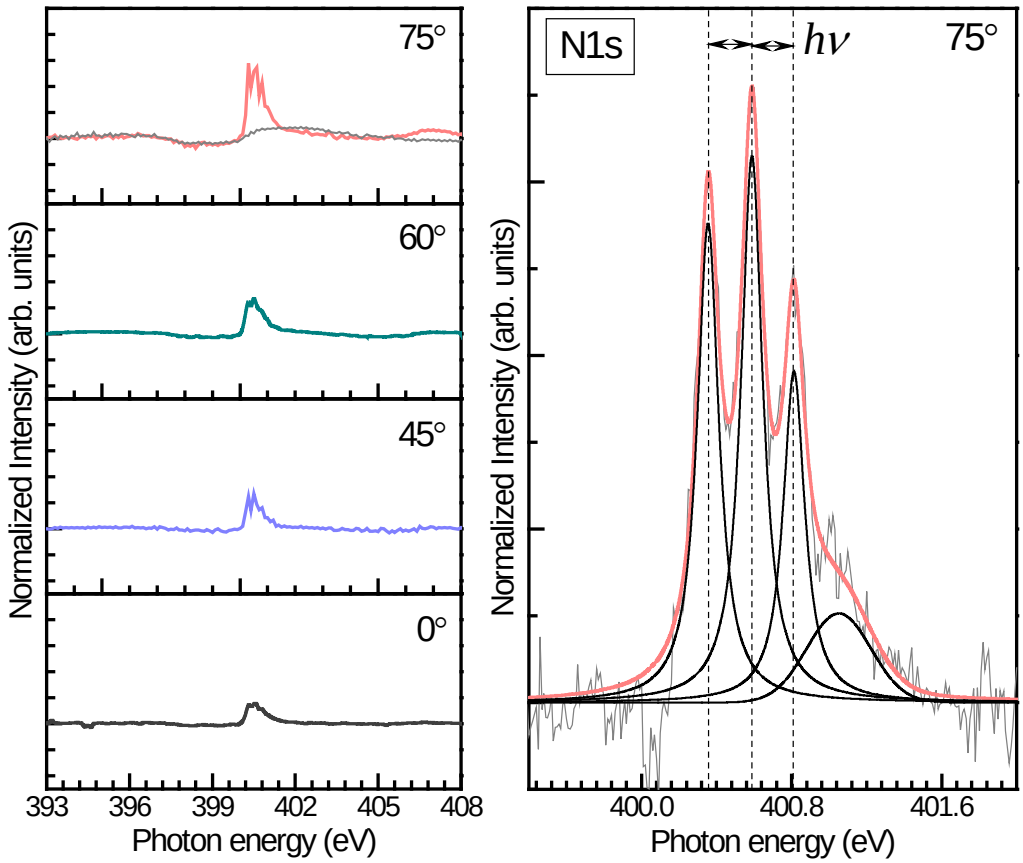

Figure 4.5: Near-edge x-ray absorption fine structure spectroscopy (NEXAFS) of nitrogen edge (N1s) in VA-SWNT synthesized from 5% acetonitrile/ethanol mixed feedstock with different incident angles between the SWNT axis and the linearly polarized incident X-ray beam, whereas there is no appearance of that in pure ethanol sample (dotted line in the topmost panel, 75°). A high resolution scan of the vibrational fine structure of N1s $\rightarrow \pi^\star$ resonance is shown in the right panel. Adapted with permission from [117], Copyright © 2013 by Elsevier.

(UHV, 5×10^{-9} mbar) at 400°C prior to measurement [172]. Figure 4.4 show the C1s absorption edges of annealed EtOH and 5 %AcN samples, revealing the archetypical spectral shape of high-quality SWNT [173] that indicate the C1s $\rightarrow \pi^\star$ resonance at 284.6 eV and the transitions into $\sigma^\star$ states above 290 eV. Lineshapes of these C1s edge of XAS spectra are in fact indistinguishable.

Figure 4.5 show the N1s absorption edge spectra of 5% AcN sample scanned in entire possible N1s π chemical shifts region, indicating the viability of nitrogen in the sample. The N1s $\rightarrow \pi^\star$ (397 eV) and N1s $\rightarrow \sigma^\star$ (407 eV) are hardly noticeable, while the clear sharp peak of unexpected N1s absorption edge of molecular nitrogen (N_2) at 400.3 eV is observed [114] indicating the predominance of N_2 molecules. The detail of expected N_2 from acetonitrile will be discussed in Section 4.3.

The incomparable amount of incorporated nitrogen and N_2 molecules is due to a bulk sensitivity of XAS measurement and extremely surface sensitivity of XPS measurement (Figure 4.1). Interestingly, as observed in polarization-dependence of the C1s $\rightarrow \sigma^\star$, the more intensity of the N1s $\rightarrow \sigma^\star$ absorption edge is clearly seen in which angle of the electric field vector respective to the nanotube alignment direction is increased. Figure 4.5 (right panel) shows a high resolution scan of the N1s $\rightarrow \pi^\star$ resonance above 400.3 eV. This N1s peak is fitted by Voigtian components with the full width at half maxima (FWHM) of 138±3 meV, and a peak spacing of 233±3 meV. This N1s fine structures in fact correspond to the vibrational sidebands of the N_2 molecule, which match the values for free N_2 molecules [174]. Prior to XAS measurement, the SWNT samples were annealed in UHV condition, so that gas molecule adsorbates were removed. The resulting XAS spectra from N1s absorption edge from inside nanotubes will be well expected. The alignment of N_2 molecules will be discussed in Section 4.4.

4.3 Isotope ^{15}N-labeled encapsulated N_2

In general, SWNTs are in CVD process synthesized at low pressure (1–3 kPa) [Ref], and background pressure of CVD chamber is not in UHV. Some other gas molecules from atmosphere still remain during synthesis process, even though there are harmless to nanotubes. Then, an appearance of N_2 inside nanotubes need to be investigated. A 1.5% mixture of isotope $CH_3C^{15}N$ into EtOH was used to synthesize nanotubes. Isotope $CH_3C^{15}N$

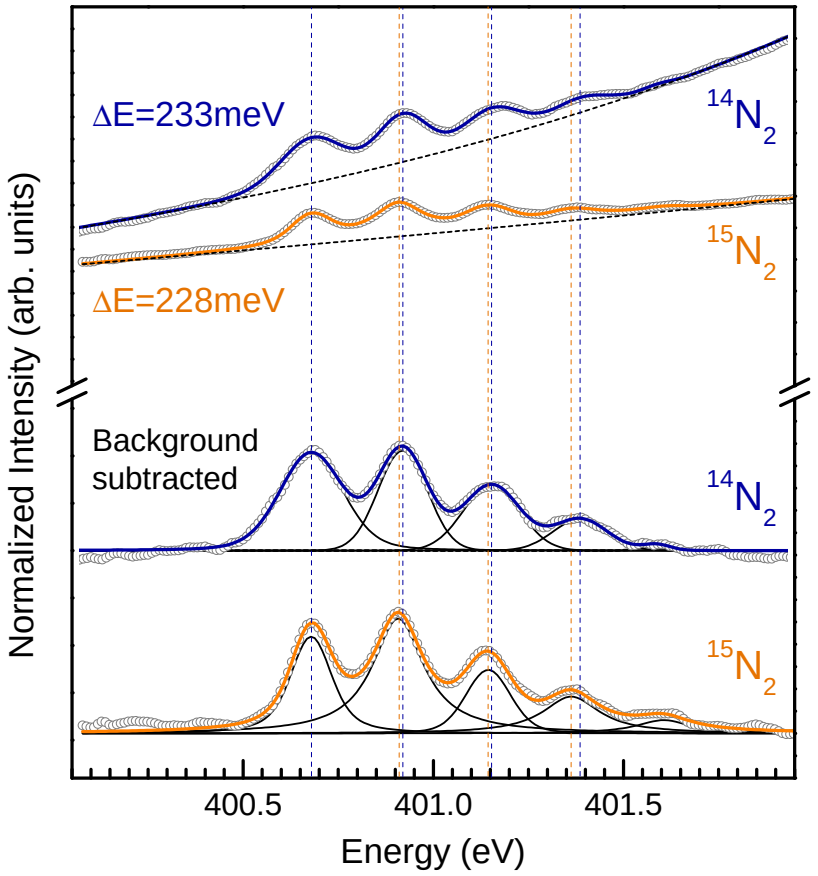

Figure 4.6: High resolution XAS of the vibron satellites in the N1s resonance of $^{14}N_2$ (dark blue) and $^{15}N_2$ (orange) VA-SWNT. Raw data are circles, solid lines are fits and dashed lines are individual peaks or the background, respectively.

was purchased from Cambridge Isotope Laboratories Inc. with impurity of $\geq 98\%$. SWNTs synthesized from $CH_3C^{15}N$ was compared with that from $CH_3C^{14}N$ by NEXAFS measurement in which the possible isotope shift in the vibration energies can be investigated.

Figure 4.6 shows normalized NEXAFS spectra of N1s absorption fine structure before and after background subtraction. Each vibration modes of N_2 can be clearly distinguishable and well resolved. The lowest resonance vibration energy corresponds to the unscattered N1s absorption, and higher resonance vibration energies correspond to excitation of higher vibration

modes. After subtracting with linear background, five Voigtian peaks were used to fit the spectra. The fitted peaks are well resolved, and an isotope shift is discernible as shown by vertical dashed lines in Figure 4.6. At a FWHM of 140 meV with a typical uncertainty of ±2 meV, very smooth spectra from a ∼ 600 ppm fraction in the specimen are required to reveal the subtle isotope shift. An average vibration energy of $^{15}N_2$ is found to be 228 ± 2 meV as expected for an equidistant satellites spaced 225 meV for pure $^{15}N_2$ according to the following relation [175],

$$\omega_{15N} = \omega_{14N} \times \sqrt{\frac{m_{14N}}{m_{15N}}},$$

where ω_{15N}, ω_{14N} and m_{15N}, m_{14N} are vibration energies and mass of ^{15}N and ^{14}N, respectively. Note that an equidistant satellites of $^{14}N_2$ is spaced at 233 ± 2 meV [21]. The expected isotope shift is found to be ∼ 24 meV for the forth peak, which is 2 to 3 data points at ∼ 10 meV step size.

The obtained N1s NEXAFS spectra of $^{14}N_2$ and $^{15}N_2$ are in agreement with the expected isotope shift. This suggests that N_2 molecules access to the nanotubes during synthesis process. By dissociating C-N bond from acetonitrile, N_2 is formed and leaves that catalyst nanoparticle surface, while having possibility to enter the growing nanotubes, which has been proposed by Yang *et al.* [176] for N_2-filled carbon nanofibers.

Unequal contributions of two carbon from EtOH (CH_3CH_2OH) molecule to nanotube formation [177] has been previously demonstrated by tracing of isotope ^{13}C in CH_3CH_2OH molecules into nanotube formation, which appear in change in Raman shift of G-band frequency due to the presence of different carbon mass [175]. Similarly, isotope $CH_3{}^{13}CN$ was used as isotope labeling in order to investigate nitrogen activity from decomposition of acetonitrile (CH_3CN) in which two carbon atoms may have different contributions.

Figure 4.7 shows high frequency resonance of G-band region of SWNTs synthesized from pure isotope $CH_3{}^{13}CN$, indicating a large downshift in G-band frequency and its broadening due to incorporation of ^{13}C into sp^2 carbon

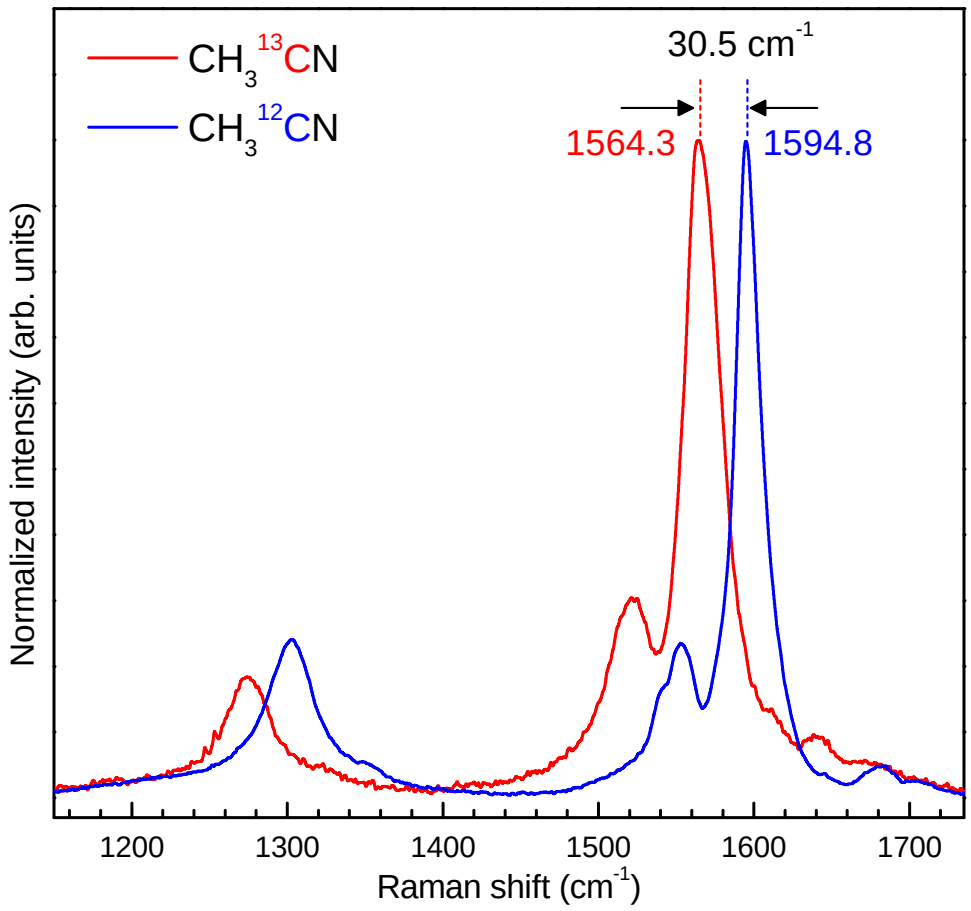

Figure 4.7: G-band in high frequency Raman spectra of SWNTs synthesized from pure isotope $CH_3{}^{13}CN$ excited at 663 nm.

network [178–180]. The G-band shift $\Delta\omega$ originates from an increasing mass of carbon atom into the nanotube walls, which can be correlated with mass fraction of incorporated ^{13}C (c) according to the relation,

$$\left(\frac{\omega_G}{\omega_{G_0}}\right)^2 = \frac{m_{12\mathrm{C}} + 0.011}{m_{12\mathrm{C}} + m_{13\mathrm{C}}}, \tag{4.1}$$

where ω_{G_0} is G-band frequency of original ^{12}C material, $m_{12\mathrm{C}}$ is mass of ^{12}C, and 0.011 is the presence of natural ^{13}C in carbon. This gives amount of $m_{13\mathrm{C}} = 0.48$ ^{13}C enrichment, corresponding to 48% ^{13}C incorporated into nanotube walls. Meaning that probabilities of ^{13}C and ^{12}C interacting at

the catalyst surface and forming nanotubes are equally comparable.

Considering thermal decomposition of acetonitrile at high temperature studied in Refs. [132, 181] along with bonding energy of carbon species, C≡N bond seems to be stable at high temperature. In addition, binding energy of C≡N bond (891 kJ/mol) is higher than that of other bonding configurations from decomposed species of CH_3CN, and more energy is vital to break C≡N bond apart. The contribution of ^{13}C, therefore, represents probability of nitrogen incorporation on nanotube formation in which nitrogen always come together with its adjacent carbon.

4.4 Aligned N_2 molecule inside VA-SWNTs

The orientation factor of VA-SWNT arrays is expressed by the nematic order parameter ξ by fitting the intensity differences of the π resonances in different polarization angles using an offset cosine squared model function $I_\pi(\phi) = A + B \cdot \cos^2(\phi)$ as shown Figure 4.8. ξ values of VA-SWNT arrays is evaluated from normalized intensity of C1s $\rightarrow \pi^\star$ absorption edge (Figure 4.4) according to the relation from Equation 4.2 [182], resulting in negative ξ values.

$$\xi = \frac{I_\parallel - I_\perp}{I_\parallel + 2 \cdot I_\perp} \tag{4.2}$$

where $I_\parallel$ and $I_\perp$ are absorption intensities when the electric field vector parallel and perpendicular to the nanotube alignment. ξ values of the aligned nanotube array are the doubled positive of the negative ξ of the C1s $\rightarrow \pi^\star$ transitions, which result in +0.25 for 5% AcN sample and +0.35 for EtOH sample. In comparison to the actual bulk absorption [182], the lower in ξ values is in agreement of the relatively shallow probed depth of XAS technique (∼100 nm), which gives a close order parameter values to that resulted from resonance Raman scattering [183, 184] (see Appendix). This may imply the observation limit of characterization technique in which a tiny area of the sample is exposed to the laser spot.

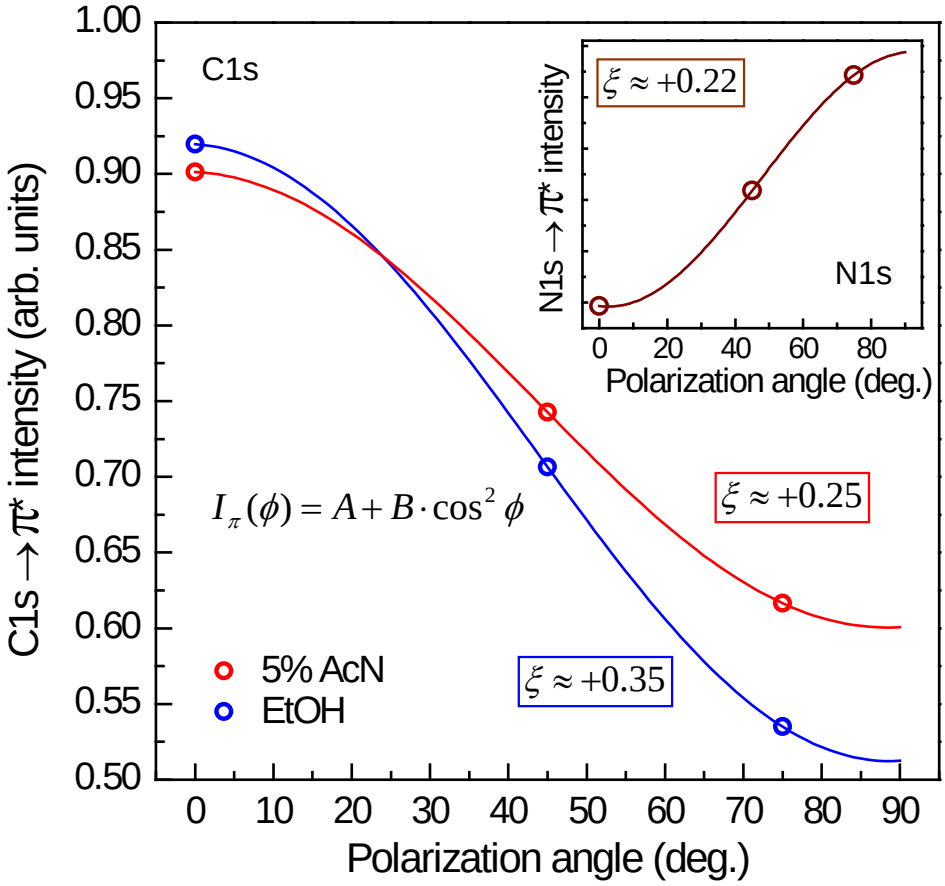

Figure 4.8: The relative data points of the C1s $\rightarrow \pi^\star$ and N1s $\rightarrow \pi^\star$ (inset) absorption edges from Figure 4.4 and Figure 4.5 shows angular-dependent XAS spectra. The data are fitted by $I_\pi(\phi) = A + B \cdot \cos^2(\phi)$.

Figure 4.5 reveals the polarization-dependent N1s intensity, indicating a confinement of N_2 molecules inside SWNTs. Meaning that these molecules are co-axially aligned in the interior of the narrow SWNTs. Following ξ calculation of SWNT array as expressed in Equation 4.2, the nematic order parameter ξ of the N_2 molecules is evaluated to be $\xi = +0.22$ (Figure 4.8, inset), which is comparable to ξ of +0.25 obtained from the C1s $\rightarrow \pi^\star$ absorption edge of the 5% AcN-grown SWNTs. The resulting lineshape spectrum of N_2 molecules, the unchanged lifetime of the x-ray-excited N1s π states, and the unaltered vibrational levels implies a tight effective c-axis in

the confining space [185, 186], and one-dimensional containment, unlike the finding of N_2 molecules in N-doped multi-walled carbon MWNTs [116, 187], or carbon nanofibers [113].

Considering the confinement of aligned N_2 molecule inside small-diameter SWNTs ($\sim$ 1 nm), the only interaction between nanotube and N_2 is van der Waals (vdW) interaction, which have in total the radius of 0.67 nm. The constant vdW radius of carbon and nitrogen atoms is merely fit within $\sim$ 1 nm SWNT, which does not allow N_2 to have a movement in radial configuration. In addition to vdW interaction, the fluctuating dipoles of nitrogen atoms will be bound in one direction.

Based on these considerations, the plausibility of one-dimensional diatomic N_2 inside small-diameter SWNT are evaluated using molecular dynamics (MD) simulations. MD simulation was performed by placing five N_2 molecules in the interior of two different 10 nm long SWNTs with comparable diameters with 5% AcN-grown SWNTs (*i.e.* (6,6) nanotube; $\sim$ 0.82 nm, and (7,7) nanotube; $\sim$ 0.96 nm). The interatomic potentials provided with the comparable package [188] were used to describe the system with the temperature of the system of 300 K. The C-C interaction was described using the adaptive intermolecular reactive empirical bond order (AIREBO) potential, and the C-N and N-N interactions were described using a Lennard-Jones potential with the coefficients used by Levitt *et al.* [189]. The N_2 bonds were treated as rigid rods by fixing the bond length. This allowed translation and rotation of the molecules, but ignored bending and vibrational modes.

Histograms showing the N_2 bond orientations with respect to the SWNT axis are shown in Figure 4.9. The continuous line shows the probability density distribution of a completely isotropic distribution due to growing differential solid angle $2\pi sin\theta d\theta$ (Figure 4.10). The probability density (P) in this case is expressed as,

$$P = \frac{1}{A_{\frac{1}{2}sphere}} 2\pi \boldsymbol{r}^2 \sin\theta = \frac{1}{2\pi \boldsymbol{r}^2} 2\pi \boldsymbol{r}^2 \sin\theta = \sin\theta,$$

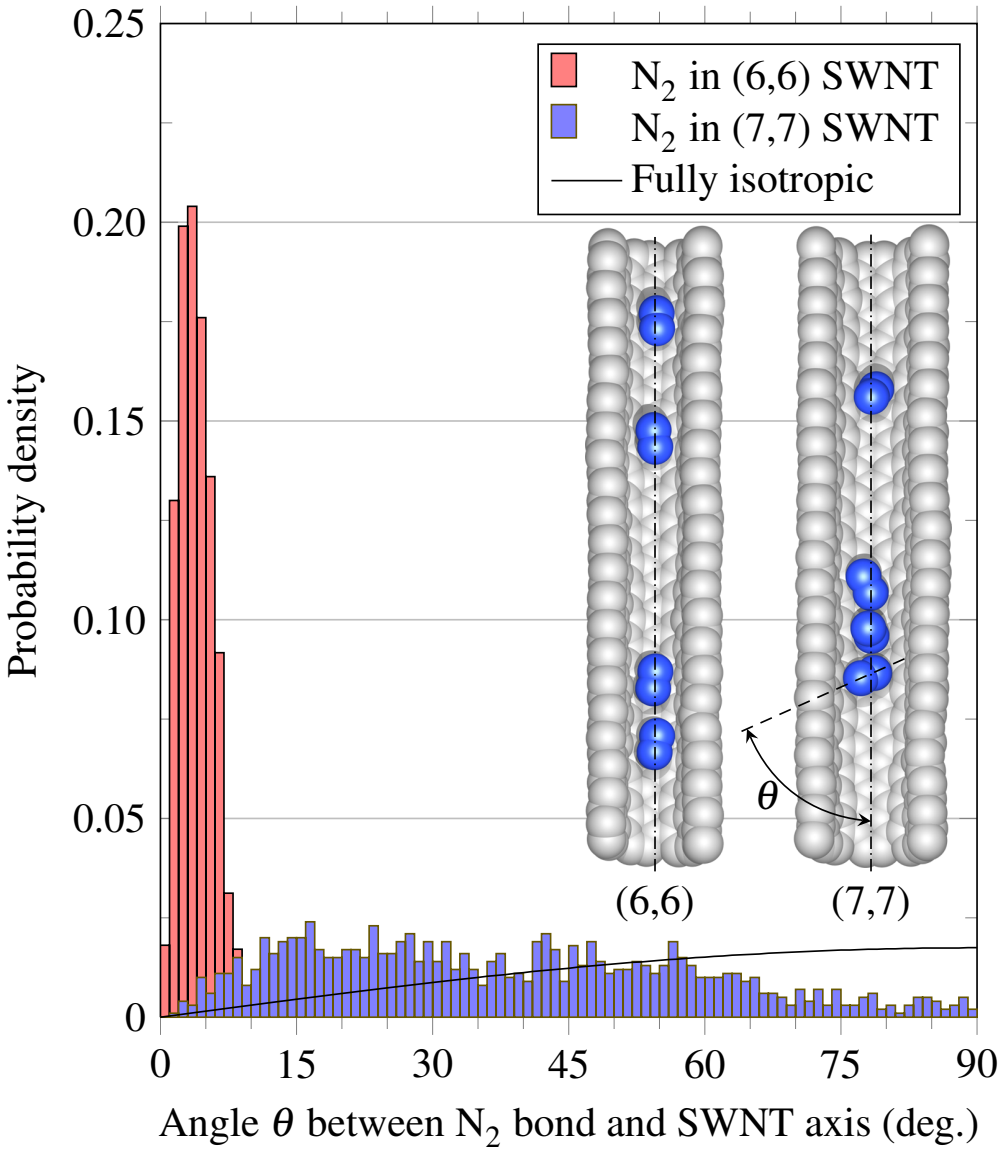

Figure 4.9: Distribution function of angle between N_2 bond and the nanotube axis. The insets are cuts of snapshots from the MD simulation for both (6,6) and (7,7) SWNTs. Adapted with permission from [117], Copyright © 2013 by Elsevier.

where number $\boldsymbol{r}$ with $\theta \sim \theta + \Delta\theta$ is $P\Delta\theta$. Considering alignment of encapsulated N_2, co-axial alignment of N_2 is much more apparent in the (6,6) nanotube, but the (7,7) nanotube is still sufficiently narrow that the N_2 are still preferentially oriented along the nanotube axis. Meaning that the individual molecules can frequently flip over inside the (7,7) nanotube, whereas never flipped inside the (6,6) nanotube. The use of interatomic potentials in the MD simulation corroborates that small-diameter SWNT – which provide an access for fluctuating dielectric displacements – are sufficient enough to confine N_2 molecules and yet tight enough to template co-axial alignment. The bond-polarizable vdW interactions can also explain the finding of aligned N_2 trapped inside larger MWNTs or hollow carbon-nitride nanofibers [114–116].

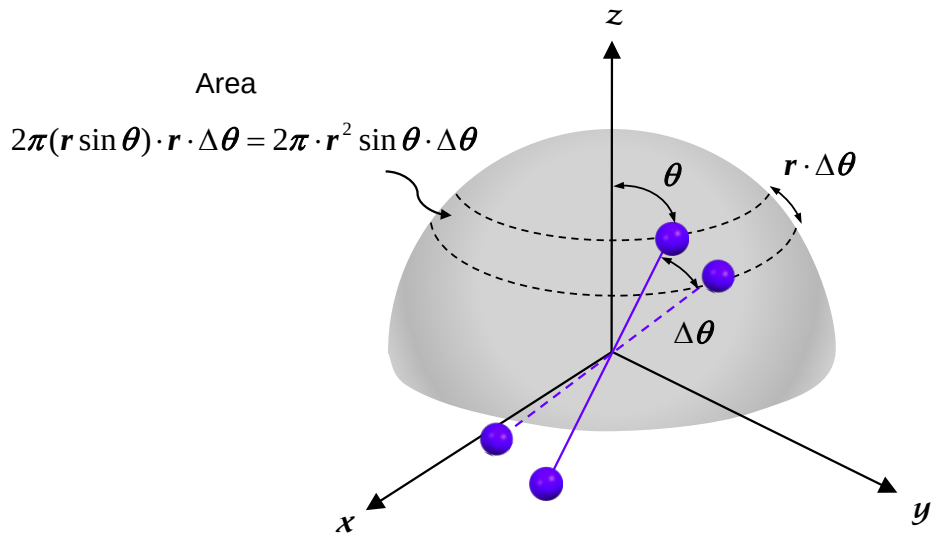

Figure 4.10: Sphere coordinate for a completely isotropic distribution due to growing differential solid angle $2\pi sin\theta d\theta$ shown in Figure 4.9 (continuous line).

Chapter 5

Multi-layered growth and growth mechanism

5.1 Introduction

The properties of SWNTs are strongly dependent on their structure, and typically become more enhanced as the nanotube diameter decreases. As a result, chirality and diameter control—particularly during synthesis—offers great potential for tuning the properties of SWNTs. It is widely accepted that the nanotube diameter is largely determined by the size of the catalyst nanoparticle, and this size relationship has been thoroughly studied [1, 19, 20, 37, 122, 123, 190–192]. Because of this relationship, there have been many attempts to reduce the SWNT diameter by reducing the catalyst particle size. SWNTs with diameters in the range of 0.6–1.1 nm have been synthesized by impregnating SiO_2 particles with Co/Mo [1, 122, 193]. A similar selectivity has been obtained using Co/Fe [3, 123], Fe/MgO [194], and Co incorporated into MCM-411 [195]. These methods, however, require the use of a powder, mesoporous material. Separating the SWNTs from the support requires significant post-processing, which can alter the SWNT properties.

Several methods to alter the SWNT structure during growth have also been demonstrated by changing growth temperature [19, 123], and/or pressure [196, 197]. Changes in diameter along a nanotube axis due to rapidly changing temperature have been previously reported for individual SWNTs [198], DWNTs [199], and other configurations of intramolecular junctions [200–205]. There are fewer studies on the influence of the precursor, but SWNT diameters have been found to be sensitive to abrupt changes in feedstock flux [206–208]. Tian *et al.* [209] recently demonstrated successful control over the diameter in the range of 1.2 to 1.9 nm by adjusting CO_2 concentration. Selectivity of diameter and chiral angle have also been shown by selective etching [210–213]. A reduction of mean SWNT diameter from 2.1 nm to less than 1 nm by incorporating acetonitrile (AcN, CH_3CN) into the ethanol (EtOH) feedstock has been presented in Section 3 [137, 140], but the role of nitrogen in this diameter change is not yet understood.

In this Section, I demonstrate *reversible* diameter modulation of vertically aligned SWNTs (VA-SWNTs) by adding acetonitrile to the feedstock during synthesis by alcohol catalytic chemical vapor deposition (CVD). This change was observed regardless of the sequence in which the carbon feedstocks were introduced. Based on this reversibility, investigation of the layer interface, and our previous findings we put forward an explanation of nitrogen's role in reducing the diameter of SWNTs.

5.2 Synthesis of multi-layered SWNT arrays

No-flow CVD was employed for synthesis of VA-SWNTs [136]. The Co/Mo binary catalysts were prepared as in our previous report [54]. Pure ethanol (EtOH) and a mixture of 5 vol.% of acetonitrile in ethanol (5% AcN) were used as precursor. Catalysts deposited on quartz or silicon substrates were reduced by flowing 300 sccm of Ar/H_2 (3% H_2) during heating (approximately 30 min). After reaching 800°C, the CVD chamber was evacuated and

40 μL of a liquid precursor stored in a small cap upstream was introduced by opening a valve. 5% AcN mixture was first introduced into reaction chamber for 2 min, after which the CVD chamber was evacuated to base pressure of 27 Pa (approximately 90 s) prior to sealing the CVD chamber and introducing pure EtOH for 90 s. EtOH supply was finally stopped, and 5% AcN was re-introduced until the growth stopped. The CVD chamber was then immediately cooled under 300 sccm of Ar flow. The actual pressures during EtOH or 5% AcN introduction increased from 1.4 to 2.6 kPa. The growth of VA-SWNTs was monitored *in situ* by a calibrated real-time measurement of the attenuation of a He/Ne (633 nm) laser passing through a quartz substrate supporting the growing films [214].

The morphology of the resulting multi-layered VA-SWNT arrays was imaged by scanning electron microscopy (SEM, 1 kV acceleration voltage, S-4800, Hitachi Co., Ltd.). For resonance Raman spectroscopy (Chromex 501is with Andor DV401-FI), a laser with excitation wavelength of 488 nm was incident on the cleaved cross-section of the VA-SWNT films using a 50× objective lens with a laser power of 0.5 mW. For cross-sectional Raman measurements in Figure 5.3 and 5.4, the incident laser light was polarized perpendicular to the nanotube axis in order to maximize the contrast of RBM features [183].

In addition, the double-layered SWNT arrays were synthesized by first introducing EtOH, followed by 5% AcN. The feedstocks were also introduced in the reverse order. The evacuation time to the background pressure of 27 Pa was 90 s, and the actual pressures during EtOH or 5% AcN introduction were raised up from 1.4 to 2.6 kPa. The double-layered sample in which EtOH and 5% AcN were introduced as the first and second feedstocks, respectively, were dispersed in ethanol, and the mean diameter of EtOH- and 5% AcN-grown SWNTs were observed by transmission electron microscopy (TEM, JEOL 2000EX operating at 200 kV). In addition, as-grown five-layer VA-SWNT array was gently dispersed in ethanol, and sonicated for a few minutes prior to dropping onto a TEM grid with a holey carbon film. Dispersed five-layer

array was observed by high-resolution transmission electron microscope (HRTEM, JEM-ARM200F operated at 200 kV) and low-angle annular dark-field STEM (LAADF-STEM, JEM-2800 operated at 200 kV and detector angle of 34–157 mrad). The CoNTub algorithm [215] was used to generate the nanotube heterojunction structures for the growth model.

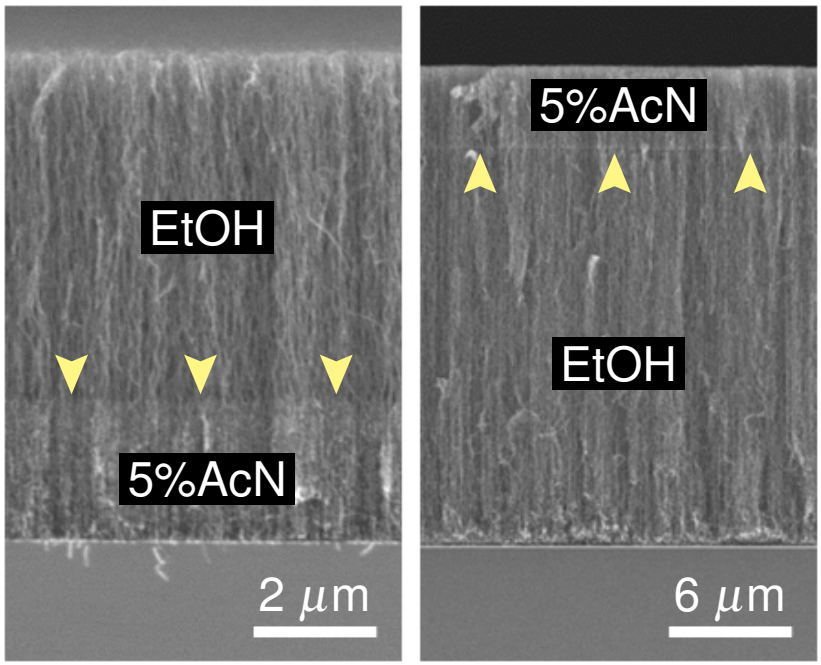

Figure 5.1: SEM micrographs of double-layer VA-SWNT arrays synthesized from ethanol (EtOH) and 5 vol.% acetonitrile (AcN). Left and right panels show different feedstock sequence, with growth initiated by EtOH (left) and AcN (right). Yellow arrows mark the interface between the regions grown from different feedstocks. Reproduced with permission from [216], Copyright © 2013 by The American Physical Society.

5.3 Catalyst-Independent Diameter Modulation

Figure 5.1 demonstrates double-layer growth of SWNTs. The left panel shows VA-SWNTs in which the feedstock was changed from EtOH to 5% AcN. The right panel shows VA-SWNTs grown from the reversed sequence of carbon feedstocks. Since the formation of VA-SWNTs is known to be a root-growth process [136], the top part of the array is formed first and the part nearest the substrate is formed last. The interface between the EtOH-grown and 5% AcN-grown regions is clearly visible in the SEM images (indicated by arrows in Figure 5.1) as the diameter changes significantly (Figure 5.3).

Figure 5.2 shows growth profiles of the VA-SWNT arrays shown in Figure 5.1. The growth process was monitored in real-time using *in situ* optical absorbance [214, 217], and the two stages are depicted by blue lines for EtOH and red lines for 5% AcN. The growth rates determined from the slope of the linear growth region were 3 μm per minute for EtOH (*Et*-SWNT) and 1.5 μm per minute for 5% AcN (*Ac*-SWNT).

Figure 5.3 shows resonance Raman spectra of double-layer VA-SWNTs obtained from the sidewall of a cleaved array using an excitation wavelength of 488 nm. The radial breathing mode (RBM) peaks reveal specific SWNTs that are in resonance with the excitation laser, and the frequency is diameter dependent [144, 218]. Here the empirical relation according to Equation 3.1 [141] is used to estimate the tube diameter. The very different Raman spectra obtained from as-grown *Et*-SWNT and *Ac*-SWNT are shown in Figure 5.3a. The increased D-line intensity is a common characteristic once N is incorporated [219, 220]. In the case of *Ac*-SWNT, the 488 nm excitation wavelength is in resonance with the first optical transition of small-diameter metallic SWNTs $\left(E_{11}^{M}\right)$ (see Figure 3.4b), as seen in the appearance of RBM peaks at 240 and 260 cm^{-1} and increasing intensity of the BWF line shape. Peaks from larger-diameter semiconducting *Et*-SWNT

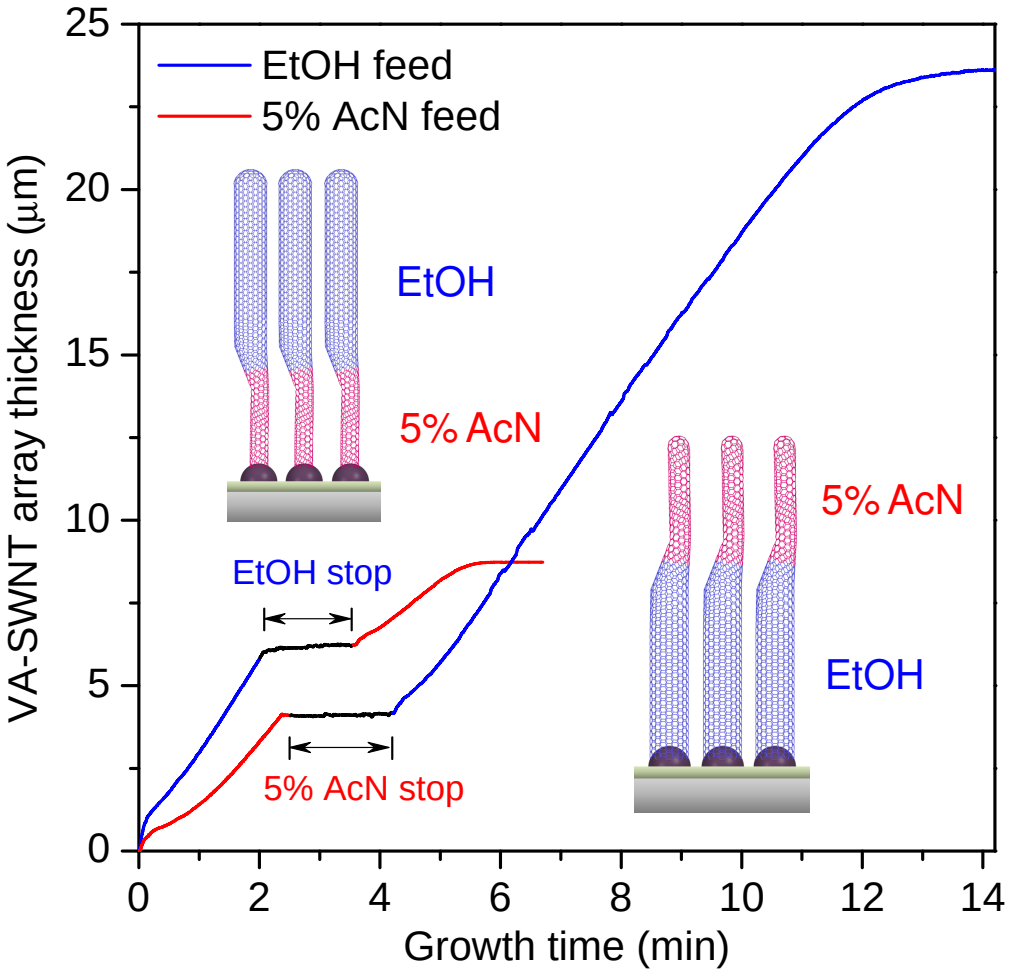

Figure 5.2: Growth curves of double-layers SWNT arrays synthesized from ethanol (EtOH) and 5% acetonitrile (5% AcN) monitored by *in-situ* measurement. Blue and red labels represent SWNTs synthesized from EtOH and 5% AcN feedstocks, respectively. Reproduced with permission from [216], Copyright © 2013 by The American Physical Society.

at 145 and 160 cm^{-1} originate from resonances of the E_{33}^S and E_{44}^S optical transitions.

Figure 5.3 reveals a catalyst-independent change in the diameter of SWNTs caused by changing the feedstock gas from EtOH to 5% AcN (*Et*→*Ac*-SWNT), as well as for the reverse (*Ac*→*Et*-SWNT). Resonance Raman spectra from VA-SWNTs synthesized from an unchanging feedstock gas

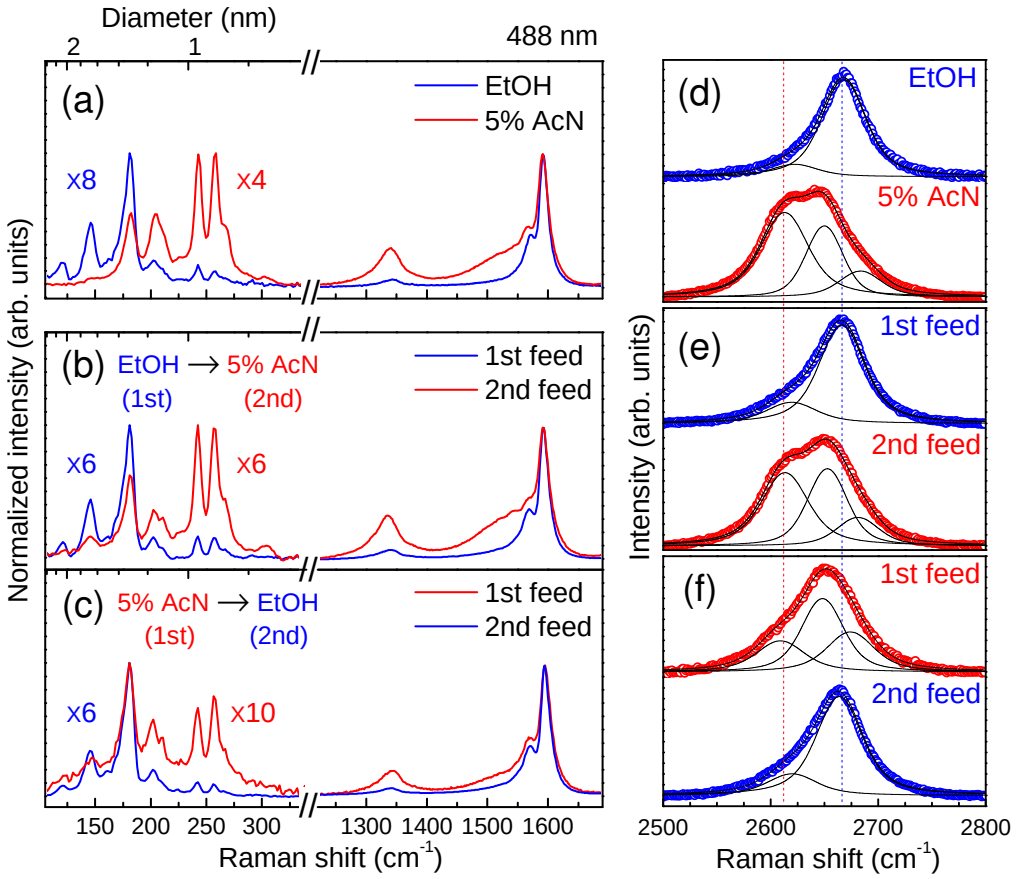

Figure 5.3: Resonance Raman spectra for RBM and G band (a-c) and the 2D (G′) peak region (d-f) of different SWNT layers synthesized from ethanol (EtOH, blue line/label) and 5 vol.% acetonitrile (5% AcN, red line/label) feedstocks. Excitation wavelength is 488 nm and the laser is polarized perpendicular to the nanotube axis. Reproduced with permission from [216], Copyright © 2013 by The American Physical Society.

(*Et*-SWNT or *Ac*-SWNT) are shown for reference. The strong BWF feature and D-line of the 5% AcN layer are identical to the features found in the *Ac*-SWNT spectrum as seen in Figure 5.3a. The diameter along the array is reduced in *Et*→*Ac*-SWNT when the feedstock is switched to 5% AcN as shown in Figure 5.3b by the appearance of dominant small-diameter RBM peaks around 230–270 cm^{-1} ($d < 1\,\mathrm{nm}$) [140]. On the other hand, in *Ac*→*Et*-SWNT an increase in diameter (up to 2.1 nm) is observed (Figure 5.3c) with

RBM peaks appearing between 140 and 220 cm^{-1} when EtOH is introduced later.

Resonance Raman spectra of the 2D (G′) line were obtained using the same 488 nm excitation wavelength (Figure 5.3(d-f)). Blue and red open circles represent the G′ spectra of VA-SWNTs synthesized from EtOH and 5%AcN, respectively. The G′ peaks were decomposed using two Voigtian peaks centered at 2620 and 2666 cm^{-1} for *Et*-SWNT, *Et*→*Ac*- and *Ac*→*Et*-SWNT (EtOH-grown layers), and three Voigtian peaks at 2610, 2650 and 2680 cm^{-1} for *Ac*-SWNT, *Et*→*Ac*- and *Ac*→*Et*-SWNT (5%AcN-grown layers). All peak components (black solid lines) were fitted with a constant full-width at half-maximum (FWHM) of 19.7 cm^{-1}, and G′ band spectra from unchanging feedstock are shown in Figure 5.3d.

Figures 5.3(d-f) show identical G′ spectra for EtOH-grown SWNT arrays at the position of 2666 cm^{-1} in all cases. The similar spectra of 5%AcN-grown SWNTs were obtained from *Ac*-SWNT, *Et*→*Ac*-SWNT and *Ac*→*Et*-SWNT from 5%AcN-grown layers. A large downshift is due to the vast difference in SWNT diameter, which has been observed in previous studies on N-doped SWNTs [140, 142, 147]. These data clearly show that *Ac*-SWNTs and *Et*-SWNTs always have their characteristic diameter distribution, regardless of the sequence of feedstock introduction.

5.4 Diameter reversibility

In order to determine whether or not the diameter of SWNTs within the same array can be modulated by changing the feedstock we split the growth into multiple stages as follows. We first initiated VA-SWNT synthesis using 5 vol. % acetonitrile in ethanol (5% AcN). After 2 min of synthesis we stopped the feedstock supply for 90 s, then supplied pure ethanol (EtOH) into the CVD chamber. After exposure to ethanol for 90 s, we again stopped the supply and changed the feedstock back to 5% AcN. A scanning electron microscope (SEM) image showing a cross-section of the resulting array is

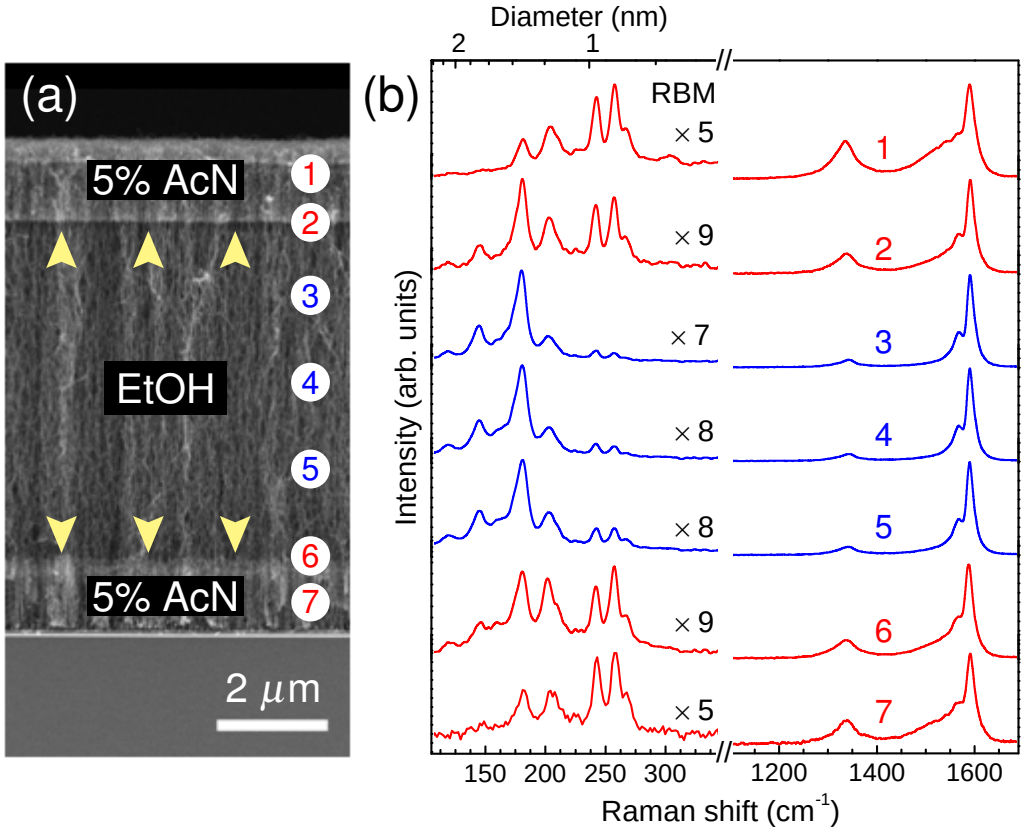

Figure 5.4: Reversibility of SWNT diameter demonstrated by growth of a triple-layered SWNT array characterized by SEM (a) and 488 nm resonance Raman spectra (b). The yellow arrows in (a) denote the interfaces between different SWNT layers. Reproduced with permission from [216], Copyright © 2013 by The American Physical Society.

shown in Figure 5.4(a). The VA-SWNT array is composed of three layers, with the interface between layers (indicated by arrows) appearing as a change in contrast in the SEM image. Since the formation of VA-SWNTs is known to be a root-growth process [136] the upper part of the array is formed first, and the part nearest the substrate is formed last.

Resonance Raman spectra were obtained at several points along the height of the array, with the approximate positions indicated by the circles numbered 1–7 in Figure 5.4(a). Raman spectra corresponding to these positions are shown in Figure 5.4(b). The very different spectra along the

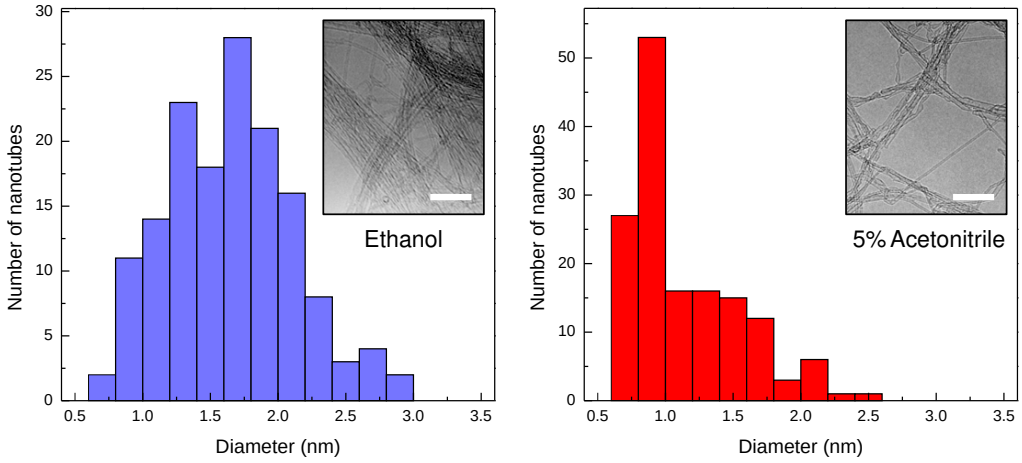

Figure 5.5: Histograms showing SWNT diameter distributions obtained from TEM observations of pure ethanol-grown (left panel) and 5% acetonitrile-grown SWNTs (right panel) in a double-layered sample. The observed mean diameters are 1.66 ± 0.46 nm and 1.14 ± 0.40 nm, respectively. TEM images of both regions are depicted in insets with scale bar of 20 nm, and the number of measurements $N = 150$ for each case. Reproduced with permission from [216], Copyright © 2013 by The American Physical Society.

array indicate the layers are comprised of very different nanotubes. Spectra obtained from the central region (points 3, 4, and 5) are typical of ethanol-grown VA-SWNTs (*Et*-SWNTs), whereas the spectra obtained from regions above and below (points 1, 2, 7, and 8) are remarkably similar to those grown from 5% AcN (*Ac*-SWNTs) [140].

The low-energy radial breathing mode (RBM) peaks originate from SWNTs of a specific chirality that are in resonance with the excitation laser (here, 488 nm), and the frequency of this mode is known to have a clear diameter dependence [144, 218]. On the basis of the RBM spectra in Figure 5.4b, the layers containing *Ac*-SWNTs appear to have considerably smaller diameters than the *Et*-SWNT layer. The strong presence of RBM peaks associated with small-diameter SWNTs for the 5% AcN case — and the absence of these peaks in the EtOH case — is strong evidence for diameter reduction. These data clearly show that *Ac*-SWNTs and *Et*-

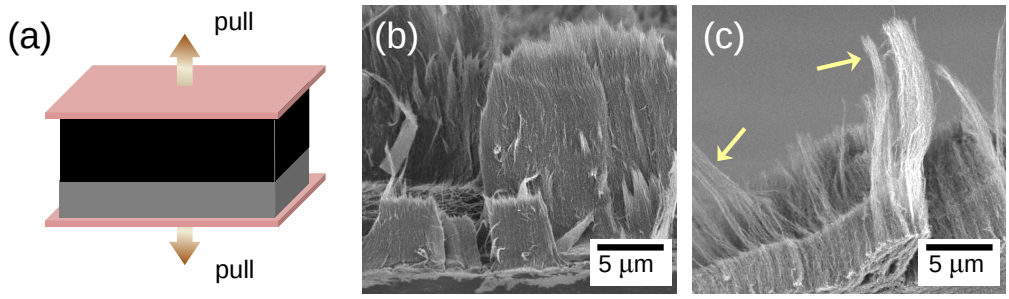

Figure 5.6: Interface examination (a) and SEM images of SWNT arrays synthesized, respectively, from 5% AcN and EtOH (b) in which the top layer was attached to adhesive tape before detaching the bottom layer with some of continuous nanotubes indicated by yellow arrows (c). Reproduced with permission from [216], Copyright © 2013 by The American Physical Society.

SWNTs maintain their characteristic diameter distribution, regardless of the sequence of feedstock introduction.

While the Raman spectra of the double-layered arrays are consistent with those shown in an earlier report in which we confirmed the significant diameter reduction when using acetonitrile [140], we acknowledge the mean diameter and diameter distribution cannot be rigorously determined only from these spectra. Therefore, we performed transmission electron microscope (TEM) observations on the different layers of a double-layered sample (Figure 5.3) in which EtOH was introduced first, followed by 5% AcN. Diameter measurements made from the images indicate a reduction in mean diameter from 1.66 ± 0.46 nm to 1.14 ± 0.40 nm when the feedstock was changed from EtOH to 5% AcN (see Figure 5.5).

5.5 Interface examination

In order to determine the role of nitrogen, we must examine what happens at the interface between the layers. Several previous studies of multi-layered SWNT growth have reported that two different layers of carbon nanotubes [221–223] are very weakly connected at the interface. We examined the strength of the interlayer connection by detaching the top layer

of a double-layered array from the bottom layer using adhesive tape. We removed the entire array from the growth substrate by attaching tape to the top surface of the array (*Ac*-SWNTs, A) and peeling the array away from the substrate. Another piece of tape was then attached to the bottom surface of the array (*Et*-SWNTs, B), and the two pieces were then separated. SEM images obtained after separation are shown in Figures 5.6(a-c). As seen in the figures, most of the layers cleanly separated from each other, indicating that the majority of SWNTs are not connected at the interface. However, some

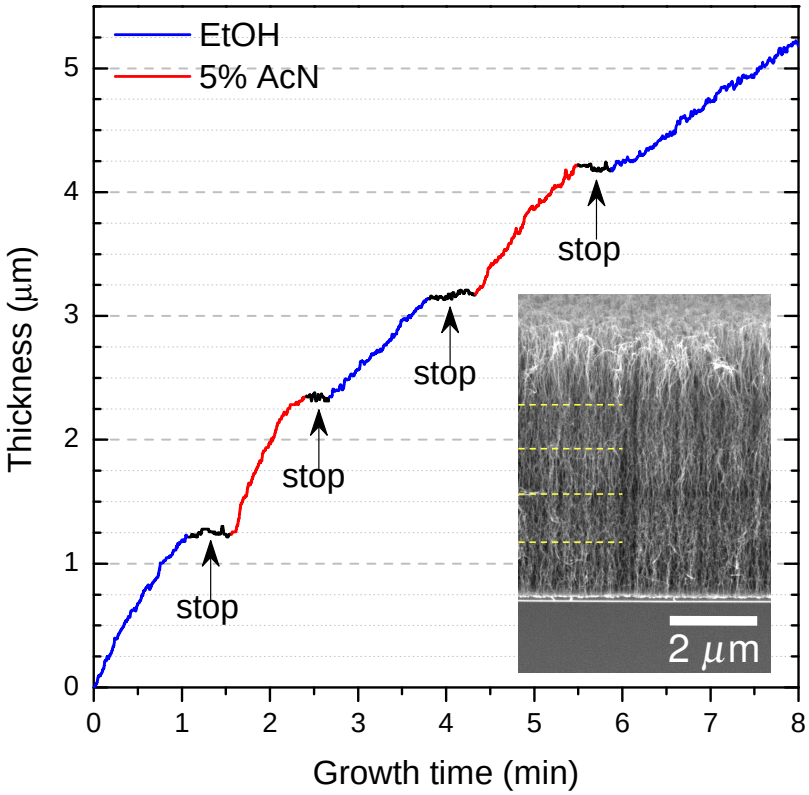

Figure 5.7: Growth curve of a five-layer VA-SWNT array synthesized by switching between ethanol (EtOH) and 5% acetonitrile (5% AcN) feedstocks. Introduction of each feedstock was separated by approximately 30 s during which the previous feedstock was evacuated. A cross-sectional SEM image is shown in the inset with interfaces indicated by dashed yellow lines. Reproduced with permission from [216], Copyright © 2013 by The American Physical Society.

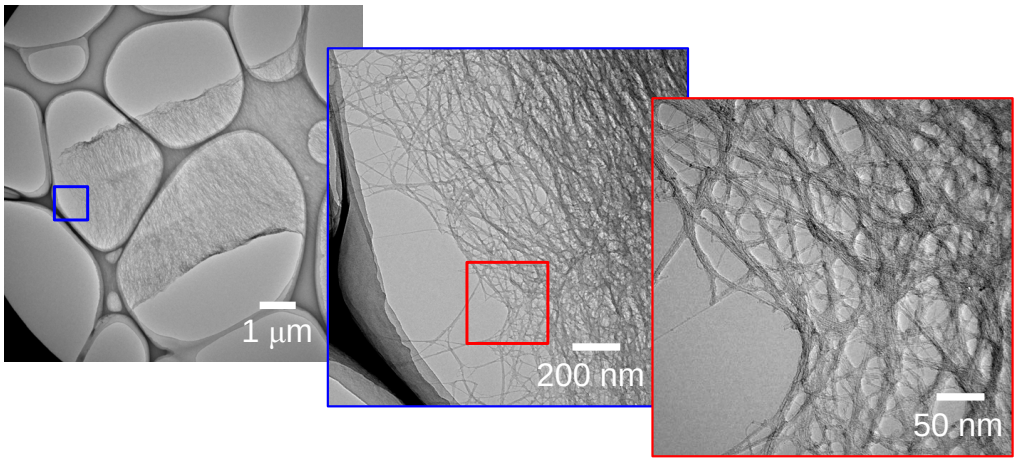

Figure 5.8: TEM images of a multi-layered SWNT array (see Figure 5.7) show clear interfaces between the layers. Reproduced with permission from [216], Copyright © 2013 by The American Physical Society.

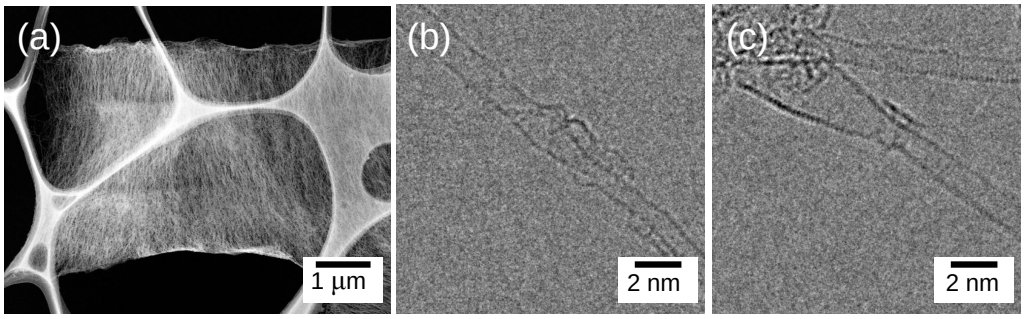

Figure 5.9: LAADF-STEM image of five layers array (a) with observable nanotube junctions between small- and large-diameter SWNTs observed from the interface region by HRTEM (b, c). Reproduced with permission from [216], Copyright © 2013 by The American Physical Society.

areas remained connected (indicated by arrows in Figure 5.6(c)), suggesting some of the SWNTs could be continuous through the interface.

A 5 μm, five-layer SWNT array was synthesized for interface examination (see Figure 5.7 and 5.8). Its low-angle annular dark-field STEM (LAADF-STEM) image is depicted in Figure 5.9(a) in which the interface can be clearly seen. Figures 5.9(b, c) show high-resolution TEM (HRTEM) images of five-layer arrays. These images clearly show a nanotube changing diameter

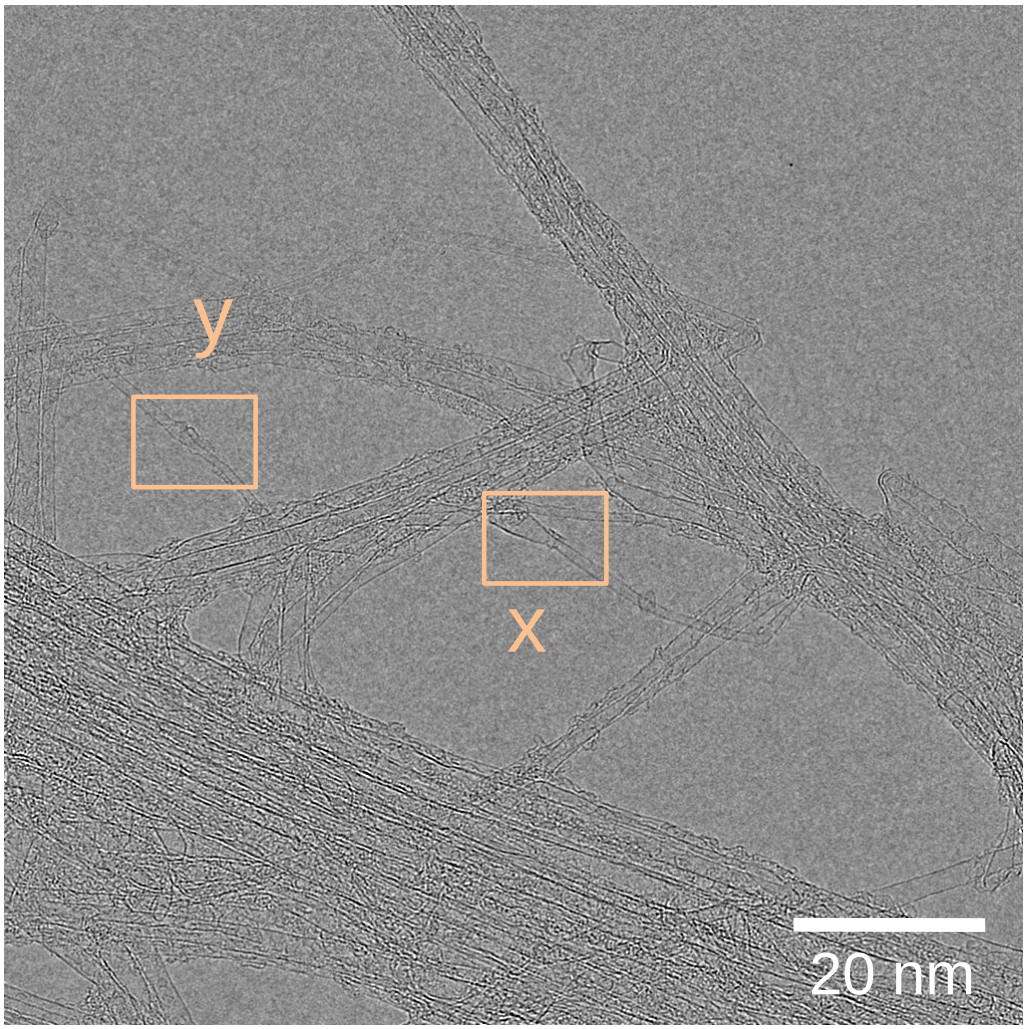

Figure 5.10: HRTEM images of nanotube junctions in the interface region between EtOH- and 5% AcN-grown layers. Reproduced with permission from [216], Copyright © 2013 by The American Physical Society.

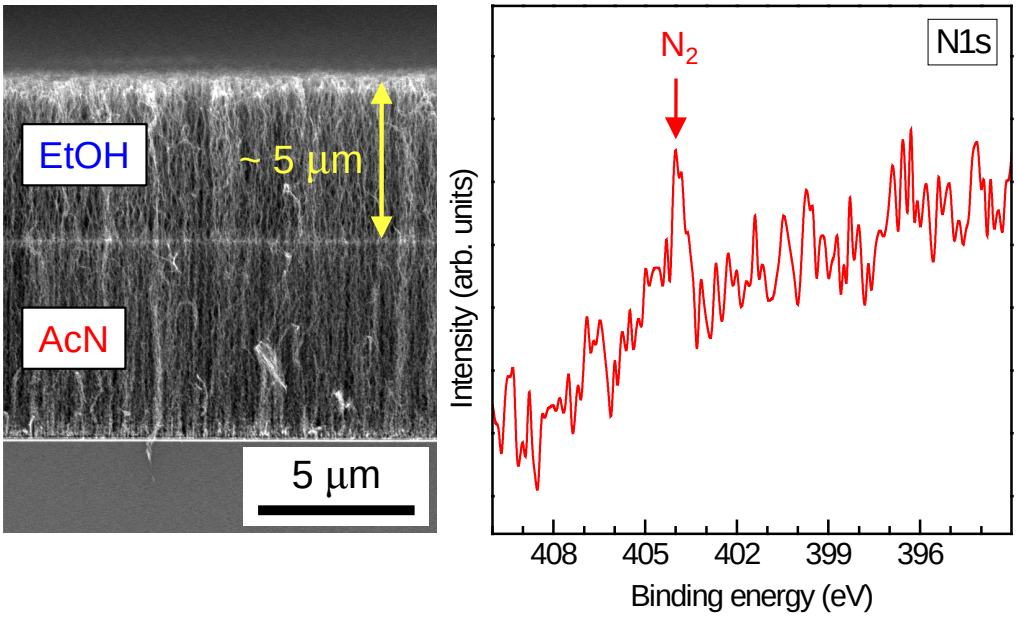

Figure 5.11: XPS spectra performed on the top of vertically aligned double-layered SWNT array synthesized from EtOH and 10% AcN, respectively (left panel), showing the presence of molecular N_2 in N1s core level (right panel).

from 1.2 nm to 0.8 nm in (b), and from 2.4 nm to 1.1 nm in (c), which were obtained from the interface region in Figure 5.10 at spot x and y, respectively. Although statistics could not be performed regarding the frequency of junctions due to entanglement of nanotubes at the interface, these observations demonstrate some SWNTs can be connected across the interface.

Additionally, one can think of investigation of interface connection by determining amount of encapsulated N_2 molecules undergo alteration between two different nanotubes (*i.e.* *Ac*- and *Et*- SWNTs). By considering this point, XPS measurement was performed on the top of vertically aligned double-layered SWNT array synthesized, respectively, from EtOH and 10% AcN. Figure 5.11 shows the viability of N_2 molecules inside EtOH-grown SWNTs (top layer), indicating migration of N_2 molecules from the bottom (10% AcN) to the top (EtOH) of the array. Note that a 5μm thickness of the top layer

is beyond escaping depth of photoelectrons. There is, therefore, no N_2 signal detected from interface region where feedstock was switched from EtOH to 10% AcN. The content of N_2 presented at the top is found to be ~ 0.07 at.% (23%) from pristine 10% AcN-grown SWNTs (0.3 at.%).

5.6 Role of nitrogen and growth mechanism

As previously mentioned, abrupt changes in growth conditions such as temperature [198, 199] and feedstock flux [206–208] have been reported to induce continuous junctions in SWNTs and DWNTs. While the temperature was unchanged in the experiments reported here, the presence of nitrogen may have altered the flux of carbon into the catalyst. It has been shown that the mean diameter of SWNTs grown from EtOH is dependent on precursor supply [37, 224], but the sensitivity is not enough to explain the findings reported here based on the availability of carbon. We suspect, however, that nitrogen acts only at the catalyst surface, disrupting the SWNT formation.

It is well-established that incorporation of nitrogen will easily induce defects into the SWNT structure [90], and density functional theory (DFT) calculations [119] have shown that the binding energy between Co and N is higher than between Co and C. This means any nitrogen present on the catalyst will be less mobile than the surrounding carbon. This condition has been predicted to result in narrower SWNTs [130].

Fiawoo *et al.* [225] recently proposed that SWNT formation occurs near the edge of a catalyst particle when the growth condition is near thermodynamic equilibrium. This is called a 'tangential' growth mode, and explains why the diameter of a SWNT is typically dependent on the catalyst particle size. This also explains the gradual increase of mean diameter that typically results from increasing the growth temperature [37, 198, 199, 226, 227]. Away from thermodynamic equilibrium, a 'perpendicular' growth mode is possible, in which the SWNT diameter is independent of the catalyst particle size. These growth modes have been studied by *in situ*

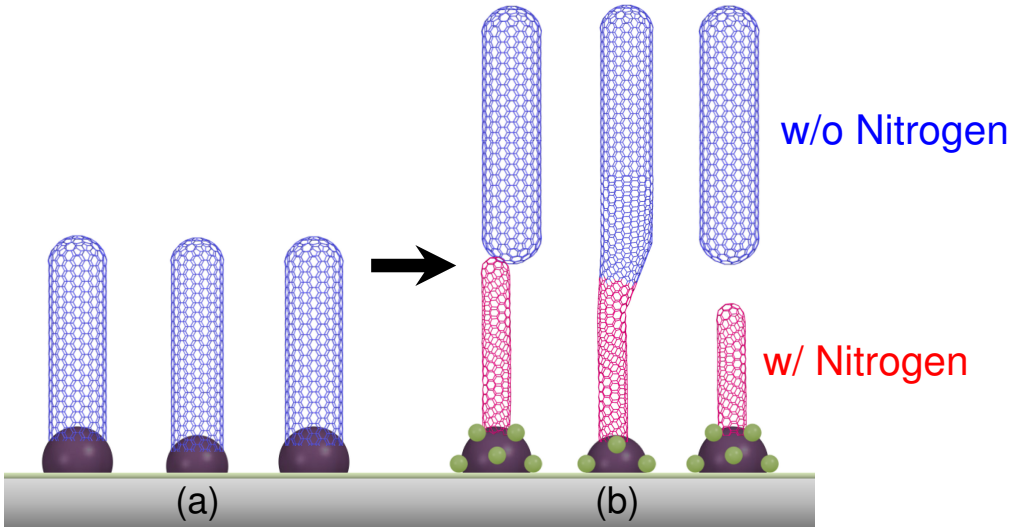

Figure 5.12: A possible mechanism of diameter change along VA-SWNT array from Co catalyst nanoparticles (a) without and (b) with N (green ball). Blue and red tubes represent larger and smaller SWNTs synthesized from ethanol (EtOH) and 5 vol.% acetonitrile (5% AcN), respectively. Reproduced with permission from [216], Copyright © 2013 by The American Physical Society.

TEM observation [225, 228]. Fiawoo *et al.* [225] proposed that nucleation occurs primarily by the perpendicular mode, which is dominant during the early stage of nanotube growth. After nucleation and the growth process approaches equilibrium, the tangential mode becomes dominant and remains so until growth stops.

Considering our experimental findings in light of the available literature, we propose the diameter change caused by the presence of nitrogen is due to a process at the catalyst surface that causes a change from the tangential to the perpendicular growth mode. We rule out formation of a nitride with the metal catalyst because that is unlikely to be reversible. Furthermore, the production of N_2 during synthesis [117] suggests a mechanism by which nitrogen could often leave the catalyst, thereby being reversible. Moreover, a process which only occurs at the catalyst surface helps explain why a small percentage of nitrogen can have a significant effect.

We propose the role of nitrogen is as follows. In the presence of pure ethanol, SWNTs grow by the tangential growth mode. The diameters of the SWNTs are therefore similar to the catalyst diameters, which are approximately 2 nm [59, 140]. When nitrogen is introduced into the system, some nitrogen atoms adsorb onto the surface of the catalyst particles. Since N interacts more strongly with the Co nanoparticles than C, the less-mobile N frustrate the formation of the sp^2 network that is to become the nanotube sidewall. As a result, it becomes difficult to sustain the tangential growth mode, and the perpendicular growth mode becomes energetically favorable (*i.e.* active area for nanotube formation is minimized), which is not applicable by the explanation catalyst elongation [119]. It is possible for the transition between growth modes to be continuous, resulting in SWNT junctions like those shown in Figures 5.9(b) and (c), but discontinuous growth is more likely. A schematic of this diameter change is shown in Figure 5.12.

As reported in Ref. [140], the diameter distribution of *Ac*-SWNTs is considerably narrow, which is expected for the perpendicular growth mode. While nucleation from different small-diameter catalyst particles is a possible alternative explanation, we expect such small catalyst particles to be quite few in number thus unable to initiate vertically aligned growth (Figure 5.1 and 5.4(a)). Synthesis of small-diameter SWNTs from larger catalyst particles *via* the perpendicular mode would result in more SWNTs and would be less sensitive to nanoparticle diameter. By considering how nitrogen could, furthermore, react at the catalyst surface before forming N_2, the tangential growth mode would plausibly hinder nitrogen to act at the catalyst surface due to cohesion of carbon chain surrounding the catalyst particle as observed in MD simulation. Nitrogens could, on the other hand, in case of perpendicular growth mode enter through sub-surfaces.

Chapter 6

Conclusion and prospect

These findings of very different diameters of nanotubes within VA-SWNT arrays synthesized from acetonitrile and ethanol demonstrate that changes in SWNT diameter can be achieved without any changes in catalyst preparation. Furthermore, the finding that nanotubes of very different diameters can be synthesized within the same VA-SWNT array by changing the carbon precursor demonstrates that the SWNT diameter can be substantially changed without altering the catalyst preparation. The compelling reduction in mean diameters is found to be from 2.1 nm for ethanol-grown SWNTs to just 0.8 nm for acetonitrile-grown VA-SWNTs. A correlation between the reduction of the SWNT diameter and an approximately one atomic percent saturated incorporation of nitrogen is well established. This narrowing of nanotube diameter occurs for growth on flat substrates as well as on zeolite powder, indicating that N takes an active role in yielding sub-nm diameter SWNTs, independent of catalyst preparation. Catalyst-particle-independent diameter control by trace amounts of heteroatoms represents a versatile pathway for the direct synthesis of engineered SWNT.

A significant small-diameter VA-SWNT array can be in the presence of nitrogen during CVD synthesis filled with N_2 molecules when acetonitrile/ethanol mixture is used as a feedstock. Interestingly, trapped N_2 molecules are compelled to be aligned inside the interior one-dimensional

(1D) space , indicating vastly small-diameter VA-SWNTs synthesized from acetonitrile mixture are sufficiently narrow as demonstrated in Chapter 3 to strictly confine 1D arrangement of trapped N_2 as indicated by polarized high-resolution NEXAFS measurement. The combined molecular dynamic simulation results also demonstrate the suitable confinement for N_2 molecules in the sufficient small-diameter (6,6) nanotube ($\sim 0.82\,\mathrm{nm}$).

A growth mechanism are further demonstrated by multi-layered growth of vertically aligned SWNTs in which the layers have vastly different diameters. The empirical finding convincingly shows that this diameter change is both reversible and repeatable, and suggests that the diameter of substrate-supported SWNTs can be changed *on-demand* without the need to alter catalyst preparation or chemistry. Such growth is also independent of the sequence in which the precursors are introduced. The result suggest this diameter reduction is due to nitrogen at the catalyst surface impeding SWNT formation, which causes the growth mode to change from tangential to perpendicular. This change can be continuous, but termination and re-nucleation of growth is more likely. The ability to easily and efficiently modulate the nanotube diameter during SWNT growth is crucial for bottom-up fabrication of carbon nanotube materials and devices.

Future work may be focused on:

1. Characterization and control nitrogen configurations, including electronic and electrical properties of N-doped SWNTs for field-effect transistor performance;
2. Controlling the ratio between semi-conducting and metallic N-doped SWNTs;
3. Direct control chirality by nitrogen contribution;
4. Gaining SWNT yield on flat substrate for future applications;
5. Fabrication of nanotube composites;
6. Transport properties study on double-layered SWNT arrays;
7. Revealing, characterizing, and studying physics of N-doped SWNT characteristic using spectroscopy approach.

Appendix

Additional analysis data of resonance Raman spectroscopy on degree of alignment of vertically-aligned single-walled carbon nanotube (VA-SWNT) array in Chapter 4 [184].

VA-SWNT array were synthesized from Co/Mo binary catalysts by no-flow chemical vapor deposition (CVD) process [136] (see Chapter 3). A pure ethanol and 5% acetonitrile (5% AcN) were used as feedstocks. A linearly polarized Raman laser of 488 nm excitation wavelength with 0.5 mW (Chromex 501is with Andor DV401-FI) was exposed on the cleaved side wall of an array with focused with a 50× objective lens. The incoming and outgoing polarizations fixed in parallel (VV) configuration. The resonance Raman spectra were recorded by rotating the sample and refocusing to maximize Raman signal, while maintaining the spot position. The spectra were measured every 10° step forward. The signals were accumulated for 5 min for each measurement as shown in Figure A.1. As the polarization angle is rotated from perpendicular to parallel to the nanotube axis, absorption by nanotube is also enhanced, which causes a downshift in Raman frequency. The effect of laser heating were, therefore, corrected by correcting the G-band spectra intensity (areas) in which the temperature resulted in the sample is calculated using the following equation [229],

$$\omega(T) = \omega_0 - \frac{A}{\exp(B\hbar\omega_0/k_B T) - 1},$$

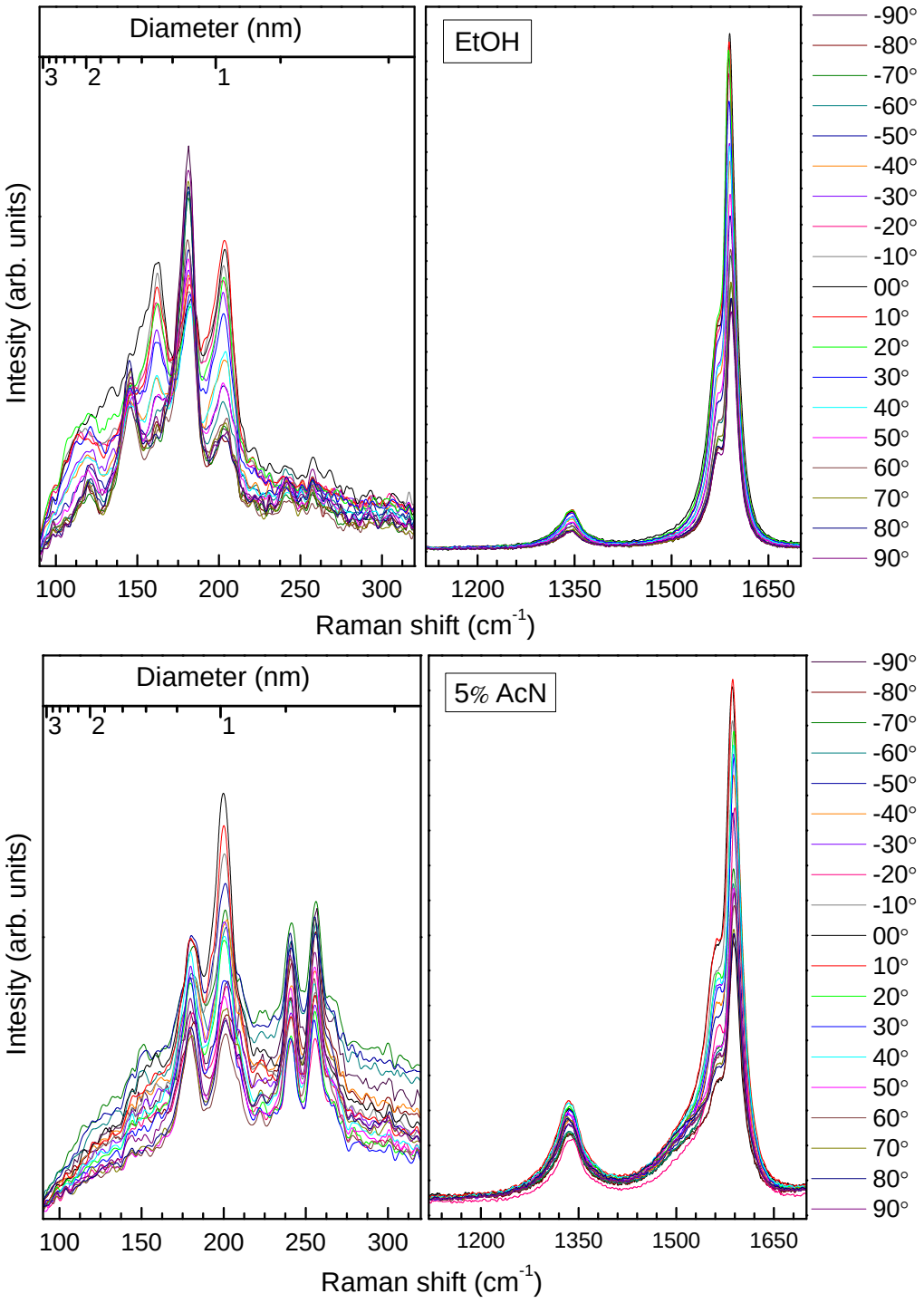

Figure A.1: Polarization-dependent Raman spectra of aligned SWNTs with 10° rotation step forwards.

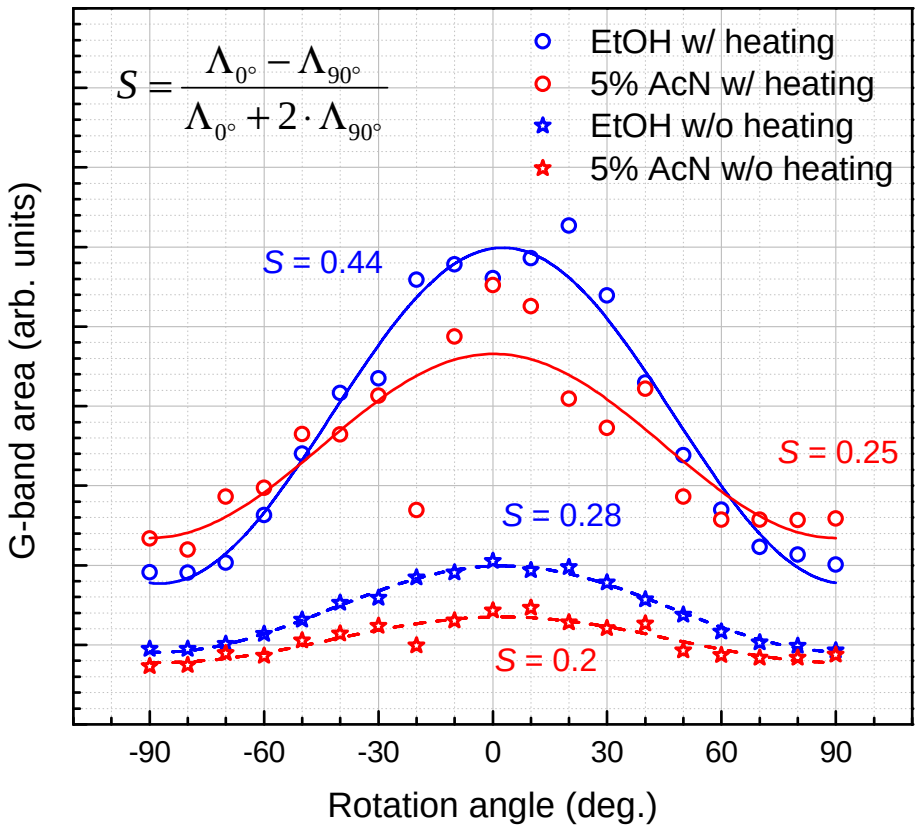

Figure A.2: Nematic order parameter (S) of VA-SWNT arrays synthesized from pure ethanol (blue) and 5% acetonitrile (AcN) before and after temperature corrections, show an increase in S value, indicating different alignment of both VA-SWNT batches.

where $\hbar$ is Planck's constant, k_B is Boltzmann's constant, T is the sample temperature, and ω_0 is the G-band frequency without laser heating ($1594\,\mathrm{cm}^{-1}$), while $A = 38.4\,\mathrm{cm}^{-1}$, and $B = 0.438$. The G-band intensity (expressed by its area) caused by temperature change is expressed according to the following equation,

$$I = I_0 \exp(-\frac{T}{B}) = I_0 \exp(-\frac{T}{430})$$

where T is the sample temperature, I_0 denotes as the Raman intensity at 0 K, while B is the constant from fitting values as described elsewhere [229]. The constant B in this case is 430.

The nematic order parameter (S) is calculated from different dipole transition of parallel and perpendicular transitions, respectively, according to the equation,

$$S = \int \frac{1}{2}(3\cos^2\theta - 1) f sin\theta \mathrm{d}\theta \mathrm{d}\phi = \frac{\Lambda(0) - \Lambda\left(\frac{\pi}{2}\right)}{\Lambda(0) + 2\Lambda\left(\frac{\pi}{2}\right)},$$

where θ is the polarization angle, and $\Lambda(0)$ and $\Lambda(\frac{\pi}{2})$ is the intensities at the polarization angle of 0° and 90°. Following the temperature correction, the nematic order parameters (S) from polarization Raman analysis are evaluated to be 0.44 and 0.28 for ethanol and 5% AcN samples, respectively (Figure A.2).

Bibliography

[1] B. Kitiyanan, W. E. Alvarez, J. H. Harwell, and D. E. Resasco, *Chem. Phys. Lett.* **3**17, 497 (2000).

[2] P. Nikolaev, M. J. Bronikowski, R. Bradley, F. Rohmund, D. T. Colbert, K. Smith, and R. E. Smalley, *Chem. Phys. Lett.* **3**13, 91 (1999).

[3] Y. Murakami, Y. Miyauchi, S. Chiashi, and S. Maruyama, *Chem. Phys. Lett.* **3**74, 53 (2003).

[4] K. S. Novoselov, A. K. Geim, S. V. Morozov, D. Jiang, Y. Zhang, S. V. Dubonos, I. V. Grigorieva, and A. A. Firsov, *Science* **3**06, 666 (2004).

[5] A. K. Geim and K. S. Novoselov, *Nat. Mater.* **6**, 183 (2007).

[6] R. Saito, G. Dresselhaus, and M. S. Dresselhaus, *Physical Properties of Carbon Nanotubes*, Imperial College Press, London, 1998.

[7] R. R. Nair, P. Blake, A. N. Grigorenko, K. S. Novoselov, T. J. Booth, T. Stauber, N. M. R. Peres, and A. K. Geim, *Science* **3**20, 1308 (2008).

[8] K. S. Kim, Y. Zhao, H. Jang, S. Y. Lee, J. M. Kim, K. S. Kim, J.-H. Ahn, P. Kim, J.-Y. Choi, and B. H. Hong, *Nature* **4**57, 706 (2009).

[9] D. M. Sun, M. Y. Timmermans, Y. Tian, A. G. Nasibulin, E. I. Kauppinen, S. Kishimoto, T. Mizutani, and Y. Ohno, *Nat. Nanotechnol.* **6**, 156 (2011).

[10] X. Gui, J. Wei, K. Wang, A. Cao, H. Zhu, Y. Jia, Q. Shu, and D. Wu, *Adv. Mater.* **2**2, 617 (2010).

[11] D. P. Hashim, N. T. Narayanan, J. M. Romo-Herrera, D. A. Cullen, M. G. Hahm, P. Lezzi, J. R. Suttle, D. Kelkhoff, E. Muñoz Sandoval, S. Ganguli, A. K. Roy, D. J. Smith, R. Vajtai, B. G. Sumpter, V. Meunier, H. Terrones, M. Terrones, and P. M. Ajayan, *Sci. Rep.* **2**, 1 (2012).

[12] Z. Zeng, X. Gui, Z. Lin, L. Zhang, Y. Jia, A. Cao, Y. Zhu, R. Xiang, T. Wu, and Z. Tang, *Adv. Mater.* **2**5, 1185 (2013).

[13] K. Jiang, Q. Li, and S. Fan, *Nature* **4**19, 801 (2002).

[14] M. Zhang, K. R. Atkinson, and R. H. Baughman, *Science* **3**06, 1358 (2004).

[15] M. D. Lima, N. Li, M. Jung de Andrade, S. Fang, J. Oh, G. M. Spinks, M. E. Kozlov, C. S. Haines, D. Suh, J. Foroughi, S. J. Kim, Y. Chen, T. Ware, M. K. Shin, L. D. Machado, A. F. Fonseca, J. D. W. Madden, W. E. Voit, D. S. Galvão, and R. H. Baughman, *Science* **3**38, 928 (2012).

[16] A. M. Rao, P. C. Eklund, S. Bandow, A. Thess, and R. E. Smalley, *Nature* **3**88, 257 (1997).

[17] C. Zhou, J. Kong, E. Yenilmez, and H. Dai, *Science* **2**90, 1552 (2000).

[18] M. Bockrath, J. Hone, A. Zettl, P. L. McEuen, A. G. Rinzler, and R. E. Smalley, *Phys. Rev. B* **6**1, R10606 (2000).

[19] S. Bandow, S. Asaka, Y. Saito, A. M. Rao, L. Grigorian, E. Richter, and P. C. Eklund, *Phys. Rev. Lett.* **8**0, 3779 (1998).

[20] W.-H. Chiang and R. M. Sankaran, *Nat. Mater.* **8**, 882 (2009).

[21] J. H. Davies, *The Physics of Low-Dimensional Semiconductors: An Introduction*, Cambridge University Press, Cambridge, UK., 1998.

[22] R. L. Liboff, *Introductory Quantum Mechanics*, 4th edn. Addison-Wesley, San Francisco, 2003.

[23] M. S. Dresselhaus, G. Dresselhaus, and P. Avouris, *Carbon Nanotubes: Synthesis, Structure, Properties, and Applications*, volume 80, Springer, Berlin, 2001.

[24] S. Reich, C. Thomsen, and J. Maultzsch, *Carbon Nanotubes: Basic Concepts and Physical Properties*, Wiley, 2004.

[25] G. S. Painter and D. E. Ellis, *Phys. Rev. B* **1**, 4747 (1970).

[26] L. Couture-Mathieu and J.-P. Mathieu, *Acta Cryst.* **5**, 571 (1952).

[27] M. S. Dresselhaus and P. C. Eklund, *Adv. in Phys* **4**9, 705 (2000).

[28] M. A. Pimenta, A. Marucci, S. A. Empedocles, M. G. Bawendi, E. B. Hanlon, A. M. Rao, P. C. Eklund, R. E. Smalley, G. Dresselhaus, and M. S. Dresselhaus, *Phys. Rev. B* **5**8, R16016 (1998).

[29] S. D. M. Brown, A. Jorio, P. Corio, M. S. Dresselhaus, G. Dresselhaus, R. Saito, and K. Kneipp, *Phys. Rev. B* **6**3, 155414 (2001).

[30] S. Piscanec, M. Lazzeri, J. Robertson, A. C. Ferrari, and F. Mauri, *Phys. Rev. B* **7**5, 035427 (2007).

[31] Y. Kawashima and G. Katagiri, *Phys. Rev. B* **5**9, 62 (1999).

[32] C. Thomsen and S. Reich, *Phys. Rev. Lett.* **8**5, 5214 (2000).

[33] S. D. M. Brown, A. Jorio, M. S. Dresselhaus, and G. Dresselhaus, *Phys. Rev. B* **6**4, 073403 (2001).

[34] M. Dresselhaus, G. Dresselhaus, A. Jorio, A. S. Filho, and R. Saito, *Carbon* **4**0, 2043 (2002).

[35] R. Saito, A. Gruneis, G. G. Samsonidze, G. Dresselhaus, M. S. Dresselhaus, A. Jorio, L. G. Cancado, M. A. Pimenta, and A. G. Souza, *Appl. Phys. A* **7**8, 1099 (2004).

[36] Y. Miyauchi, M. Oba, and S. Maruyama, *Phys. Rev. B* **7**4, 205440 (2006).

[37] R. Xiang, E. Einarsson, Y. Murakami, J. Shiomi, S. Chiashi, Z. Tang, and S. Maruyama, *ACS Nano* **6**, 7472 (2012).

[38] M. J. O'Connell, S. M. Bachilo, C. B. Huffman, V. C. Moore, M. S. Strano, E. H. Haroz, K. L. Rialon, P. J. Boul, W. H. Noon, C. Kittrell, J. P. Ma, R. H. Hauge, R. B. Weisman, and R. E. Smalley, *Science* **2**97, 593 (2002).

[39] O. A. Dyatlova, J. Gomis-Bresco, E. Malic, H. Telg, J. Maultzsch, G. Zhong, J. Geng, and U. Woggon, *Phys. Rev. B* **8**5, 245449 (2012).

[40] T. Okazaki, T. Saito, K. Matsuura, S. Ohshima, M. Yumura, and S. Iijima, *Nano Lett.* **5**, 2618 (2005).

[41] P. H. Tan, A. G. Rozhin, T. Hasan, P. Hu, V. Scardaci, W. I. Milne, and A. C. Ferrari, *Phys. Rev. Lett.* **9**9, 137402 (2007).

[42] J. G. Duque, C. E. Hamilton, G. Gupta, S. A. Crooker, J. J. Crochet, A. Mohite, H. Htoon, K. A. D. Obrey, A. M. Dattelbaum, and S. K. Doorn, *ACS Nano* **5**, 6686 (2011).

[43] A. Einstein, *Ann. d. Phys.* **1**7, 132 (1905).

[44] M. S. S. Doniach, *J. Phys. C: Solid State Phys.* **3**, 285 (1970).

[45] C. Kramberger, H. Shiozawa, H. Rauf, A. Grüneis, M. H. Rümmeli, T. Pichler, B. Büchner, D. Batchelor, E. Einarsson, and S. Maruyama, *Phys. Status Solidi B* **2**44, 3978 (2007).

[46] H. W. Kroto, J. R. Heath, S. C. O'Brien, R. F. Curl, and R. E. Smalley, *Nature* **3**18, 162 (1985).

[47] S. Iijima and T. Ichihashi, *Nature* **3**63, 603 (1993).

[48] D. S. Bethune, C. H. Klang, M. S. de Vries, G. Gorman, R. Savoy, J. Vazquez, and R. a. Beyers, *Nature* **3**63, 605 (1993).

[49] C. Journet, W. K. Maser, P. Bernier, A. Loiseau, M. L. de la Chapelle, S. Lefrant, P. Deniard, R. Lee, and J. E. Fischer, *Nature* **3**88, 756 (1997).

[50] A. Thess, R. Lee, P. Nikolaev, H. Dai, P. Petit, J. Robert, C. Xu, Y. H. Lee, S. G. Kim, A. G. Rinzler, D. T. Colbert, G. E. Scuseria, D. Tománek, J. E. Fischer, and R. E. Smalley, *Science* **2**73, 483 (1996).

[51] H. Dai, A. G. Rinzler, P. Nikolaev, A. Thess, D. T. Colbert, and R. E. Smalley, *Chem. Phys. Lett.* **2**60, 471 (1996).

[52] S. Maruyama, R. Kojima, Y. Miyauchi, S. Chiashi, and M. Kohno, *Chem. Phys. Lett.* **3**60, 229 (2002).

[53] Y. Shibuta and S. Maruyama, *Chem. Phys. Lett.* **3**82, 381 (2003).

[54] Y. Murakami, S. Chiashi, Y. Miyauchi, M. H. Hu, M. Ogura, T. Okubo, and S. Maruyama, *Chem. Phys. Lett.* **3**85, 298 (2004).

[55] S. Han, X. Liu, and C. Zhou, *J. Am. Chem. Soc.* **1**27, 5294 (2005).

[56] A. Ismach, L. Segev, E. Wachtel, and E. Joselevich, *Angew. Chem., Int. Ed.* **4**3, 6009 (2004).

[57] C. Kocabas, S.-H. Hur, A. Gaur, M. A. Meitl, M. Shim, and J. A. Rogers, *Small* **1**, 1110 (2005).

[58] Y. Murakami, Y. Miyauchi, S. Chiashi, and S. Maruyama, *Chem. Phys. Lett.* **3**77, 49 (2003).

[59] M. Hu, Y. Murakami, M. Ogura, S. Maruyama, and T. Okubo, *J. Catal.* **2**25, 230 (2004).

[60] K. Mukhopadhyay, A. Koshio, N. Tanaka, and H. Shinohara, *Jpn. J. Appl. Phys.* **3**7, L1257 (1998).

[61] K. Mukhopadhyay, A. Koshio, T. Sugai, N. Tanaka, H. Shinohara, Z. Konya, and J. B. Nagy, *Chem. Phys. Lett.* **3**03, 117 (1999).

[62] M. C. LeMieux, M. Roberts, S. Barman, Y. W. Jin, J. M. Kim, and Z. Bao, *Science* **3**21, 101 (2008).

[63] J.-H. Ahn, H.-S. Kim, K. J. Lee, S. Jeon, S. J. Kang, Y. Sun, R. G. Nuzzo, and J. A. Rogers, *Science* **3**14, 1754 (2006).

[64] G. Grüner, *J. Mater. Chem.* **1**6, 3533 (2006).

[65] M. D. Lay, J. P. Novak, and E. S. Snow, *Nano Lett.* **4**, 603 (2004).

[66] E. Artukovic, M. Kaempgen, D. S. Hecht, S. Roth, and G. Grüner, *Nano Lett.* **5**, 757 (2005).

[67] E. Snow, J. Novak, P. Campbell, and D. Park, *Appl. Phys. Lett.* **8**2, 2145 (2003).

[68] M. Zheng, A. Jagota, E. D. Semke, B. A. Diner, R. S. Mclean, S. R. Lustig, R. E. Richardson, and N. G. a. Tassi, *Nat. Mater.* **2**, 338 (2003).

[69] R. Krupke, F. Hennrich, H. v. Löhneysen, and M. M. Kappes, *Science* **3**01, 344 (2003).

[70] M. S. Arnold, A. A. Green, J. F. Hulvat, S. I. Stupp, and M. C. Hersam, *Nat. Nanotechnol.* **1**, 60 (2006).

[71] D. Golberg, Y. Bando, L. Bourgeois, K. Kurashima, and T. Sato, *Carbon* **3**8, 2017 (2000).

[72] U. Bangert, A. Bleloch, M. H. Gass, A. Seepujak, and J. van den Berg, *Phys. Rev. B* **8**1, 245423 (2010).

[73] F. Xu, M. Minniti, C. Giallombardo, A. Cupolillo, P. Barone, A. Oliva, and L. Papagno, *Surf. Sci.* **6**01, 2819 (2007).

[74] P. G. Collins, K. Bradley, M. Ishigami, and A. Zettl, *Science* **2**87, 1801 (2000).

[75] J.-Y. Yi and J. Bernholc, *Phys. Rev. B* **4**7, 1708 (1993).

[76] O. Stephan, P. M. Ajayan, C. Colliex, P. Redlich, J. M. Lambert, P. Bernier, and P. Lefin, *Science* **2**66, 1683 (1994).

[77] J. Ma, S. Guan, and C.-H. Lai, *Phys. Rev. B* **7**4, 205401 (2006).

[78] H. J. Choi, J. Ihm, S. G. Louie, and M. L. Cohen, *Phys. Rev. Lett.* **8**4, 2917 (2000).

[79] P. Ayala, R. Arenal, A. Loiseau, A. Rubio, and T. Pichler, *Rev. Mod. Phys.* **8**2, 1843 (2010).

[80] R. Arenal, X. Blase, and A. Loiseau, *Adv. in Phys* **5**9, 101 (2010).

[81] D. Wei, Y. Liu, Y. Wang, H. Zhang, L. Huang, and G. Yu, *Nano Lett.* **9**, 1752 (2009).

[82] L. S. Panchakarla, K. S. Subrahmanyam, S. K. Saha, A. Govindaraj, H. R. Krishnamurthy, U. V. Waghmare, and C. N. R. Rao, *Adv. Mater.* **2**1, 4726 (2009).

[83] D. Usachov, O. Vilkov, A. Grüneis, D. Haberer, A. Fedorov, V. K. Adamchuk, A. B. Preobrajenski, P. Dudin, A. Barinov, M. Oehzelt, C. Laubschat, and D. V. Vyalikh, *Nano Lett.* **1**1, 5401 (2011).

[84] T. Schiros, D. Nordlund, L. Pálová, D. Prezzi, L. Zhao, K. S. Kim, U. Wurstbauer, C. Gutiérrez, D. Delongchamp, C. Jaye, D. Fischer,

H. Ogasawara, L. G. M. Pettersson, D. R. Reichman, P. Kim, M. S. Hybertsen, and A. N. Pasupathy, *Nano Lett.* **1**2, 4025 (2012).

[85] P. H. Matter, E. Wang, and U. S. Ozkan, *J. Catal.* **2**43, 395 (2006).

[86] G. Vijayaraghavan and K. J. Stevenson, *Langmuir* **2**3, 5279 (2007).

[87] K. Gong, F. Du, Z. Xia, M. Durstock, and L. Dai, *Science* **3**23, 760 (2009).

[88] L. Qu, Y. Liu, J.-B. Baek, and L. Dai, *ACS Nano* **4**, 1321 (2010).

[89] D. Yu, E. Nagelli, F. Du, and L. Dai, *J. Phys. Chem. Lett.* **1**, 2165 (2010).

[90] P. Ayala, R. Arenal, M. Rümmeli, A. Rubio, and T. Pichler, *Carbon* **4**8, 575 (2010).

[91] A. H. Nevidomskyy, G. Csányi, and M. C. Payne, *Phys. Rev. Lett.* **9**1, 105502 (2003).

[92] B. Zheng, P. Hermet, and L. Henrard, *ACS Nano* **4**, 4165 (2010).

[93] V. Krstić, G. L. J. A. Rikken, P. Bernier, S. Roth, and M. Glerup, *Europhys. Lett.* **7**7, 37001 (2007).

[94] S. Latil, S. Roche, D. Mayou, and J.-C. Charlier, *Phys. Rev. Lett.* **9**2, 256805 (2004).

[95] R. Droppa, C. T. M. Ribeiro, A. R. Zanatta, M. C. dos Santos, and F. Alvarez, *Phys. Rev. B* **6**9, 045405 (2004).

[96] H. C. Choi, J. Park, and B. Kim, *J. Phys. Chem. B* **1**09, 4333 (2005).

[97] L. H. Chan, K. H. Hong, D. Q. Xiao, T. C. Lin, S. H. Lai, W. J. Hsieh, and H. C. Shih, *Phys. Rev. B* **7**0, 125408 (2004).

[98] S. Maldonado, S. Morin, and K. J. Stevenson, *Carbon* **4**4, 1429 (2006).

[99] A. A. Koós, M. Dowling, K. Jurkschat, A. Crossley, and N. Grobert, *Carbon* **47**, 30 (2009).

[100] P. Ayala, A. Grüeis, T. Gemming, D. Grimm, C. Kramberger, M. H. Rümmeli, F. L. Freire, H. Kuzmany, R. Pfeiffer, A. Barreiro, B. Büchner, and T. Pichler, *J. Phys. Chem. C* **1**11, 2879 (2007).

[101] P. Ayala, A. Grüneis, T. Gemming, B. Büchner, M. H. Rümmeli, D. Grimm, J. Schumann, R. Kaltofen, F. L. Freire Jr., H. D. F. Filho, and T. Pichler, *Chem. Mater.* **1**9, 6131 (2007).

[102] H. Lin, R. Arenal, S. Enouz-Vedrenne, O. Stephan, and A. Loiseau, *J. Phys. Chem. C* **1**13, 9509 (2009).

[103] H. Lin, J. Lagoute, C. Chacon, R. Arenal, O. Stéphan, V. Repain, Y. Girard, S. Enouz, L. Bresson, S. Rousset, and A. Loiseau, *Phys. Status Solidi B* **2**45, 1986 (2008).

[104] F. Villalpando-Paez, A. Zamudio, A. Elias, H. Son, E. Barros, S. Chou, Y. Kim, H. Muramatsu, T. Hayashi, J. Kong, H. Terrones, G. Dresselhaus, M. Endo, M. Terrones, and M. Dresselhaus, *Chem. Phys. Lett.* **4**24, 345 (2006).

[105] Z. Zhu, H. Jiang, T. Susi, A. G. Nasibulin, and E. I. Kauppinen, *J. Am. Chem. Soc.* **1**33, 1224 (2011).

[106] S.-G. KIM, S.-Y. KIM, and H.-W. LEE, *Trans. Nonferrous Met. Soc. China* **2**1, Supplement 1, s130 (2011).

[107] P. Ayala, A. Grüneis, C. Kramberger, M. H. Rümmeli, I. G. Solorzano, J. Freire, F. L., and T. Pichler, *J. Chem. Phys.* **1**27, 184709 (2007).

[108] E. Ibrahim, V. O. Khavrus, A. Leonhardt, S. Hampel, S. Oswald, M. H. Rümmeli, and B. Büchner, *Diamond Relat. Mater.* **1**9, 1199 (2010).

[109] A. R. Rocha, M. Rossi, A. J. R. da Silva, and A. Fazzio, *J. Phys. D: Appl. Phys.* **4**3, 374002 (2010).

[110] M. Terrones, H. Terrones, N. Grobert, W. K. Hsu, Y. Q. Zhu, J. P. Hare, H. W. Kroto, D. R. M. Walton, P. Kohler-Redlich, , M. Rühle, J. P. Zhang, and A. K. Cheetham, *Appl. Phys. Lett.* **7**5, 3932 (1999).

[111] K. Suenaga, M. Yudasaka, C. Colliex, and S. Iijima, *Chem. Phys. Lett.* **3**16, 365 (2000).

[112] M. Terrones, P. Ajayan, F. Banhart, X. Blase, D. Carroll, J. Charlier, R. Czerw, B. Foley, N. Grobert, R. Kamalakaran, P. Kohler-Redlich, M. Rühle, T. Seeger, and H. Terrones, *Appl. Phys. A* **7**4, 355 (2002).

[113] M. Terrones, R. Kamalakaran, T. Seeger, and M. Ruhle, *Chem. Commun.* , 2335 (2000).

[114] A. V. Okotrub, L. G. Bulusheva, A. G. Kudashov, V. V. Belavin, D. V. Vyalikh, and S. L. Molodtsov, *Appl. Phys. A* **9**4, 437 (2009).

[115] A. V. Okotrub, M. A. Kanygin, L. G. Bulusheva, and D. V. Vyalikh, *Fullerenes, Nanotubes, Carbon Nanostruct.* **1**8, 551 (2010).

[116] J. G. Zhou, J. A. Wang, H. Liu, M. N. Banis, X. L. Sun, and T. K. Sham, *J. Phys. Chem. Lett.* **1**, 1709 (2010).

[117] C. Kramberger, T. Thurakitseree, H. Koh, Y. Izumi, T. Kinoshita, T. Muro, E. Einarsson, and S. Maruyama, *Carbon* **5**5, 196 (2013).

[118] B. G. Sumpter, V. Meunier, J. M. Romo-Herrera, E. Cruz-Silva, D. A. Cullen, H. Terrones, D. J. Smith, and M. Terrones, *ACS Nano* **1**, 369 (2007).

[119] J. P. O'Byrne, Z. Li, S. L. T. Jones, P. G. Fleming, J. A. Larsson, M. A. Morris, and J. D. Holmes, *ChemPhysChem* **1**2, 2995 (2011).

[120] T. Susi, G. Lanzani, A. G. Nasibulin, P. Ayala, T. Jiang, T. Bligaard, K. Laasonen, and E. I. Kauppinen, *Phys. Chem. Chem. Phys.* **1**3, 11303 (2011).

[121] S. Taubert and K. Laasonen, *J. Phys. Chem. C* **1**16, 18538 (2012).

[122] S. M. Bachilo, L. Balzano, J. E. Herrera, F. Pompeo, D. E. Resasco, and R. B. Weisman, *J. Am. Chem. Soc.* **1**25, 11186 (2003).

[123] Y. Miyauchi, S. Chiashi, Y. Murakami, Y. Hayashida, and S. Maruyama, *Chem. Phys. Lett.* **3**87, 198 (2004).

[124] B. Wang, Y. Yang, L.-J. Li, and Y. Chen, *J. Mater. Sci.* **4**4, 3285 (2009).

[125] X. Li, X. Tu, S. Zaric, K. Welsher, W. S. Seo, W. Zhao, and H. Dai, *J. Am. Chem. Soc.* **1**29, 15770 (2007).

[126] H. Wang, B. Wang, X.-Y. Quek, L. Wei, J. Zhao, L.-J. Li, M. B. Chan-Park, Y. Yang, and Y. Chen, *J. Am. Chem. Soc.* **1**32, 16747 (2010).

[127] S. Suzuki, N. Asai, H. Kataura, and Y. Achiba, *Eur. Phys. J. D* **4**3, 143 (2007).

[128] A. M. Cassell, J. A. Raymakers, J. Kong, and H. Dai, *J. Phys. Chem. B* **1**03, 6484 (1999).

[129] R. Xiang, E. Einarsson, J. Okawa, Y. Miyauchi, and S. Maruyama, *J. Phys. Chem. C* **1**13, 7511 (2009).

[130] J. H. Hafner, M. J. Bronikowski, B. R. Azamian, P. Nikolaev, A. G. Rinzler, D. T. Colbert, K. A. Smith, and R. E. Smalley, *Chem. Phys. Lett.* **2**96, 195 (1998).

[131] H. M. Cheng, F. Li, G. Su, H. Y. Pan, L. L. He, X. Sun, and M. S. Dresselhaus, *Appl. Phys. Lett.* **7**2, 3282 (1998).

[132] C. L. Pint, Z. Sun, S. Moghazy, Y.-Q. Xu, J. M. Tour, and R. H. Hauge, *ACS Nano* **5**, 6925 (2011).

[133] L. G. Bulusheva, A. Okotrub, A. G. Kudashov, Y. V. Shubin, E. Shlyakhova, N. F. Yudanov, E. M. Pazhetnov, A. I. Boronin, and D. V. Vyalikh, *Carbon* **4**6, 864 (2008).

[134] Y. Xia, R. Mokaya, D. M. Grant, and G. S. Walker, *Carbon* **4**9, 844 (2011).

[135] T. Cui, R. Lv, Z.-H. Huang, H. Zhu, J. Zhang, Z. Li, Y. Jia, F. Kang, K. Wang, and D. Wu, *Carbon* **4**9, 5022 (2011).

[136] R. Xiang, Z. Zhang, K. Ogura, J. Okawa, E. Einarsson, Y. Miyauchi, J. Shiomi, and S. Maruyama, *Jpn. J. Appl. Phys.* **4**7, 1971 (2008).

[137] T. Thurakitseree, C. Kramberger, P. Zhao, S. Chiashi, E. Einarsson, and S. Maruyama, *Phys. Status Solidi B* **2**49, 2404 (2012).

[138] Y. Murakami and S. Maruyama, *Chem. Phys. Lett.* **4**22, 575 (2006).

[139] Z. Wu, Z. Chen, X. Du, J. M. Logan, J. Sippel, M. Nikolou, K. Kamaras, J. R. Reynolds, D. B. Tanner, A. F. Hebard, and A. G. Rinzler, *Science* **3**05, 1273 (2004).

[140] T. Thurakitseree, C. Kramberger, P. Zhao, S. Aikawa, S. Harish, S. Chiashi, E. Einarsson, and S. Maruyama, *Carbon* **5**0, 2635 (2012).

[141] P. T. Araujo, S. K. Doorn, S. Kilina, S. Tretiak, E. Einarsson, S. Maruyama, H. Chacham, M. A. Pimenta, and A. Jorio, *Phys. Rev. Lett.* **9**8, 067401 (2007).

[142] R. Pfeiffer, H. Kuzmany, F. Simon, S. N. Bokova, and E. Obraztsova, *Phys. Rev. B* **7**1, 155409 (2005).

[143] P. Zhao, E. Einarsson, R. Xiang, Y. Murakami, and S. Maruyama, *J. Phys. Chem. C* **1**14, 4831 (2010).

[144] M. S. Dresselhaus, G. Dresselhaus, R. Saito, and A. Jorio, *Physics Reports* **4**09, 47 (2005).

[145] O. Dubay, G. Kresse, and H. Kuzmany, *Phys. Rev. Lett.* **8**8, 235506 (2002).

[146] M. J. Matthews, M. A. Pimenta, G. Dresselhaus, M. S. Dresselhaus, and M. Endo, *Phys. Rev. B* **5**9, R6585 (1999).

[147] J. F. Cardenas and A. Gromov, *Chem. Phys. Lett.* **4**42, 409 (2007).

[148] I. O. Maciel, N. Anderson, M. A. Pimenta, A. Hartschuh, H. Qian, M. Terrones, H. Terrones, J. Campos-Delgado, A. M. Rao, L. Novotny, and A. Jorio, *Nat. Mater.* **7**, 878 (2008).

[149] I. O. Maciel, M. A. Pimenta, M. Terrones, H. Terrones, J. Campos-Delgado, and A. Jorio, *Phys. Status Solidi B* **2**45, 2197 (2008).

[150] C. Kramberger, T. Thurakitseree, and S. Maruyama, *Phys. Status Solidi B* **2**49, 2369 (2012).

[151] T. Susi, J. Kotakoski, R. Arenal, S. Kurasch, H. Jiang, V. Skakalova, O. Stephan, A. V. Krasheninnikov, E. I. Kauppinen, U. Kaiser, and J. C. Meyer, *ACS Nano* **6**, 8837 (2012).

[152] S. M. Bachilo, M. S. Strano, C. Kittrell, R. H. Hauge, R. E. Smalley, and R. B. Weisman, *Science* **2**98, 2361 (2002).

[153] A. Jorio, R. Saito, J. H. Hafner, C. M. Lieber, M. Hunter, T. McClure, G. Dresselhaus, and M. S. Dresselhaus, *Phys. Rev. Lett.* **8**6, 1118 (2001).

[154] C. Fantini, A. Jorio, M. Souza, M. S. Strano, M. S. Dresselhaus, and M. A. Pimenta, *Phys. Rev. Lett.* **9**3, 147406 (2004).

[155] S. H. Lim, H. I. Elim, X. Y. Gao, A. T. S. Wee, W. Ji, J. Y. Lee, and J. Lin, *Phys. Rev. B* **7**3, 045402 (2006).

[156] J. Scofield, *J. Electron Spectrosc. Relat. Phenom.* **8**, 129 (1976).

[157] R. H. Baughman, A. A. Zakhidov, and W. A. de Heer, *Science* **2**97, 787 (2002).

[158] C. Liu, Y. Y. Fan, M. Liu, H. T. Cong, H. M. Cheng, and M. S. Dresselhaus, *Science* **2**86, 1127 (1999).

[159] A. C. Dillon, K. M. Jones, T. A. Bekkedahl, C. H. Kiang, D. S. Bethune, and M. J. Heben, *Nature* **3**86, 377 (1997).

[160] S. C. Tsang, Y. K. Chen, P. J. F. Harris, and M. L. H. Green, *Nature* **3**72, 159 (1994).

[161] B. W. Smith, M. Monthioux, and D. E. Luzzi, *Nature* **3**96, 323 (1998).

[162] S. Bandow, M. Takizawa, K. Hirahara, M. Yudasaka, and S. Iijima, *Chem. Phys. Lett.* **3**37, 48 (2001).

[163] R. Kitaura, N. Imazu, K. Kobayashi, and H. Shinohara, *Nano Lett.* **8**, 693 (2008).

[164] H. Oshima, Y. Suzuki, T. Shimazu, and S. Maruyama, *Jpn. J. Appl. Phys.* **4**7, 1982 (2008).

[165] W.-T. Chen, Y. Yamada, G.-N. Liu, A. Kubota, T. Ichikawa, Y. Kojima, G.-C. Guo, and S. Fukuzumi, *Dalton Trans.* **4**0, 12826 (2011).

[166] C. R. Brundle, *J. Vac. Sci. Technol.* **1**3, 301 (1976).

[167] M. Grunze, J. Fühler, M. Neumann, C. Brundle, D. Auerbach, and J. Behm, *Surf. Sci.* **1**39, 109 (1984).

[168] O. Björneholm, A. Nilsson, A. Sandell, B. Hernnäs, and N. Mårtensson, *Phys. Rev. Lett.* **6**8, 1892 (1992).

[169] H. C. Choi, S. Y. Bae, J. Park, K. Seo, C. Kim, B. Kim, H. J. Song, and H.-J. Shin, *Appl. Phys. Lett.* **8**5, 5742 (2004).

[170] R. Barajas-Barraza, J. Ramirez-Ruíz, and R. Guirado-López, *J. Comput. Theor. Nanosci.* **5**, 2255 (2008).

[171] S. Gayen, S. N. Behera, and S. M. Bose, *Phys. Rev. B* **7**6, 165433 (2007).

[172] H. C. Choi, S. Y. Bae, W.-S. Jang, J. Park, H. J. Song, H.-J. Shin, H. Jung, and J.-P. Ahn, *J. Phys. Chem. B* **1**09, 1683 (2005).

[173] C. Kramberger, H. Rauf, H. Shiozawa, M. Knupfer, B. Buchner, T. Pichler, D. Batchelor, and H. Kataura, *Phys. Rev. B* **7**5, 235437 (2007).

[174] C. T. Chen, Y. Ma, and F. Sette, *Phys. Rev. A* **4**0, 6737 (1989).

[175] L. Liu and S. Fan, *J. Am. Chem. Soc.* **1**23, 11502 (2001).

[176] J. H. Yang, D. H. Lee, M. H. Yum, Y. S. Shin, E. J. Kim, C. Y. Park, M. H. Kwon, C. W. Yang, J. B. Yoo, H. J. Song, H. J. Shin, Y. W. Jin, and J. M. Kim, *Carbon* **4**4, 2219 (2006).

[177] R. Xiang, B. Hou, E. Einarsson, P. Zhao, S. Harish, K. Morimoto, Y. Miyauchi, S. Chiashi, Z. Tang, and S. Maruyama, *ACS Nano* **7**, 3095 (2013).

[178] S. D. Costa, C. Fantini, A. Righi, A. Bachmatiuk, M. H. Rümmeli, R. Saito, and M. A. Pimenta, *Carbon* **4**9, 4719 (2011).

[179] C. Kramberger, M. Löffler, M. Rümmeli, A. Grüneis, R. Schönfelder, O. Jost, T. Gemming, T. Pichler, and B. Büchner, *Phys. Status Solidi B* **2**43, 3050 (2006).

[180] F. Simon, C. Kramberger, R. Pfeiffer, H. Kuzmany, V. Zólyomi, J. Kürti, P. M. Singer, and H. Alloul, *Phys. Rev. Lett.* **9**5, 017401 (2005).

[181] A. Lifshitz and C. Tamburu, *Int. J. Chem. Kinet.* **3**0, 341 (1998).

[182] Y. Murakami, E. Einarsson, T. Edamura, and S. Maruyama, *Phys. Rev. Lett.* **9**4, 087402 (2005).

[183] Z. Zhang, E. Einarsson, Y. Murakami, Y. Miyauchi, and S. Maruyama, *Phys. Rev. B* **8**1, 165442 (2010).

[184] C. Kramberger, T. Thurakitseree, S. Chiashi, E. Einarsson, and S. Maruyama, *Appl. Phys. A* **1**09, 509 (2012).

[185] F. Esaka, H. Shimada, M. Imamura, N. Matsubayashi, T. Kikuchi, and K. Furuya, *J. Electron Spectrosc. Relat. Phenom.* **8**8, 817 (1998).

[186] M. Petravic, Q. Gao, D. Llewellyn, P. N. K. Deenapanray, D. Macdonald, and C. Crotti, *Chem. Phys. Lett.* **4**25, 262 (2006).

[187] G. Abbas, P. Papakonstantinou, G. R. S. Iyer, I. W. Kirkman, and L. C. Chen, *Phys. Rev. B* **7**5, 195429 (2007).

[188] S. Plimpton, *J. Comput. Phys.* **1**17, 1 (1995).

[189] M. Levitt, M. Hirshberg, R. Sharon, and V. Daggett, *Comput. Phys. Commun.* **9**1, 215 (1995).

[190] H. Kataura, Y. Kumazawa, Y. Maniwa, Y. Ohtsuka, R. Sen, S. Suzuki, and Y. Achiba, *Carbon* **3**8, 1691 (2000).

[191] L. An, J. M. Owens, L. E. McNeil, and J. Liu, *J. Am. Chem. Soc.* **1**24, 13688 (2002).

[192] A. G. Nasibulin, P. V. Pikhitsa, H. Jiang, and E. I. Kauppinen, *Carbon* **4**3, 2251 (2005).

[193] B. Wang, C. H. P. Poa, L. Wei, L.-J. Li, Y. Yang, and Y. Chen, *J. Am. Chem. Soc.* **1**29, 9014 (2007).

[194] H. Ago, S. Imamura, T. Okazaki, T. Saito, M. Yumura, and M. Tsuji, *J. Phys. Chem. B* **1**09, 10035 (2005).

[195] D. Ciuparu, Y. Chen, S. Lim, G. L. Haller, and L. Pfefferle, *J. Phys. Chem. B* **1**08, 503 (2004).

[196] Y. Chen, D. Ciuparu, S. Lim, Y. Yang, G. L. Haller, and L. Pfefferle, *J. Catal.* **2**26, 351 (2004).

[197] M. Picher, E. Anglaret, R. Arenal, and V. Jourdain, *ACS Nano* **5**, 2118 (2011).

[198] Y. Yao, Q. Li, J. Zhang, R. Liu, L. Jiao, Y. T. Zhu, and Z. Liu, *Nat. Mater.* **6**, 283 (2007).

[199] G. Ning and H. Shinohara, *Chem. Asian J.* **4**, 955 (2009).

[200] D. C. Wei, Y. Q. Liu, L. C. Cao, L. Fu, X. L. Li, Y. Wang, G. Yu, and D. B. Zhu, *Nano Lett.* **6**, 186 (2006).

[201] M. Ouyang, J. L. Huang, and C. M. Lieber, *Acc. Chem. Res.* **3**5, 1018 (2002).

[202] Z. Jin, X. Li, W. Zhou, Z. Han, Y. Zhang, and Y. Li, *Chem. Phys. Lett.* **4**32, 177 (2006).

[203] J. Li, C. Papadopoulos, and J. Xu, *Nature* **4**02, 253 (1999).

[204] G. W. Meng, Y. J. Jung, A. Y. Cao, R. Vajtai, and P. M. Ajayan, *Proc. Natl. Acad. Sci. U. S. A.* **1**02, 7074 (2005).

[205] D. Wei, L. Cao, L. Fu, X. Li, Y. Wang, G. Yu, and Y. Liu, *Adv. Mater.* **1**9, 386 (2007).

[206] J. J. Jackson, A. A. Puretzky, K. L. More, C. M. Rouleau, G. Eres, and D. B. Geohegan, *ACS Nano* **4**, 7573 (2010).

[207] D. B. Geohegan, A. A. Puretzky, J. J. Jackson, C. M. Rouleau, G. Eres, and K. L. More, *ACS Nano* **5**, 8311 (2011).

[208] A. A. Puretzky, D. B. Geohegan, J. J. Jackson, S. Pannala, G. Eres, C. M. Rouleau, K. L. More, N. Thonnard, and J. D. Readle, *Small* **8**, 1534 (2012).

[209] Y. Tian, M. Timmermans, S. Kivistö, A. Nasibulin, Z. Zhu, H. Jiang, O. G. Okhotnikov, and E. I. Kauppinen, *Nano Res.* **4**, 807 (2011).

[210] G. Zhang, P. Qi, X. Wang, Y. Lu, D. Mann, X. Li, and H. Dai, *J. Am. Chem. Soc.* **1**28, 6026 (2006).

[211] Q. Liu, W. Ren, Z.-G. Chen, D.-W. Wang, B. Liu, B. Yu, F. Li, H. Cong, and H.-M. Cheng, *ACS Nano* **2**, 1722 (2008).

[212] W. J. Yu, S. Y. Lee, S. H. Chae, D. Perello, G. H. Han, M. Yun, and Y. H. Lee, *Nano Lett.* **1**1, 1344 (2011).

[213] M. He, H. Jiang, E. I. Kauppinen, and J. Lehtonen, *Nanoscale* **4**, 7394 (2012).

[214] E. Einarsson, Y. Murakami, M. Kadowaki, and S. Maruyama, *Carbon* **4**6, 923 (2008).

[215] S. Melchor and J. A. Dobado, *J. Chem. Inf. Comput. Sci.* **4**4, 1639 (2004).

[216] T. Thurakitseree, C. Kramberger, A. Kumamoto, S. Chiashi, E. Einarsson, and S. Maruyama, *ACS Nano* **7**, 2205 (2013).

[217] S. Maruyama, E. Einarsson, Y. Murakami, and T. Edamura, *Chem. Phys. Lett.* **4**03, 320 (2005).

[218] H. Kataura, Y. Kumazawa, Y. Maniwa, I. Umezu, S. Suzuki, Y. Ohtsuka, and Y. Achiba, *Synth. Met.* **1**03, 2555 (1999).

[219] A. A. Koós, F. Dillon, E. A. Obraztsova, A. Crossley, and N. Grobert, *Carbon* **4**8, 3033 (2010).

[220] H. Liu, Y. Zhang, R. Li, X. Sun, S. Désilets, H. Abou-Rachid, M. Jaidann, and L.-S. Lussier, *Carbon* **4**8, 1498 (2010).

[221] L. Zhu, Y. Xiu, D. W. Hess, and C.-P. Wong, *Nano Lett.* **5**, 2641 (2005).

[222] T. Iwasaki, G. Zhong, T. Aikawa, T. Yoshida, and H. Kawarada, *J. Phys. Chem. B* **1**09, 19556 (2005).

[223] T. Iwasaki, J. Robertson, and H. Kawarada, *Nano Lett.* **8**, 886 (2008).

[224] R. Xiang, E. Einarsson, J. Okawa, T. Thurakitseree, Y. Murakami, J. Shiomi, Y. Ohno, and S. Maruyama, *J. Nanosci. Nanotechnol.* **1**0, 3901 (2010).

[225] M.-F. C. Fiawoo, A.-M. Bonnot, H. Amara, C. Bichara, J. Thibault-Pénisson, and A. Loiseau, *Phys. Rev. Lett.* **1**08, 195503 (2012).

[226] W. Zhu, A. Rosen, and K. Bolton, *J. Chem. Phys.* **1**28, 124708 (2008).

[227] K. Hasegawa and S. Noda, *Carbon* **4**9, 4497 (2011).

[228] S. Hofmann, R. Sharma, C. Ducati, G. Du, C. Mattevi, C. Cepek, M. Cantoro, S. Pisana, A. Parvez, F. Cervantes-Sodi, A. C. Ferrari, R. Dunin-Borkowski, S. Lizzit, L. Petaccia, A. Goldoni, and J. Robertson, *Nano Lett.* **7**, 602 (2007).

[229] S. Chiashi, Y. Murakami, Y. Miyauchi, and S. Maruyama, *Jpn. J. Appl. Phys.* **4**7, 2010 (2008).

Acknowledgement

We never know what will happen in future or the near future. There may be something that cause people come together, despite no one knows each other before or just by name. This always happen with scientists. With the same destination, work can be accomplished with collaborations. This PhD work was conducted between October, 2010 and September, 2013 in **Maruyama-Shiomi lab.**, Department of Mechanical, The University of Tokyo.

First of all, I am very grateful to **the Office of the Higher Education Commission** that always supports me during PhD course. It could never be possible without the guidance of my supervisor **Prof. Shigeo Maruyama**. It does not matter how many questions and how hard it is, he always provided me rough idea in order to let me have some spaces to think about problems on my own. "*it may be this*" or "*it may be that*", these seem to be his style and identical sentences. Of course, some people who do not understand his point, may think that this is hard time for them to the bright way. On the other hand, I have learned how to think and create some idea myself by just sparking one idea from others. He did give me an impressive advice on my PhD research with all written in this thesis.

I am also grateful to committee members of my PhD presentation: **Prof. Yuichi Ikuhara**, **Prof. Tatsuya Okubo**, **Assoc. Prof. Junichiro Shiomi**, and **Dr. Shohei Chiashi**. They did give me very useful and sophisticated comments on my presentation, so that I could be able to improve weak points on my thesis, including systematical ways of thinking.

Nobody knows which ways they should go for the further PhD research. I am also one of those people who got stuck in dark obscure idea for almost one year at the beginning of my PhD study. It turned out that I have met one researcher, who has opened up a bright way and motivated me to keep moving further on research. Of course, it is sometime quite difficult to express by just one word for some feeling. Really great thanks to **Dr. Christian Kramberger** from the University of Vienna with many things coming to my life and research. He is very experience scientist in many field, especially solid state physics, and is essentially my second advisor. Before this I just understood that only synthesis of carbon nanotubes for PhD research should be the only one research topic that I could do, but it is indeed not. I can do research on many things using many different tools. He has taught me how to do spectroscopy measurement in the correct way and how to correctly analyse spectrum. XPS and NEXAFS spectroscopy methods are also tools which I have learned from him. He really gave me a big opportunity to learn how to do NEXAFS measurement at SPring8 synchrotron, one of the most powerful new generation synchrotron in Japan. He is really willing to share ideas with important discussion. I sometime felt bad because I often asked him many different questions, but he was always willing to answer me with clear explanation. He told me one thing that make me more eager to learn something new, *you ask because you want to know and learn. If you do not ask, it means you do not want to learn.* He did devote great effort into teaching me scientific writing and researching. Most of my PhD research in this thesis and ideas are contributed from him. This effort help me a lot on writing scientific articles, and the early version of this thesis.

I am grateful to **Dr. Erik Einarsson** who always adviced and helped me during my whole years of PhD study and since my Master course. He is very experience scientist, and always open for easy and difficult questions. Some ideas of my research were sparked from a few words that he suggested. Many good discussion brought us to good quality of work. An key discussion

on role of nitrogen on SWNT synthesis was mainly suggested by him. Due to his experience in x-ray absorption measurement, we also went to SPring8 together with Dr. Kramberger. Besides researching, he also devotes great effort me into teaching and improving my scientific writing, and starting point of this thesis. Out of work, we always walked around the campus and discussed a lot on what to do the near future as scientist.

I am grateful to the group of **Prof. Yuichi Ikuhara** and especially to **Dr. Akihito Kumamoto** from the University of Tokyo, for devoting great effort into TEM observation on small-diameter SWNTs, particularly on SWNTs with different diameters of multi-layered SWNT array. They did contribute to the discussions with their expertise on TEM observation of nano materials. Also great thanks to **Dr. K. Ibe**, a TEM technician, who supported me for early TEM observation on small-diameter SWNTs and double-layered SWNT arrays. He also did taught and assisted me how to do TEM from the beginning.

I never expected that I would at some point work with people who is doing simulation, because our researches are quite different. I am grateful to **Heeyuen Koh** for smart simulation of trapped-N_2 molecules inside different diameters of SWNTs. She did spent part of her research time on this simulation before we eventually have a nice scientific articles published.

The accomplishment of SPring8 activities would not be happened without great helps of very experienced beamline scientists, **Dr. Takayuki Muro**, **Dr. Toyohiko Kinoshita**, and **Dr. Yudai Izumi**. They did provide sophisticated measurement system for NEXAFS measurement, and good discussion on trapped N_2 molecules inside SWNTs.

Other than my expertise, **Dr. Shinya Aikawa**, **Sungjin Kim**, and **Taiki Inoue** did devote their research time for supporting nano-device fabrications and discussions on transfer characteristic of N-doepd SWNTs. Even though they were very busy with their won research, they are willing to help me with their expertise on nanotube devices.

I am grateful to **Global Center of Excellent (GCOE) Program** which always supported me to attend international conferences. Other than doing research in Maruyama Lab., this program did open opportunity for me to do international internship in the US and Germany. I am grateful to **Prof. Pulickel M. Ajayan** from Rice University and **Prof. Tobias Hertel** from University of Würzberg, who accepted me to join their research activities during my internship. Beside creating new research idea, these experiences have taught a lot for being a researcher, and how differences between Japanese, American, and German researchers are, including the ways they think and conduct their researches.

S. Harish, **Cui Kehang**, and **Dr. Pei Zhao** have different research experience on their own expertises. Although our research fields are irrelevant by the main goals, we did discuss our own researches and exchanged some ideas whenever we had chance, and it was indeed good opportunity for beer with good discussions.

My research would not be completed without a good Raman measurement system with three different lasers. I am also grateful thanks to **Dr. Shohei Chiashi** for sophisticated Raman system. Of course, it will be hard to survive and do a good job if we just only go to the lab, work, and go back home with no communications with others. My life in the lab was colourful with many funny things and some crazy talks with other lab members. I am grateful to friendly atmosphere at work: **Dr. James Cannon**, **Dr. Takuma Shiga**, **Takuma Hori**, **Jiayu Wang**, **Takanori Umino**, **Takafumi Oyake**, and **Takaaki Chiba**.

And lastly, I would like to thank and express my hearty gratitude to my fiancée, **Tuenta Naphun**, and **my family** for their understanding and encouragement for PhD study.

Curriculum Vitae

Education

Current :	Ph.D. candidate in Mechanical Engineering **The University of Tokyo**, Japan *CVD synthesis and characterization of nitrogen-doped single-walled carbon nanotubes* Advisor: Prof. Shigeo Maruyama
September 2010 :	M.Sc. in Mechanical Engineering **The University of Tokyo**, Japan *Diameter controlled CVD growth of single-walled carbon nanotubes* Advisor: Prof. Shigeo Maruyama
March 2006 :	B.Sc. in Physics **Chiang Mai University**, Thailand *Synthesis and physical property studies of cobalt beta-diketonate complexes* *Second class honors*, Major: Physics-Material Science Advisor: Assist. Prof. Kamonpan Pengpat Co-advisors: Assist. Prof. Phimphaka Harding and Assoc. Prof. David J. Harding, Walailak university, Thailand.

Scholarships and Certificates

2011 : Poster Award
12th International Conference on the Science and Application of Nanotubes (NT11)

2010–2013 : Graduate Research Assistant
21st Century Global Center of Excellence for Mechanical Systems Innovation (GMSI)

2008–2013 : Strategic Frontier Research Scholarship
The Office of the Higher Education Commission (CHE-PhD-SFR)

2006 : Academic Excellence Award (Bronze)
B.Sc., Chiang Mai University

2002–2006 : Promotion Project for Teacher Production in Sciences and Mathematics Scholarship

Languages

Thai : Mothertongue

English : Fluent

Japanese : Basic Knowledge

Research Interests

1. Synthesis of single-walled carbon nanotubes
2. Energy-related application of carbon nanotubes
3. Optical and physical properties of single-walled carbon nanotubes
4. Spectroscopy of single-walled carbon nanotubes

Internships

February 2012 :	Short term internship at **Tobias Hertel research group** Unviersity of Würzburg, Würzburg, Germany Helped to approach growth of small-diameter SWNTs in range of (6,5) nanotube and solve problem CVD apparatus
July–August 2011 :	Reversed NanoJapan program at **Ajayan research group** Rice Unviersity, Houston, Texas, USA Worked in the growth lab, helped to synthesize CNT forest for applications and other studies, and solved problem of gaining CNT yield by dip-coating approach

List of Figures

1.1 Ewald's sphere in 3D k-space 7
1.2 Density of states in different dimensions 8
1.3 Geometry construction of SWNT 11
1.4 Different chiralities of nanotubes 13
1.5 Unit cells in real and reciprocal spaces 15
1.6 Cutting lines in the Brillouin zone 16
1.7 First Brillouin zone of graphene 16
1.8 Energy dispersion of graphene 17
1.9 Density of states of metallic and semiconducting SWNTs 19
1.10 Chirality map of SWNT 20
1.11 Raman scattering process 22
1.12 Resonance Raman spectra of SWNTs 25
1.13 Schematic of light absorption 26
1.14 Van Hove Singularity of SWNTs 28
1.15 Kataura plot and absorbance of individual nanotubes 29
1.16 PLE map of individual nanotubes 31
1.17 X-ray photoemission process 33
1.18 XPS spectrum of clean SWNTs 34
1.19 Near-edge x-ray absorption process 35
1.20 Polarization-dependent NEXAFS spectra of VA-SWNTs 36
1.21 Principal of SEM and image of VA-SWNTs 37
1.22 Principal of TEM and HRTEM image of nanotubes 38
1.23 Different morphology of nanotubes 40

1.24 Dip-coating process 42

2.1 Nitrogen configurations with carbon environment 47
2.2 XAS of C1s and N1s edges of N-doped graphene 49

3.1 SEM images of VA-SWNTs synthesized from pure AcN 53
3.2 TEM images and diameter distribution of SWNTs 54
3.3 Optical absorption spectra of as-grown VA-SWNTs 55
3.4 Raman spectra of small- and large-diameter SWNTs 56
3.5 PLE maps of dispersed small-diameter SWNTs 58
3.6 SEM images of SWNTs with different AcN mixtures 59
3.7 Optical absorption spectra of different SWNT diameters 60
3.8 Raman spectra of SWNTs with different AcN mixtures 61
3.9 Splitting of G^+ and G^- 62
3.10 Raman characteristic of AcN-grown SWNTs 63
3.11 Raman spectra of SWNTs on zeolite support 64
3.12 Optical absorption spectra of individual N-doped SWNTs 65
3.13 PLE maps of individual N-doped SWNTs 66
3.14 A plot between diameter with normalized peak areas 67
3.15 Peak fitting of absorption spectra of as-grown SWNTs 69
3.16 XPS spectra of SWNTs synthesized from AcN mixtures 72
3.17 Correlation between SWNT diameter and AcN mixtures 73
3.18 XPS spectra of dispersed SWNTs grown on zeolite 74

4.1 XPS of 5%AcN-grown VA-SWNTs 77
4.2 XPS spectra after N_2 removed 78
4.3 G-band fitting 79
4.4 Polarization-dependent NEXAFS spectra of C1s edge 80
4.5 Polarization-dependent NEXAFS of N1s edge 81
4.6 NEXAFS of isotope $^{15}N_2$ 83
4.7 G-band shift by isotope $CH_3{}^{13}CN$ 85
4.8 Degree of alignment analysis of N_2 87
4.9 MD simulation of aligned 1D N_2 89

4.10 Isotropic distribution 90

5.1 SEM imagesn of double-layered arrays 94
5.2 Growth curves of double-layered arrays 96
5.3 Raman spectra of diameter-changed SWNTs 97
5.4 Reversible SWNT diameter 99
5.5 Diameter distributions of SWNTs 100
5.6 Interface examination 101
5.7 Growth curve of five-layers arrays 102
5.8 TEM images of nanotube interface 103
5.9 STEM and HR-TEM of diameter-changed junctions 103
5.10 Interface region of SWNTs 104
5.11 XPS spectra of N_2 on EtOH-grown layer 105
5.12 Growth mechanism of N-doped SWNTs 107

A.1 Polarization-dependent Raman spectra of VA-SWNTs 114
A.2 Nematic order parameter of VA-SWNTs 115

Lists of publications

Peer-Reviewed Publications

19. C. Kramberger, **T. Thurakitseree**, E. Einarsson, A. Takashima, T. Kinoshita, T. Muro, and S. Maruyama, "From $CH_3{-}C^{15}N$ to $^{15}N_2$ inside single-walled carbon nanotubes", (2013), *to be submitted*.

18. C. Kramberger, **T. Thurakitseree**, H. Shiozawa, A. Stang, Y. Izumi, T. Kinoshita, T. Muro, T. Pichler, S. Maruyama, "Length scales in nematic order of vertically aligned single walled carbon nanotubes", (2013), *submitted*.

17. C. Kramberger, **T. Thurakitseree**, S. Maruyama, and M. Knupfer, "On the effect of diameter in the loss-function of single-walled carbon nanotubes", Nanotechnology (2013), *in press*.

16. K. Cui, T. Chiba, S. Omiya, **T. Thurakitseree**, P. Zhao, E. Einarsson, S. Chiashi, and S. Maruyama, "Self-Assembled Microhoneycomb Network of Single-Walled Carbon Nanotubes for Solar Cells", *J. Phys. Chem. Lett.*, 4, 2571 (2013).
doi:10.1021/jz401242a

15. **T. Thurakitseree**, C. Kramberger, A. Kumamoto, S. Chiashi, E. Einarsson, and S. Maruyama, "Reversible diameter modulation of single-walled carbon nanotubes by acetonitrile-containing feedstock", *ACS Nano*, 7, 2205 (2013).
doi:10.1021/nn3051852

14. C. Kramberger, **T. Thurakitseree**, H. Koh, Y. Izumi, T. Kinoshita, T. Muro, E. Einarsson, and S. Maruyama, "One-dimensional N_2 gas inside single-walled carbon nanotube containers", *Carbon*, 55, 196 (2012)
doi:10.1016/j.carbon.2012.12.026

13. C. Kramberger, **T. Thurakitseree**, S. Chiashi, E. Einarsson, and S. Maruyama, "On the polarization-dependent Raman spectra of aligned carbon nanotubes", *Appl. Phys. A*, 109, 509 (2012).
doi:10.1007/s00339-012-7305-8

12. C. Kramberger, **T. Thurakitseree**, and S. Maruyama, "Sub-nanometer thin single walled carbon nanotubes: Nitrogen does the trick", *Phys. Stat. Sol. (b)*, 249, 2369 (2012).
doi:10.1002/pssb.201200112

11. **T. Thurakitseree**, C. Kramberger, P. Zhao, S. Chiashi, E. Einarsson, and S. Maruyama, "Reduction of single-walled carbon nanotube diameter to sub-nm via feedstock", *Phys. Sat. Sol. (b)*, 249, 2404 (2012).
doi:10.1002/pssb.201200126

10. S. Lee, M. G. Hahm, R. Vajtai, D. P. Hashim, **T. Thurakitseree**, A. C. Chipara, P. M. Ajayan, and J. H. Hafner, "Utilizing 3d SERS active volumes in aligned carbon nanotube scaffold substrates", *Adv. Mater.*, 24, 5261 (2012).
doi.org/10.1002/adma.201200645

9. **T. Thurakitseree**, C. Kramberger, P. Zhao, S. Aikawa, S. Harish, S. Chiashi, E. Einarsson, and S. Maruyama, "Diameter-controlled and nitrogen-doped vertically aligned single-walled carbon nanotubes", *Carbon*, 50, 2635 (2012).
doi:10.1016/j.carbon.2012.02.023

8. **T. Thurakitseree**, E. Einarsson, R. Xiang, P. Zhao, S. Aikawa, S. Chiashi, J. Shiomi, and S. Maruyama, "Diameter controlled CVD synthesis of single-walled carbon nanotubes", *J. Nanosci. Nanotech.*, 12, 370 (2012).
doi:10.1166/jnn.2011.5398

7. S. Aikawa, E. Einarsson, **T. Thurakitseree**, S. Chiashi, E. Nishikawa, and S. Maruyama, "Deformable transparent all-carbon-nanotube transistors",*Appl. Phys. Lett.*, 100, 063502 (2012).
doi:10.1063/1.3683517

6. C. Kramberger, E. Einarsson, S. Huotari, **T. Thurakitseree**, S. Maruyama, M. Knupfer, and T. Pichler, "Plasma dynamics in graphite and SWNT probed by inelastic electron and X-ray scattering", *Phys. Stat. Sol. (c)*, 7, 2789 (2010).
doi:10.1002/pssc.201000290

5. S. Takada, T. Nakai, **T. Thurakitseree**, J. Shiomi, S. Maruyama, H. Takagi, M. Shuzo, J.-J. Delaunay, and I. Yamada, "Micro gas preconcentrator made of a film of single-walled carbon nanotubes", *IEEJ Trans. SM*, 130, 207 (2010).
doi:10.1541/ieejsmas.130.207

4. C. Kramberger, E. Einarsson, S. Huotari, **T. Thurakitseree**, S. Maruyama, M. Knupfer, and T. Pichler, "Interband and plasma excitations in single-walled carbon nanotubes and graphite in inelastic x-ray and electron scattering", *Phys. Rev. B*, 81, 205410 (2010).
doi:10.1103/PhysRevB.81.205410

3. R. Xiang, E. Einarsson, J. Okawa, **T. Thurakitseree**, Y. Murakami, J. Shiomi, Y. Ohno, and S. Maruyama, "Parametric study of ACCVD for controlled synthesis of vertically aligned single-walled carbon nanotubes", *J. Nanosci. Nanotech.*, 10, 3901 (2010).
doi:10.1166/jnn.2010.2011

2. P. Harding, D. J. Harding, R. Daengngern, **T. Thurakitseree**, B. M. Schutte, M. J. Shaw, and Y. Tantirungrotechai, "Redox coupled-spin crossover in cobalt β-diketonate complexes: Structural, electrochemical and computational studies", *Polyhedron*, 42, 291 (2012). doi.org/10.1016/j.poly.2012.05.037

1. D. J. Harding, P. Harding, **T. Thurakitseree**, and H. Adams, "Unexpected oxidation of a disphosphine by bis(1,3-diphenylpropane-1,3-dionato)cobalt(II), [Co(dbm)$_2$]", *Acta. Cryst.*, C63, m163 (2007). doi.org/10.1107/S010827010700933X

International Conference Contributions

5. **T. Thurakitseree** *et al.*
   13th International Conference on the Science and Application of Nanotubes (NT12), Brisbane, Australia (2012)
   http://www.nt12.org/

4. **T. Thurakitseree** *et al.*
   IWEPNM 2012, Kirchberg, Austria (2012)
   http://www.iwepnm.org/2012/2012.php

3. **T. Thurakitseree** *et al.*
   12th International Conference on the Science and Application of Nanotubes (NT11), Cambridge, UK (2011)
   http://www.msm.cam.ac.uk/nt11/

2. **T. Thurakitseree** *et al.*
   APS March Meeting, Dallas, USA (2011)
   http://www.aps.org/meetings/march/info/index.cfm

1. **T. Thurakitseree** *et al.*
   Asia Nano conference, Tokyo, Japan (2010)
   http://asianano2010.org/index.html

Domestic Conference Contributions

4. **T. Thurakitseree** *et al.*
   The 41st Fullerenes-Nanotubes-Graphene General Symposium
   Tokyo, Japan (2011).

3. **T. Thurakitseree** *et al.*
   Micro Nano Mechanical Engineering Symposium 2nd
   Shimane, Japan (2010).

2. **T. Thurakitseree** *et al.*
   Heat Transfer Symposium 47th
   Hokkaido, Japan (2010).

1. **T. Thurakitseree** *et al.*
   Fullerene-Nanotubes Symposium 38th
   Nagoya, Japan (2010).